Composite Spin Hall Conductivity from Non-collinear Antiferromagnetic Order in $PtMn_3$

by

Steve Novakov

A dissertation submitted in partial fulfillment
of the requirements for the degree of
Doctor of Philosophy
(Physics)
in the University of Michigan
2021

Doctoral Committee:

Assistant Professor John Heron, Chair
Assistant Professor Robert Hovden
Associate Professor Kai Sun
Assistant Professor Liuyan Zhao

Steve Novakov

steveeee@umich.edu

ORCID ID: 0000-0003-2467-4061

ACKNOWLEDGEMENTS

My principal thanks must go to the other University of Michigan Ferroelectronics Laboratory pioneers: Peter Meisenheimer, Nguyen Vu, and Sieun Chae. We started with empty, barren laboratories, but full imaginations. With hard work and diligence we persevered.

There are many collaborators who contributed to this and other works and to my overall development, most significantly A.J. Grutter and R.F. Need from NIST NCNR, S.H. Sung and R. Hovden from Michigan, G.A. Pan and J.A. Mundy from Harvard, and the J.A. Robinson group at Penn State.

Of course I have to thank my family and friends. If my parents failed to feed me during childhood, I would have died of malnourishment and therefore been unable to produce this work. If a formal lifetime support hierarchy were to be defined, it would be entirely reasonable to place them at the top. My friends surely enhanced my mental health in a positive way and were generally not an additional source of stress in my life.

I acknowledge financial support from the Semiconductor Research Corporation NEWLIMITS Center and NIST through award number 70NANB17H041, and the University of Michigan.

TABLE OF CONTENTS

LIST OF FIGURES

FIGURE

LIST OF APPENDICES

APPENDIX

ABSTRACT

Thin film antiferromagnets have emerged as strong candidates for state-of-the-art spintronic applications, promising efficient spin current generation that is critical for the development of low power non-volatile electronics [1–3]. Intrinsic spin current generation in thin films has been primarily studied in systems with interfacial symmetry breaking [4, 5] (such as the Rashba-Edelstein effect), surface spin current from a topological insulator state [6–8], or a bulk spin Hall effect in heavy metal systems such as W, Ta, or Pt [9–12]. In general, the high symmetry of these nonmagnetic systems limits the spin Hall conductivity tensor components to that of a left-handed polarization texture around the applied current direction, with out-of-plane spin currents having only $\hat{y}$ polarization [13]. In contrast, the reduced symmetry of non-collinear antiferromagnets allows for additional linear-response-driven spin conductivities, including longitudinal and out-of-plane spin currents with $\hat{x}, \hat{z}$ polarization, though the measured effects so far have been small and non-tunable [14,15]. Understanding the intrinsic origin of these out-of-plane spin currents with atypical polarization could enable new developments in low power non-volatile spin-based electronics.

In this work, multi-component out-of-plane spin Hall conductivities σ^x_{xz}, σ^y_{xz},σ^z_{xz} are discovered in $L1_2$ ordered antiferromagnetic $PtMn_3$ thin films that are uniquely generated in the non-collinear state. The maximum spin torque efficiencies ($\xi = J_S/J_e \sim 0.3$) are found to be significantly larger than in Pt ($\xi \sim 0.1$), a canonical spin Hall effect material. Additionally, the spin Hall conductivities in the non-collinear state exhibit an orientation-dependent anisotropy, which can be used to select for a dominant component. The work presented here demonstrates symmetry control through the magnetic lattice as a pathway to tailored functionality in magnetoelectronic systems.

CHAPTER 1

Introduction

1.1 Electronic Spin Currents and The Spin Hall Effect

Many exotic physical phenomena in modern condensed matter physics arise in spintronic systems, where an underlying mechanism results in a coherent and significant spin polarization of charge carriers. In traditional electronic materials, charge carriers such as electrons or holes flow with no coherent spin order, and there is some resulting current under an applied electric field $\boldsymbol{J} = \bar{\sigma}\boldsymbol{E}$, as per a generalized Ohm's law. In contrast, spintronic systems have an additional degree of freedom in the spin polarization of carriers, whether from some uniform average polarization or a more complicated spin-momentum distribution. There are two categories of phenomena which lead to coherent spin polarization of current: extrinsic, involving relativistic carrier-impurity scattering, and intrinsic, where the band structure of the material itself causes either net spin polarization through static band filling (e.g. in ferromagnets) or dynamic polarization of the carriers under applied field through a linear response effect. The polarization efficiency of extrinsic spin conductivity is generally quite small ($<< 1\%$, though it can be brought higher with impurity doping, within the same order of magnitude as heavy metals [16]), and the effect is well explained [17–19]. It is the intrinsic phenomena that are the most interesting from a physics perspective, and which offer high spin polarization efficiencies for potential device applications. The main focus of this work is intrinsic spin current generation in the different antiferromagnetic phases of $L1_2$ ordered $PtMn_3$ and how symmetry control through the magnetic lattice can enable nonstandard spin Hall conductivity at a high efficiency and with directional anisotropy. To start, an overview is given of intrinsic spin current generation in electronic materials, with a focus on the role of global symmetry in determining the structure of linear response phenomena in spintronic systems.

The simplest intrinsic mechanism for a coherent spin polarization of charge carriers is that in a conducting ferromagnet, where each band is split by the macroscopic internal field, leading to a spin-dependent band filling in particular bands (Figure 1.1a). This is the driving physics

behind spin-transfer torque magnetic tunnel junction devices, where an electron current is spin polarized by standard conduction through a pinned strong ferromagnet, and then transfers this spin angular momentum via a scattering process in a subsequent, weaker strength "free" ferromagnet (Figure 1.1b).

Another simple mechanism for intrinsic spin current generation is the Rashba-Edelstein Effect (REE) [19, 20], where a population of charge carriers is exposed to a strong electric field, say in the $\hat{z}$ direction. The total system Hamiltonian is then:

$$H = \frac{\hbar^2 k^2}{2m} + \lambda \boldsymbol{k} \times \boldsymbol{\sigma} \cdot \mathcal{E}_z \hat{z} \tag{1.1.1}$$

where λ is the Rashba coupling constant, $\boldsymbol{k}$ is the crystal momentum, $\boldsymbol{\sigma}$ is the Pauli spin matrix vector, and $\mathcal{E}_z$ is the electric field amplitude. It's clear from this expression that the energy minimum in momentum space $\boldsymbol{k}$ is such that $\boldsymbol{s} \perp \hat{k} \times \hat{z}$. Statically, there is no net spin in the carrier population, but when an exernal field is applied in the xy-plane, the momentum distribution shifts so that there is a net carrier spin polarization (Figure 1.1c). This effect is readily realized in thin film systems, for example in metal/oxide bilayers or metals on oxide substrates, where the out-of-plane differences in carrier density cause a charge gradient and a resulting $\mathcal{E}_z = -\nabla V$. The degree of spin polarization from the REE can be readily measured in heterostructures of oxides and metallic ferromagnets [21], and is particularly strong in metal/ferroelectric interfaces [22], where it can be reversed by switching the ferroelectric, as outlined in (Figure 1.1d). Because of the explicit orthogonality between the out-of-plane charge gradient, forward carrier momentum, and spin polarization, REE materials can not generate out-of-plane spin polarizations, and the the spin current does flow out-of-plane. This greatly reduces their efficiency in thin film applications, which revolve around out-of-plane magnetic structures with low total area such as MTJs with in-plane or perpendicular anisotropy magnets. The REE in thin film systems is a simple example of how a broken symmetry, here the out-of-plane mirror symmetry of the charge density, leads to breaking of degeneracy between spin bands, and a dynamic response with a spin-momentum distribution.

The most relevant mechanism for intrinsic spin current generation in this work is the intrinsic spin Hall effect (SHE), where under an applied electric field the ensemble of charge carriers picks up an anomalous transverse momentum that is coupled to the spin degree of freedom. In contrast to ferromagnetic polarization and the REE, which are equilibrium descriptions of perturbed state energies, understanding the intrinsic SHE requires a dynamical theory of the response to carriers to the applied field [12, 23, 24]. In the canonical SHE in heavy metal systems, there is no net spin polarization in the ensemble of charge carriers in the static system. However, an applied electric field leads to an outward diffusion of spin in a left handed circular texture orthogonal to

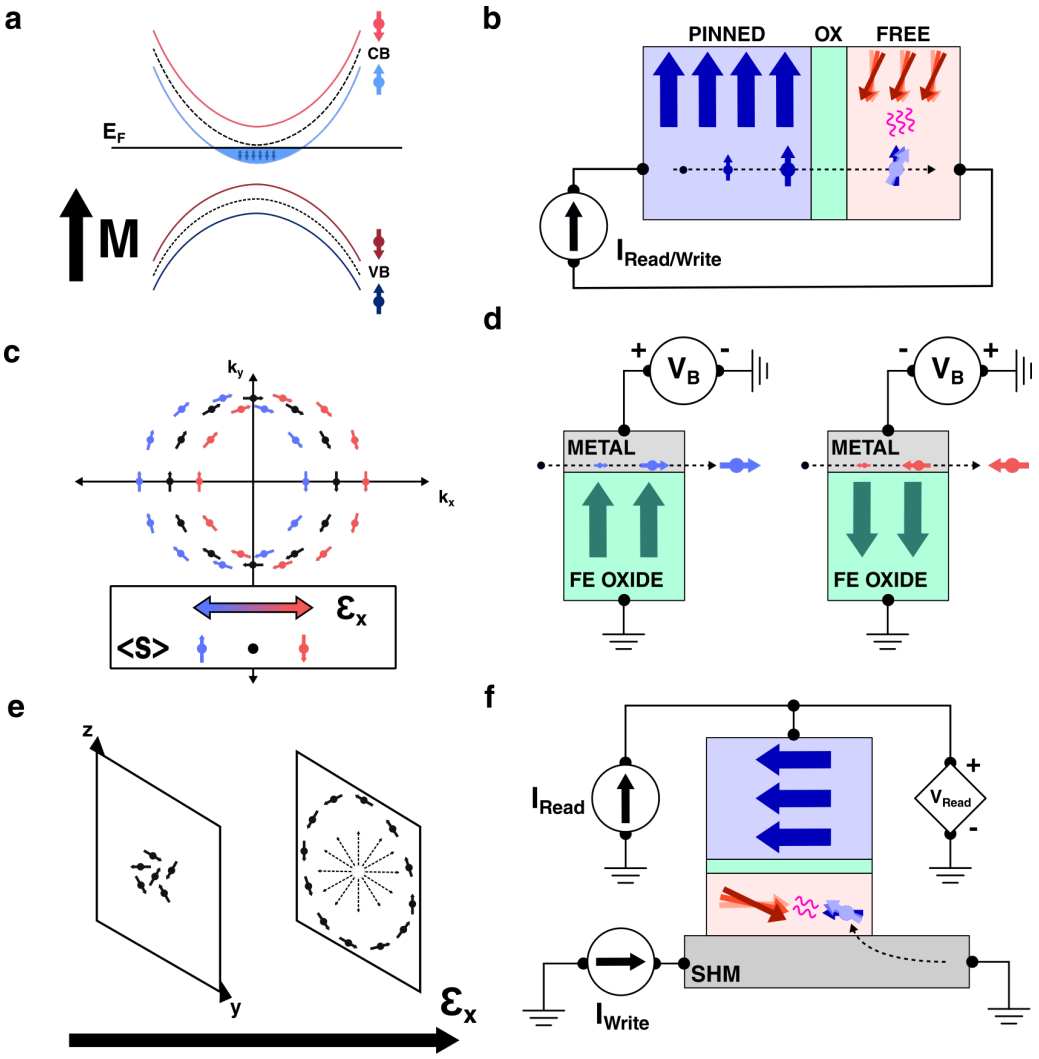

Figure 1.1: **Mechanisms for intrinsic spin currents in electronic systems**. **a**, Conduction band spin polarization from exchange splitting in a ferromagnetic metal, and **b**, example application in magnetic tunnel junction (MTJ) device where induced polarization from a strongly magnetized (pinned) layer is used to transfer angular momentum to a weakly magnetized (free) layer and flip its orientation. **c**, Rashba polarization of charge carriers in a quasi-2D system with an internal out-of-plane electric field such as a metal/ferroelectric (FE) oxide interface and the resulting net spin $\langle S \rangle$ vs. applied in-plane electric field $\mathcal{E}_x$. **d**, Sufficiently biasing the ferroelectric to induce switching will reverse the effect and flip the net spin polarization. **e**, Transverse spin-momentum distribution of carriers under applied electric field in an intrinsic spin Hall effect (SHE) material. **f**, The outward spin current diffusion is particularly useful in thin film systems where, for example, SHE materials can be used for more efficient writing of MTJs in vertical heterostructures.

the electric field direction, as shown in Figure 1.1e. In general, the polarization efficiency in heavy metal SHE systems is more efficient than in traditional MTJs and they can be used as a separate

write layer, as in (Figure 1.1f), allowing for more variation in magnetic heterostructure design. Further, heterostructures of thin film magnets and heavy metal SHE systems offer approximately 10 times lower average switching energy compared to traditional MTJs, as per a recent survey of modern works [25]. Unlike the other mechanisms for spin polarization, this behavior is not readily intuitive, and requires a multi-state adiabatic time evolution formalism to understand completely.

For some system Hamiltonian $H(\boldsymbol{R})$ with some slowly varying parameters $\boldsymbol{R}(t)$, at every point in time there are some instantaneous set of eigenstates $H(\boldsymbol{R})\left|n(\boldsymbol{R})\right\rangle = \epsilon_n(\boldsymbol{R})\left|n(\boldsymbol{R})\right\rangle$. Then, if the parameters are being changed slowly enough that there is no significant inter-state tunneling (adiabatic evolution), the evolved state $\left|\psi_n(t)\right\rangle$ is:

$$\left|\psi_n(t)\right\rangle = e^{i\gamma_n(t)} \exp\left[-\frac{i}{\hbar}\int_0^t dt' \epsilon_n(\boldsymbol{R}(t'))\right]\left|n(\boldsymbol{R}(t))\right\rangle \tag{1.1.2}$$

where the right two terms are the standard dynamic phase factor from first-order time-dependent perturbation theory and the instantaneous eigenstate, and the leading term is the geometric phase factor. This geometric phase $\gamma_n(t)$ is conveniently expressed as a path integral in the variable parameter space:

$$\gamma_n(t) = i\int_{\boldsymbol{R}(0)}^{\boldsymbol{R}(t)} d\boldsymbol{R}' \cdot \left\langle n(\boldsymbol{R}')\right| \nabla_{\boldsymbol{R}'} \left|n(\boldsymbol{R}')\right\rangle = \int_{\mathcal{C}} d\boldsymbol{R}' \cdot \mathcal{A}_n(\boldsymbol{R}') \tag{1.1.3}$$

where $\mathcal{A}_n$ is referred to as the Berry connection. In general, $\gamma_n(t)$ is of no physical consequence in physical systems, as it is not gauge-invariant with choice of path in parameter space and can be made to vanish. However, when the adiabatic evolution of the system is cyclical, that is, there is a closed path in parameter space, $\gamma_n(t)$ is independent of the exact path taken through parameter space and is referred to as the Berry phase:

$$\gamma_n = \oint_C d\boldsymbol{R} \cdot \mathcal{A}_n(\boldsymbol{R}) \tag{1.1.4}$$

The physical significance of this term, and of cyclic adiabatic evolution in quantum many body systems, was identified by its namesake in 1984 [26]. Unlike the geometric phase, the Berry phase is a gauge-invariant physical quantity and has a measurable effect on quantum state evolution (confusingly, the two terms are often used interchangably).

While the geometric phase is only of physical consequence in cyclical time evolution, there is a corresponding quantity, the Berry curvature:

$$\Omega^n_{\mu\nu} = \frac{\partial}{\partial R^\mu}\mathcal{A}^n_\nu(\boldsymbol{R}) - \frac{\partial}{\partial R_\nu}\mathcal{A}^n_\mu(\boldsymbol{R}) \tag{1.1.5}$$

which is essentially the "phase-flux" for the system in parameter space, and has physical consequence due to its gauge invariance. Particularly in the case of Bloch electrons, it can be shown that under an applied electric field $\boldsymbol{\mathcal{E}}$, there emerges an anomalous transverse velocity that is an explicit function of the Berry curvature:

$$\boldsymbol{v}_n(\boldsymbol{k}) = \frac{\partial E_n(\boldsymbol{k})}{\hbar \partial \boldsymbol{k}} - \frac{e}{\hbar}\boldsymbol{\mathcal{E}} \times \boldsymbol{\Omega}_n(\boldsymbol{k}) \tag{1.1.6}$$

where $\boldsymbol{\Omega}_n(\boldsymbol{k})$ is the vector Berry curvature vector for the $|n, \boldsymbol{k}\rangle$ Bloch state, related to the tensor form by $\Omega^n_{\mu\nu} = \epsilon_{\mu\nu\eta}(\boldsymbol{\Omega}_n)_\eta$. In ferromagnets, $\boldsymbol{\Omega} \parallel \boldsymbol{M}$, the internal exchange field and the source of band splitting [27], and so the wave packet formalism sufficiently explains their intrinsic anomalous Hall conductivity, first observed in 1880 by its namesake [28, 29] and linked more explicitly to the ferromagnetic anisotropy in 1953 [30]. In the non-magnetic case, where Bloch states of opposite spin are degenerate in the equilibrium system, it can be shown that $\boldsymbol{\mathcal{E}} \times \boldsymbol{\Omega}_n \propto \boldsymbol{\mathcal{E}} \times \boldsymbol{s}$ (see discussion around Equation (9.15) in Ref. [27]), which is exactly the canonical intrinsic SHE described in Figure 1.1c. In heavy metal SHE systems, the large Berry curvature is attributed to spin-orbit coupling. The Berry curvature is maximal near the high symmetry k-points where spin-orbit coupling breaks band degeneracy. For the system to have a large SHE, it is ideal if this gap is small, and that the Fermi level lies inside it [9, 12, 27]. In general, describing real physical systems with simple models like Equation 1.1.6 is difficult, as it is not possible to derive a macroscopic vector field that applies consistently to all Bloch states. To calculate accurate spin Hall conductivities σ^s_{ij}, it is most practical to use computational methods to calculate the energy spectrum for the Bloch states, and to integrate the spin Berry curvature $\Omega^s_{ij,n}(\boldsymbol{k})$ over all n bands and momenta in the Brillouin zone (BZ):

$$\sigma^s_{ij} = \frac{e}{\hbar}\sum_n \int_{k\in \mathrm{BZ}} \frac{d^3k}{(2\pi)^3} f_n(k)\Omega^s_{ij,n}(k) \tag{1.1.7}$$

where $f_n(k)$ is the state occupancy, which is nonzero up to the Fermi momentum. It is important to note that, somewhat nonintuitively, this does not scale with the strength of the spin-orbit coupling directly. High spin Hall conductivity in heavy metal systems such as Ta, Pt, and W is thought to be a consequence of the combined 4*f*-5*d* valence shell having more avoided crossings than in lighter 3/4*d* systems, and the potential to contribute more high Berry curvature zones in the momentum space to the total macroscopic integral [24, 31]. The structure and symmetry of the Bloch bands in momentum space play a key role in the ultimate macroscopic spin or anomalous Hall effect. Additional contributions to the system Hamiltonian, such as exchange interactions between the conduction electrons and a magnetic lattice, can change the Bloch state energetics (band degeneracy, Fermi level, state filling) as well as the total system symmetry (number of

high symmetry k-points, additional degeneracy lifting), leading to different amplitudes for the macroscopic spin Hall conductivity, or its outright suppression.

1.2 Linear Response in Electronic Materials

For multi-state adiabatic quantum evolution, the wave packet formalism as in Equation 1.1.6 is difficult to formulate outside of approximate or toy models, and with low band counts (as low as 2, but up to 4 doubly degenerate bands [23, 32]). In general, precise evaluation of Equation 1.1.7 is done with computational methods, first computing the Bloch band structure of the equilibrium Hamiltonian, and then the change to the relevant observable (usually $\underline{\sigma}$, $\underline{\sigma}^s$) through a linear response formalism [24, 33]. In general, linear response theory defines how an observable of a multi-state system will change with an applied perturbation that is slow enough to guarantee adiabatic evolution of states. Consider a system with some equilibrium Hamiltonian, H_0, with an additional time dependent perturbation. The total Hamiltonian is:

$$H = H_0 + \hat{V}(t) \tag{1.2.1}$$

where the additional $\hat{V}(t) = \hat{B}f(t)$, with $\hat{B}$ being some quantum mechanical operator, and $f(t)$ being a time dependent scalar. In the most relevant case to solid state systems, the perturbation is an applied electric field $\mathcal{E}(t)$ and $\hat{V}(t) = e\mathcal{E}(t)\hat{r}$. Assuming the perturbation is applied slowly enough that the system evolves adiabatically, the linear response of some observable $\hat{A}$ to the perturbation is:

$$\delta A_i = \chi^A_{ij} V_j \tag{1.2.2}$$

where χ^A_{ij} is the linear response tensor for $\hat{A}$.

The adiabaticity condition for the linear response theory being valid is that the slew rate of the perturbation is significantly lower than the natural state oscillation frequency (see discussion in Ref. [34] around eq. (5.6.11)):

$$\frac{\langle m(t)|\, \dot{H}\, |n(t)\rangle}{E_{nm}} = \langle m(t)|\, \hat{r}\, |n(t)\rangle\, \frac{e}{E_{nm}} \frac{\partial \mathcal{E}(t)}{\partial t} << \langle m(t)|\, \frac{\partial}{\partial t}\, |m(t)\rangle \tag{1.2.3}$$

That is, there is a smooth adiabatic evolution of the quantum states under applied electric field with no inter-state transitions. Violation of this condition is commonly referred to as "breakthrough", when the Bloch electrons transition to upper bands and undergo ballistic transport. The condition

for electric field breakthrough is (see Ref. [35] (J.8)):

$$\frac{E_{nm}^2}{E_F} >> e\mathcal{E}a \tag{1.2.4}$$

where E_F is the Fermi energy, $\mathcal{E}$ is the ultimate electric field in the steady state, and a is the unit cell constant corresponding to one Brillouin zone. In the vast majority of plausible physical scenarios, this condition is well satisfied. The theoretical Fermi energy for a wide range of metals ranges from 1.5-12 eV (see Table 2.1 in [35]), and Bravais lattice constants are typically 5 Å or less. Regarding the band gap, a lower bound can be estimated for all possible materials by requiring it to be more significant than the thermalization energy $E_T = k_B T \sim 25$ meV at room temperature. Selecting $E_{nm} > 10\ k_B T$ as a limit for significance, then, at room temperature:

$$\mathcal{E} << \frac{(0.25\text{ eV})^2}{12\text{ eV} \cdot e \cdot 0.5 \cdot 10^{-7}\text{cm}} \approx 105\ \frac{\text{kV}}{\text{cm}} \tag{1.2.5}$$

Electric fields in excess of 100 kV/cm are not typical in well conducting systems, and are more commonly seen in capacitive applications with strong insulators. In samples used in this work, typical devices have channel lengths of no less than 10 μm, and the channel voltage is at most 5 V. This yields $\mathcal{E} \leq 5$ kV/cm, which satisfies the adiabaticity criteria well. An electric field of 5kV/cm in a typical metallic film with $\rho \sim 100\mu\Omega \cdot$ cm (well satisfied in this work) results in a current density of $J = 5 \cdot 10^7$ A/cm^2, which is most likely destructive even in very thin films. In this work $J \leq 5 \cdot 10^6$ A/cm^2 for all transport measurements to reduce possible device damage or excessive localized heating, and so the adiabaticity condition is satisfied by a further order of magnitude.

In the context of solid state electronic systems, it is convenient to re-write χ_{ij}^A in the Bloch band basis:

$$\chi_{ij}^A = \lim_{\epsilon \to 0} \sum_k \sum_{m,n} \frac{f(E_{m,k}) - f(E_{n,k})}{E_{m,k} - E_{n,k} - i\epsilon} \langle n,k|\, \hat{A}_i\, |m,k\rangle \langle m,k|\, \hat{B}_j\, |m,k\rangle \tag{1.2.6}$$

where m, n are band indices and k is the crystal momentum. If the full spectrum of Bloch states and energies has been calculated already, it is easy to put together χ_{ij}^A for a choice of observable $\hat{A}$. Usually the observable of most interest is the conductivity. In this case $\hat{A} = -e\hat{v}\mathcal{V}$, the current density (normalized to total volume $\mathcal{V}$), $\hat{F} = eE\hat{r}$, and the linear response tensor corresponds exactly to the Berry curvature [36]:

$$\chi_{ij,nk}^A = \Omega_{ij,nk} = \sum_{m \neq n} \frac{1}{E_{m,k} - E_{n,k}} \langle n,k|\, \hat{v}_i\, |m,k\rangle \langle m,k|\, \hat{v_j}\, |n,k\rangle \tag{1.2.7}$$

If instead the *spin* conductivity is considered, then $\hat{A} = (1/2)\{\hat{s}, \hat{v}\}/\mathcal{V}$ is the spin current density, and

$$\chi^{A,s}_{ij,nk} = \Omega^{s}_{ij,nk} = \sum_{m \neq n} \frac{1}{E_{m,k} - E_{n,k}} \langle n,k| \hat{J}^{s}_{i} |m,k\rangle \langle m,k| \hat{v}_{j} |n,k\rangle \tag{1.2.8}$$

which is often dubbed the *spin* Berry curvature, and used to compute the spin Hall conductivity tensor as in Equation 1.1.7. The computed linear response tensor and ultimate conductivity can correspond well with physical measurements, assuming the perturbation is indeed adiabatic (e.g. the anomalous Hall conductivity of bcc Fe showing excellent correspondence between experiment and theory at about 700-1000 $\Omega^{-1}\text{cm}^{-1}$ [37]). Computing σ^{s}_{ij} explicitly is the definitive way to gauge the intrinsic spin current generating capability of a particular material. However, this can be intensive in both time and computing resources for a broad survey of materials. It turns out that the global symmetry of a particular Hamiltonian can enforce a certain structure for σ^{s}_{ij}. For wide classes of materials, simply knowing their global symmetry group is enough to determine whether particular σ^{s}_{ij} components are allowed to exist without having to compute them explicitly.

1.3 Symmetry-enforced Structure of Linear Response Tensors in Magnetic Systems

Separate from their ultimate numerical values, the structure of the linear response tensor components is enforced by the global symmetry of the Hamiltonian under consideration. Specifically, it must transform in a consistent way with the full set of symmetry operations of the system (see discussion around eq. (39)-(44) in Ref. [13]). For magnetic systems, the operations are extended to time reversal, or combinations of translation/rotation with time reversal, and there is a corresponding magnetic Laue group. In general, high symmetry systems with a large number of symmetry operators force most of the elements of σ^{s}_{ij} to be zero, for example in non-magnetic heavy metals such as Pt (Laue group $m\bar{3}m1'$, see Figure 1.2). In the particular case of cubic non-magnets, a system with very high symmetry, the tensor structure is such that there is only the canonical SHE which is completely isotropic (as in Figure 1.1). If spin-orbit coupling is a dominant contribution to the Hamiltonian, then even weakly magnetic systems or systems with high magnetic symmetry will be limited to this canonical SHE, unless an equally energetic interaction is present that reduces global symmetry.

In systems with strong on-site magnetization, a separate contribution to the linear response tensor arises from itinerant electron interaction with the magnetic lattice (s-d model). This ex-

change can be significant, and is predicted to generate large intrinsic spin conductivities without any contribution from spin-orbit coupling [14, 38]. There are four general classes of microscopic magnetic lattices: collinear ferromagnets (e.g. Fe), collinear antiferromagnets/ferrimagnets (e.g. Cr_2O_3), non-collinear antiferromagnets (e.g. XMn_3 compounds, and the pyrochlore iridates), and some combination of those, such as a non-coplanar ferromagnet with some chiral texture [38]. It is the greatly reduced global symmetry of fully non-collinear antiferromagnetic systems, compared to non-magnets or ferromagnets, which allows for unconventional non-zero components of the linear response tensors for charge and spin currents. For instance, breaking two-fold rotational symmetry or inversion permits out-of-plane spin currents with additional $\hat{x}, \hat{z}$ polarization, and even intrinsic longitudinal spin currents [13, 14].

Within the class of non-collinear antiferromagnets, the XMn_3 compounds (X = Ga, Ge, Sn, Ir, Pt, and Rh) have garnered considerable interest as a platform for studying intrinsic spin and anomalous Hall effects. The combination of a strong s-d exchange with Mn ($\mu \sim 3\mu_B$ [39]) and the reduced global symmetry of their low temperature non-collinear antiferromagnetic states opens the possibility for large intrinsic spin Hall conductivities with unconventional components [33]. Already the hexagonal $SnMn_3$ has been shown to generate large intrinsic anomalous and spin Hall effects [40, 41], with the anomalous Hall effect's dependence on spin order being used for prototype logic devices [42]. The $L1_2$ ordered cubic XMn_3 compounds (X = Rh, Ir, Pt) offer additional antiferromagnetic magnetic phases, with a possible intermediate-temperature collinear state (Laue group $4'/mmm'$), and low-temperature non-collinear state (Laue group $\bar{3}m'1$) with an alternating all-in-all-out Kagome lattice in the (111) planes (see Figure 1.2). Both of these phases have been explicitly identified in bulk $PtMn_3$ via neutron diffraction, and their existance and transition temperatures were shown to vary with Mn composition [39]. The spin Hall conductivity tensor of the low symmetry non-collinear ground state is significantly less restricted than in canonical SHE systems, and there is no symmetry enforcement of an isotropic response in arbitrary crystal orientations [13, 33]. Ideally, this would allow for $\hat{x}, \hat{z}$ polarized out-of-plane spin currents with the right choice of crystal orientation, expanding the compatibility of intrinsic SHE materials to a wider range of magnetic heterostructures.

Recent work with the non-collinear phase of cubic $IrMn_3$ seems to validate this notion of orientation dependence, showing a large and facet-dependent spin conductivity that is greater in amplitude than typical heavy metal systems [43]. Unfortunately, it was not possible to directly link this to the AFM order due to the large Néel temperature (T_N) for $IrMn_3$ close to 1000 K [44]. $PtMn_3$ shares the same non-collinear AFM ground state, but has a significantly lower Néel temperature ($T_N \sim 475$ K in bulk) [39] as well as a unique intermediate collinear AFM state with a first order phase transition around 360 K that is absent in $IrMn_3$ and $RhMn_3$ [45]. For the AHE, this link

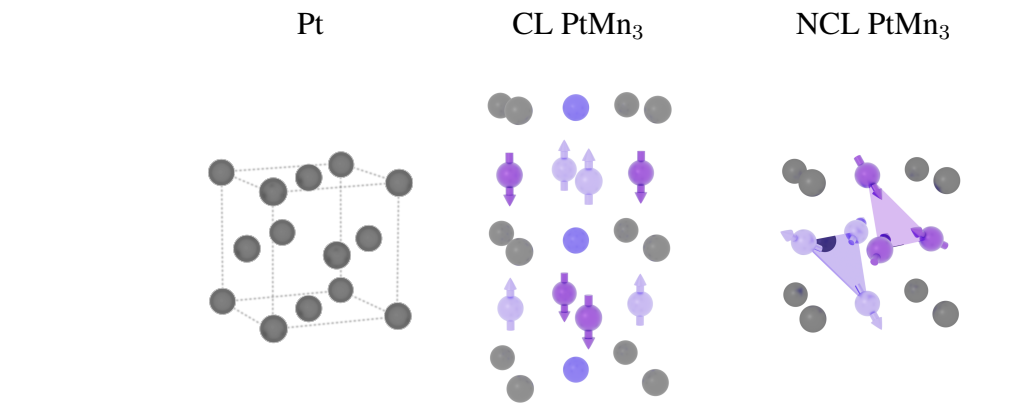

Laue Group	$m\bar{3}m1'$	$4'/mmm'$	$\bar{3}m'$
$\underline{\sigma}^x$	$\begin{pmatrix} 0 & 0 & 0 \\ 0 & 0 & \sigma^z_{xy} \\ 0 & -\sigma^z_{xy} & 0 \end{pmatrix}$	$\begin{pmatrix} 0 & 0 & 0 \\ 0 & 0 & \sigma^x_{yz} \\ 0 & \sigma^x_{zy} & 0 \end{pmatrix}$	$\begin{pmatrix} \sigma^x_{xx} & \sigma^y_{xx} & \sigma^x_{xz} \\ \sigma^y_{xx} & -\sigma^x_{xx} & -\sigma^y_{xz} \\ \sigma^x_{zx} & -\sigma^y_{zx} & 0 \end{pmatrix}$
$\underline{\sigma}^y$	$\begin{pmatrix} 0 & 0 & -\sigma^z_{xy} \\ 0 & 0 & 0 \\ \sigma^z_{xy} & 0 & 0 \end{pmatrix}$	$\begin{pmatrix} 0 & 0 & \sigma^y_{xz} \\ 0 & 0 & 0 \\ \sigma^y_{zx} & 0 & 0 \end{pmatrix}$	$\begin{pmatrix} \sigma^y_{xx} & -\sigma^x_{xx} & \sigma^y_{xz} \\ -\sigma^x_{xx} & -\sigma^y_{xx} & \sigma^x_{xz} \\ \sigma^x_{zx} & -\sigma^y_{zx} & 0 \end{pmatrix}$
$\underline{\sigma}^z$	$\begin{pmatrix} 0 & \sigma^z_{xy} & 0 \\ -\sigma^z_{xy} & 0 & 0 \\ 0 & 0 & 0 \end{pmatrix}$	$\begin{pmatrix} 0 & \sigma^z_{xy} & 0 \\ \sigma^z_{yx} & 0 & 0 \\ 0 & 0 & 0 \end{pmatrix}$	$\begin{pmatrix} \sigma^z_{xx} & \sigma^z_{xy} & 0 \\ -\sigma^z_{xy} & \sigma^z_{xx} & 0 \\ 0 & 0 & \sigma^z_{zz} \end{pmatrix}$

Figure 1.2: **Symmetry-enforced spin Hall conductivity tensors for magnetic phases of $PtMn_3$.** The allowed structure of spin Hall conductivity tensors $\underline{\sigma}^x$, $\underline{\sigma}^y$, $\underline{\sigma}^z$ versus magnetic Laue group for the three possible magnetic phases of $PtMn_3$. The tensors are most restricted in the high-temperature non-magnetic fcc metal phase, equivalent to fcc Pt, where they equate to the canonical spin Hall effect. At the onset of antiferromagnetism, the tensors become less restricted in the intermediate collinear (CL) and low-temperature non-collinear (NCL) antiferromagnetic states, with the NCL tensors being significantly less restricted. $PtMn_3$ above the Néel transition is non-magnetic and has the same global symmetry as fcc Pt. Symmetry-enforced tensor forms are pulled from [13].

with the magnetic order has been presently established, using both temperature and piezoelectric strain to move a $PtMn_3$ film out of the non-collinear AFM state and suppress the intrinsic AHE entirely [46]. In the framework of the non-spin-orbit coupling symmetry-imposed restrictions on the AHE/SHE, it is the intermediate collinear state that explicitly bars a non-zero AHE. If there is a measured SHE in the collinear phase, it is attributed entirely to spin-orbit coupling and is expected to be isotropic [38].

The possibility of unconventional $\hat{x}, \hat{z}$ polarized out-of-plane spin currents was also recently confirmed in the non-collinear antiferromagnets Mn_3GaN [15] and Mn_2Au [47]. Explicit computation of the out-of-plane spin Hall conductivities $\sigma^i_{xz}, i = (x, y, z)$ of Mn_3GaN corresponded well to their relative measured amplitudes, approximately 5-10% of the conventional σ^y_{xz}. The $\hat{x}, \hat{z}$ polarized spin currents were found to emerge smoothly through the Néel transition at $T_N \sim 345$ K, showing their explicit dependence on the magnetic texture [15]. As no general evaluation of the full SHC tensor for Mn_3GaN was performed, and electronic measurements were performed on a single device orientation, it is undetermined whether there is any dependence on crystal orientation to the σ^i_{xz}. In Mn_2Au, the σ^z_{xz} was found to be much more significant, up to 1.7x the conventional σ^y_{xz} [47]. In that study, devices were created with (Co/Pd) perpendicular anisotropy magnets, and it was shown that the Mn_2Au was able to deterministically switch them, although only at extremely high current densities $\sim 10^8$ A cm^{-2} (the switching result is somewhat controversial as current densities that high have been shown to irreversably damage devices and cause persistent thermal gradients which yield equivalent thermoelectric signals [48]). These initial works are exciting, and seem to verify the existance of unconventional spin Hall conductivity in non-collinear antiferromagnets. The $PtMn_3$ system promises similar phenomena, but has additional intermediate phases, which should make it possible to correlate these unconventional components not just with antiferromagnetic order, but with a particular *type* of it, in order to deduce the exact level of symmetry dependence. Additionally, $PtMn_3$ is expected to have an orientation-dependent anisotropy in the spin Hall conductivity which is strongest in the lowest-symmetry single domain non-collinear state. The near room temperature accessibility of three distinct magnetic textures (non-collinear, collinear, and non-magnetic) makes $PtMn_3$ a uniquely suitable material for studying the link between intrinsic AHE/SHE that originate from magnetic Berry curvature.

1.4 Orientation-dependent Composite Spin Hall Conductivity in $PtMn_3$

Detailed theoretical work computing the intrinsic spin Hall conductivities in the cubic XMn_3 (X=Rh, Ir, Pt) materials shows highly isotropic spin conductivity, and large non-zero amplitudes for all polarizations, comparable to or exceeding intrinsic SHE in high spin-orbit coupling metallic systems [33]. Compared to high symmetry non-magnets with high spin-orbit coupling (e.g. fcc Pt, Laue group $m\bar{3}m1'$), which have spin Hall conductivity tensor components restricted to that of the canonical spin Hall effect (e.g. only σ^y_{xz},$-\sigma^z_{xy}$ contributions for an applied current along $\hat{x}$), the reduced symmetry of the cubic $PtMn_3$ non-collinear state (Laue group $3\bar{m}'$) allows for additional transverse and also longitudinal spin conductivity for multiple spin polarizations [13]. Further-

more, the conductivities can be anisotropic with respect to current orientation, potentially allowing for selection of preferred spin current direction and polarization [33,43].

Using previously calculated spin Hall conductivity tensors for the non-collinear antiferromagnetic state of $L1_2$ $PtMn_3$ in the high symmetry basis [33], the out-of-plane σ^i_{xz} and longitudinal σ^i_{xx} spin conductivities are calculated for (001)-oriented $PtMn_3$ thin films with devices patterned along an in-plane direction $\hat{x}$ in Figure 1.3. For a single antiferromagnetic domain with (111)-oriented Kagome planes, the orientation-dependent anisotropy in each spin polarization is high, and allows for selection of a dominant component by orienting device channels appropriately. Unfortunately, devices with multiple domains, where the Kagome planes are aligned to some combination of (111)-eqivalent directions, increase the global symmetry and potentially eliminate the unconvential components of the spin Hall conductivity entirely. For example, in the highest symmetry configuration where all eight possible domains are present, only the typical σ^y_{xz} is non-zero (see Figure A.1). The calculation methodology and source code for the orientation-dependent σ^i_{xz}, σ^i_{xx} in the low-temperature non-collinear phase of $PtMn_3$ is provided in section A.

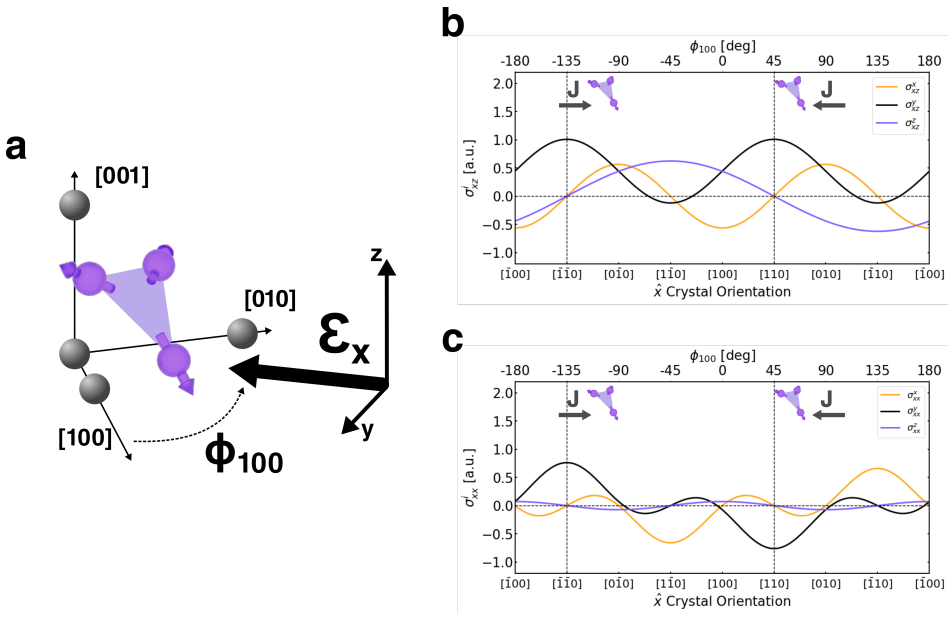

Figure 1.3: **Anisotropic spin Hall conductivity in (001)-oriented $PtMn_3$.** **a** Coordinate system for thin film $PtMn_3$ Hall bar devices with coordinates $\hat{x}, \hat{y}, \hat{z}$ patterned in the (001) plane with some angle ϕ_{100} from the [100] crystal orientation. **b** Estimated out-of-plane spin Hall conductivities σ^i_{xz} and **c** longitudinal spin conductivities σ^i_{xx} for spin current polarizations $i = x, y, z$ versus crystal orientation/ϕ_{100}, assuming a single non-collinear antiferromagnetic domain with (111)-oriented Kagome planes. Conductivity tensor components were calculated using prior results [33], and rotating into the Hall device coordinates (see section A, and calculations for multiple domains in Figure A.1).

In this work, L12 ordered (001)-oriented $PtMn_3$ thin films are synthesized in isolation and in heterostructures with Permalloy (Py, here approximately $Ni_{80}Fe_{20}$) to measure the anomalous (σ_{xy}) and out-of-plane spin conductivities ($\sigma^i_{xz}, i \in (x, y, z)$) in each of the accessible antiferromagnetic phases, and to explicitly correlate them with magnetic order and show the expected anisotropy in the spin Hall conductivity. The observed maximum spin torque efficiencies ($\xi = J_S/J_e \sim 0.3$) from the unconventional $\hat{x}, \hat{z}$ polarized out-of-plane spin currents are significantly larger than the traditional $\hat{y}$ polarized out-of-plane spin current in Pt ($\xi \sim 0.1$), which is promising for efficient switching of magnetic devices and devices with selectable spin polarization components.

The synthesis of $L1_2$ ordered $PtMn_3$ thin films via RF magnetron sputtering is described in detail in chapter 2, as is the structural and chemical characterization via X-ray and neutron methods. The magnetic characterization of the antiferromagnetic phases of $PtMn_3$ via neutron diffraction, reflectometry, and anomalous Hall effect measurements is shown in chapter 3. The measurement of spin torques in $PtMn_3$/Py heterostructures is covered in chapter 4, as is the component fitting and the extraction of spin torque effective fields from $\hat{x}, \hat{y}, \hat{z}$ polarized out-of-plane spin currents versus temperature and antiferromagnetic phase of $PtMn_3$. Finally, the complete work is summarized in chapter 5, and an outlook is given for experimental advances in controlling non-collinear antiferromagnetic domain formation, the prospect of quantum self-inductance, and integration in heterostructures with perpendicular magnetic anisotropy ferromagnets.

CHAPTER 2

Growth, Structural, and Chemical Characterization of $PtMn_3$ Thin Films

2.1 Growth of Ordered $PtMn_3$ Thin Films via Magnetron Sputtering

Growth of an ordered intermetallic thin film of a particular composition and ordering is generally challenging due to complicated crystal phase spaces. For the Pt-Mn system below 1000 °C (about the maximum possible in our thin film growth facilities), there are four ordered phases in this temperature range [39, 49, 50], and large composition and temperature windows where dual phases, solid solutions, and eutectic phases can exist [51]. This particular system is additionally difficult due to the vastly different chemistry and growth kinetics of Pt and Mn. For example, Mn will adhere readily to oxide substrates and template accordingly, and has a low vapor pressure of 950-1350 °C at process gas pressures of 7-70 mTorr (∼1-10 Pa) [52], making precise control challenging in high-energy growth methods like pulsed laser deposition. In contrast, Pt has a very high vapor pressure of 2050-2350 °C in the same conditions (7-70 mTorr process gas) [52], and is significantly less reactive. In general for Pt, the adatom-substrate adhesion is poor can lead to discontinuous films and unwanted (111) phase formation if the film is not deposited at a high enough growth rate [53]. Growth of high quality intermetallic Pt-Mn films requires a precise tuning of deposition conditions, and the method of choice here is RF magnetron sputtering, due to relatively low incident atom energy and a high degree of tunability. A schematic of a modern magnetron sputtering system is shown in Figure 2.1a. There are many parameters that influence film growth, including substrate temperature, process gas pressure and the plasma power density on the surface of the sputtering target (an excellent resource on sputtering growth and the behavior of the Ar plasma and target plumes can be found in Ref. [54]). For ordered $PtMn_3$ growth, two primary parameters are tuned. First, the relative Mn composition is tuned with Ar process gas

pressure, as shown in Figure 2.1b. As Mn is a significantly lighter element that Pt, it preferentially scatters in the transverse direction and the forward concentration of Mn in the sputtering plume decreases with higher process gas pressure. Second, the crystallinity of a sample with a tuned incident species stoichometry can be controlled with substrate temperature, shown in Figure 2.1c, as per the bulk phase diagram [51] and surface adatom kinetics.

To obtain the desired low temperature non-collinear antiferromagnet state, and the spin Hall conductivity behavior outlined in Figure 1.3, the thin films must have high $L1_2$ ordering, as per Figure 2.2a. Intermetallics are generally challenging to characterize, due to the ease which constituent elements can alloy into different phases, and the structural similarity between them. For example, the simulated $2\theta - \omega$ XRD spectra for likely (001)-oriented Pt-Mn thin films in the relevant growth parameter range is shown in Figure B.1. As seen in the temperature dependent profiles in Figure 2.1c, it is easy to conflate these phases if the film is not the ideal single crystal. Generally, both structural and chemical characterization must be done to confirm the film phase, though for the lower temperature growths below 650 °C, the relative ratios of the 001 and 002 XRD peaks suggest that the films are exclusively some combination of the $L1_2$ and γ phases (see discussion around Figure 2.2b.

The (001)-oriented thin film $PtMn_3$ samples in this work with the highest $L1_2$ ordering on either $SrTiO_3$ or MgO substrates were grown via RF magnetron sputtering from a 1" metallic target of 6:1 Mn:Pt at 45 W gun power, 630-650 °C substrate temperature, 5" target-substrate distance, and in 10-13 mTorr (1 mTorr = 0.133 Pa) of Ar at approximately 1.5 nm/min. For growths on MgO, the substrate was pre-baked at 950 °C for 1h in high vacuum (typically $< 10^{-6}$ Torr). For growths on $SrTiO_3$, the substrate was pre-baked at 630-650 °C for 30 minutes in 50 mTorr Ar to reduce oxygen vacancy formation in the substrate surface. Permalloy films were deposited at room temperature from a 2" target of $Ni_{80}Fe_{20}$ at 100 W, approximately 5" target-substrate distance, and in 10 mTorr of Ar at approximately 2.5 nm/min. For capping with SiC or TiO_2, the sample was removed from the chamber and placed in a high vacuum pulsed laser deposition chamber within 1 minute of sample removal for capping film deposition.

2.2 Structural Characterization of $PtMn_3$ Thin Films

The thin film $PtMn_3$ crystal structure was characterized by X-ray diffraction (XRD) in a Rigaku SmartLab diffractometer equipped with a Ge(220)×2 monochromator to select for Cu Kα X-rays. XRD ϕ scans were obtained by aligning to 024 peaks of the substrates and film. Reciprocal space mapping was done by aligning to the substrate 024 peaks and scanning in $2\theta, \omega$ in approximately 3 degree fields of view and 0.1 degree resolution. To quantify the ordering fraction, the relative

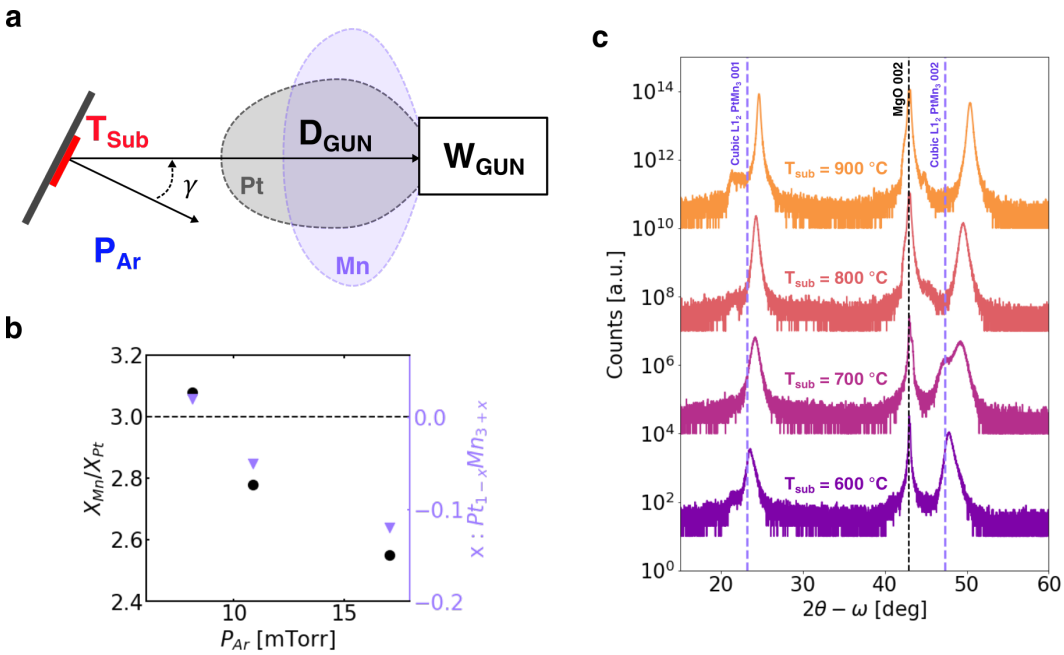

Figure 2.1: **Synthesis of Thin Film $PtMn_3$ With RF Magnetron Sputtering**. **a** General schematic of RF magnetron sputtering system with sputtering gun/source target assembly (right), and substrate holder assembly (left). The exact composition and crystallinity of the films can be tuned with multiple process inputs including substrate temperature (T_{sub}), Ar process gas pressure (P_{Ar}), RF plasma power (W_{gun}), gun-substrate distance (D_{gun}), and their relative angle (γ). **b**, The chemical composition can be tuned with P_{Ar} due to the difference in relative scattering rates of Pt and Mn with Ar. **c**, The crystallinity is generally tuned with substrate deposition temperature, which can also change the composition due to the relatively low vapor pressure of Mn in high vaccuum conditions.

intensity of the out-of-plane 001 and 002 $PtMn_3$ XRD peaks is compared to the ideal crystal with 100% ordering. To extract the intensities, Voigt profiles are fit to the substrate and $PtMn_3$ XRD peaks. For the 001, 002 XRD peaks, $I_{001}/I_{002} = S^2 r_0$, where S is the ordering fraction, and r_0 = 0.938 is the ratio for the fully ordered crystal. In all samples used in this study, $S_{STO} \in [0.7, 0.91]$, with thinner films typically exhibiting higher ordering fractions. In contrast, $S_{MgO} \in [0.55, 0.65]$ for all measured films, which is significantly lower. A representative X-ray diffraction (XRD) $2\theta - \omega$ scan of a 95 nm $PtMn_3$ film on $SrTiO_3$, as well as a φ scan of the substrate and $PtMn_3$ 024 peaks, is shown in Figure 2.2b. The $PtMn_3$ films are predominantly (001)-oriented, with thicker films showing detectable amounts of (111) oriented domains (though these are consistently $< 1\%$ of the total film volume, as per their integrated XRD peak intensity ratios). The ordering fraction of the $PtMn_3$ film shown in Figure 2.2b is $S = 0.91$, with the rest of the film assumed to be the solid solution γ-$PtMn_3$.

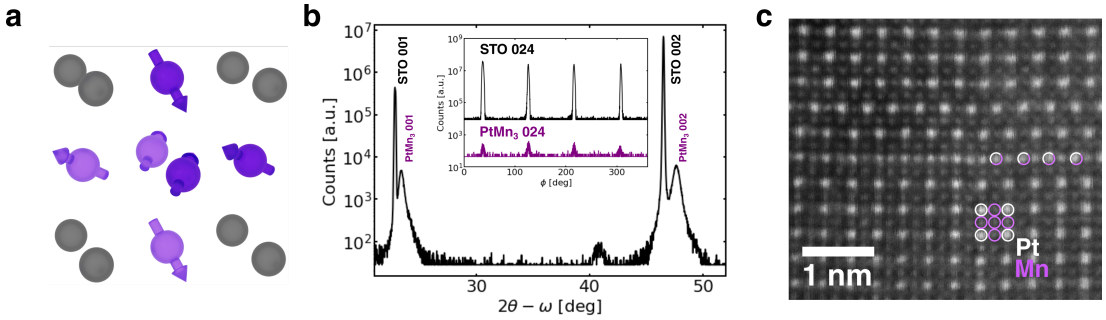

Figure 2.2: **Atomic ordering of $PtMn_3$ thin films on (001)-oriented $SrTiO_3$.** **a**, The low temperature non-collinear AFM state of $L1_2$ ordered $PtMn_3$ with Pt on the vertices (gray) and Mn on the face sites (purple). **b**, XRD of 001 $PtMn_3$ on $SrTiO_3$ (STO) with ϕ scan (inset). **c**, HAADF-STEM micrograph of representative $PtMn_3$ thin film showing Pt (white), Mn (purple), and occasional Mn/Pt antisite defects (white/purple). Thin films on $SrTiO_3$ exhibit $L1_2$ ordering fractions of 0.70-0.91 with thinner films typically having higher ordering. HAADF-STEM data obtained in collaboration with G.A. Pan [55].

Ordered $PtMn_3$ grown on $SrTiO_3$ are largely single crystal (001) phase, with no in-plane twinning (see Figure B.2b-c). Due to the near identical in-plane lattice constant of the $PtMn_3$ film to the $SrTiO_3$ substrate, it is difficult to resolve peaks with higher relative Q_x components. To compensate, the higher-Q_z 024 peaks are used for both XRD ϕ scans and reciprocal space mapping (RSM). RSMs of the 024 peaks for $PtMn_3$ on MgO and $SrTiO_3$ are shown in (see Figure B.2d-e), respectively, and provide fitted in-plane and out-of-plane lattice parameters from the peak centers. Due to the large in-plane lattice mismatch, the $PtMn_3$ and MgO peaks are well separated, but exhibit the highest tetragonal strain, approximately -1.1% out-of-plane and +1.8% in-plane compared to the ideal cubic system ($a = c = 3.84$Å). The $PtMn_3$ films on $SrTiO_3$ have relatively reduced strains of -0.6% out-of-plane and +1.6 % in-plane, and are exclusively used for transport measurements in this work.

High-angle annular dark field scanning transmission electron microscopy (HAADF-STEM) images of the same 95 nm $PtMn_3$ film is shown in Figure 2.2c. Over the imaged region, the films are single crystal, (001)-oriented, and $L1_2$ ordered, although occasional antisite defects are observed. Further HAADF-STEM images of the $SrTiO_3$/$PtMn_3$(46.6 nm)/Py(6.8 nm)/SiC sample used for harmonic Hall effect measurements are shown in Figure 2.3 (see Methods in Ref. [55]). Overall, the $PtMn_3$ exhibits high crystallinity persisting through the entire thickness of the thin film ($\sim$ 45 nm). The $PtMn_3$ film is epitaxially templated to the $SrTiO_3$, although there is disorder observed at the interface (see Figure 2.3c). The films also have occasional half unit-cell offset dislocations, as well as regions of solid solution face-centered-cubic γ-$PtMn_3$ with a typical antisite defect of top/bottom face manganese substituted with platinum which is most pronounced near the substrate-film interface and less common defects appear less near the top $PtMn_3$/Py interface. It

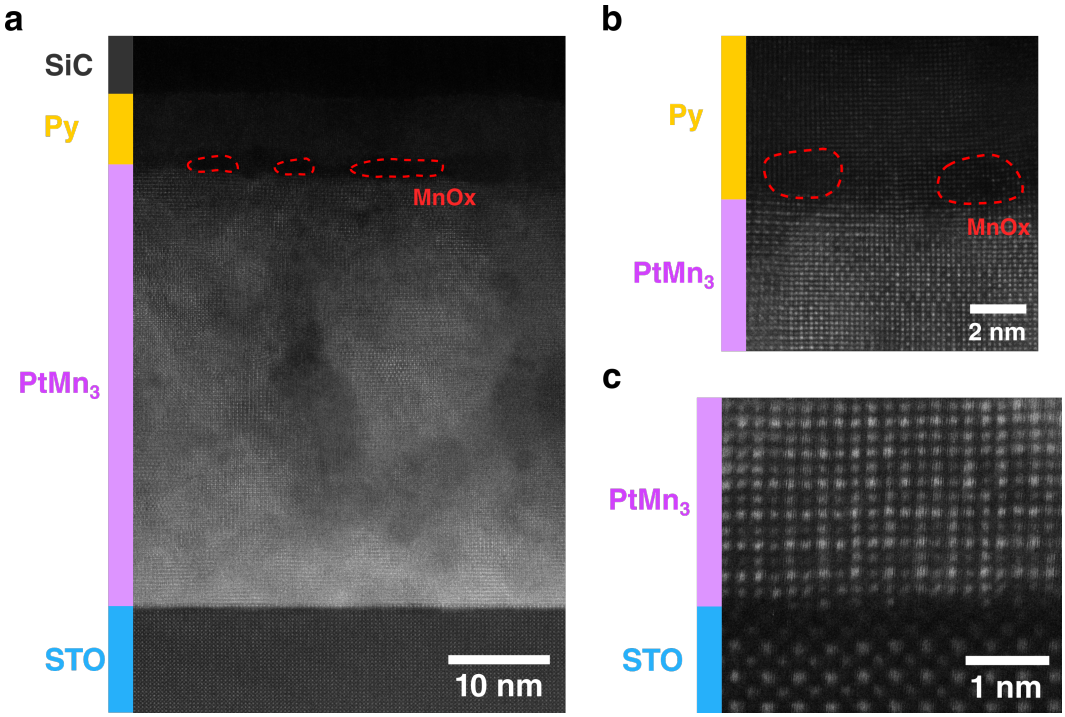

Figure 2.3: **HAADF-STEM of $PtMn_3$/Py film stack for harmonic Hall effect measurements**. **a**, Large field-of-view HAADF-STEM image of $SrTiO_3$/$PtMn_3$(46.6 nm)/Py(6.8 nm)/SiC used for harmonic Hall effect measurements. **b**, Top interface between $PtMn_3$ and Py showing good $L1_2$ ordering and interface smoothness. **c**, Bottom $PtMn_3$ and $SrTiO_3$ interface, showing increased solid solution phase with typically reduced Mn stoichiometry ($PtMn_{2.0}$). Pockets of MnO_x are present near the surface, here 1-2 unit cells thick and in disconnected regions. HAADF-STEM data obtained in collaboration with G.A. Pan [55].

is possible that the prevalence of antisite defects near the substrate/$PtMn_3$ interface is a method of strain relaxation due to the substrate lattice mismatch ($\epsilon \sim +1.7\%$), as platinum (a = c = 3.93 Å) expands the lattice constant of $PtMn_3$. It is possible that the larger strain relaxation requirements for $PtMn_3$ films on MgO is the cause of the consistently lower $L1_2$ ordering fraction in films on MgO.

Typically, a post-growth annealing strategy would be employed to improve the ordering fraction and overall crystallinity, as was done in a prior work with $PtMn_3$ films on $BaTiO_3$ [46]. Due to the relatively low vapor pressure ($\sim$ 950-1350 °C) [52] of Mn at high vacuum conditions however, loitering at high temperatures post growth leads to the formation of a surface cubic manganese layer with a depth of 2-5 nm, and forms sparse ridges of Mn across the film surface (see Figure B.5). For this reason, post-growth annealing was not done for any samples destined for electronic measurement in order to avoid large Mn ridges shunting current within or between patterned devices. EELS spectroscopic imaging of an example surface manganese region is shown in Figure B.4. The pockets of Mn at the surface are almost exclusively cubic MnO_x, and therefore all electronic

measurements are kept above 120 K to avoid a parasitic antiferromagnetic signal from potential clusters of MnO ($T_N \sim 115$ K). As MnO_x is a good insulator, the effect of these regions on the interfacial spin current diffusion is expected to be minimal, as interfacial oxides have been shown to have high interface spin transparency in the kinds of vertical heterostructures employed here [56]. The source of the oxidiation in the surface manganese is currently unclear, and may possibly occur ex-situ during the transfer of the sample lamella into the STEM. Nevertheless, even if the manganese were to be fully metallic in the as-grown state, only a fractional suppression of interface spin current would be expected, both as per prior studies with continuous 3d transition metal spacers of a similar thickness [57] and because it is discontinuous. To reduce possible inhibition of spin current diffusion across the $PtMn_3$/Py interface from an interfacial manganese layer, the samples used for the harmonic Hall effect measurements were not subject to a post-deposition anneal, and were cooled immediately to room temperature in 50 mTorr Ar process gas. Despite the precaution, these samples still show discontinuous 1-2 nm thick surface manganese regions, as shown in Figure 2.3a-b. In general, there is a direct tradeoff between lowering the growth temperature (and therefore manganese diffusion) and $L1_2$ ordering fraction.

2.3 Chemical Characterization of $PtMn_3$ Thin Films

In addition to crystalline order, the chemical composition of $PtMn_3$ has a direct effect on magnetic order. Small differences in Mn stoichiometry can move the Néel and first-order transition temperatures around by 50-100 K, and even suppress the formation of the noncollinear AFM phase [39]. Chemical characterization of $PtMn_3$ thin films was done through X-ray photoelectron spectroscopy (XPS) and neutron reflectometry. The primary use of XPS here was to gauge the film stoichiometry within a few nm of the surface. Higher detail cross-sectional composition is obtained with neutron reflectometry through the extracted nuclear scattering length density (SLD) profile.

XPS spectra were obtained using a Kratos Axis Ultra XPS with a monochromated Al source and a charge neutralizer (neutralizing surface charge buildup is mandatory when samples are on insulating substrates). High-resolution scans were taken about the Mn 2p and Pt 4f peaks, and the integrated intensities of the Mn 2p 1/2 peak and both Pt 4f peaks were compared to those from a reference 6:1 Mn:Pt target to establish film stoichiometry. The background of the full Mn 2p peak is more difficult to consistently select boundaries for, and so only the Mn 2p 1/2 peak is chosen for integration in order to make evaluation between samples more consistent. Sample XPS spectra for the Mn 2p and Pt 4f peaks are shown in Figure 2.4, and are as expected for non-oxidized metallic peaks (see Ref. [58] for expected spectra with Al Kα X-rays).

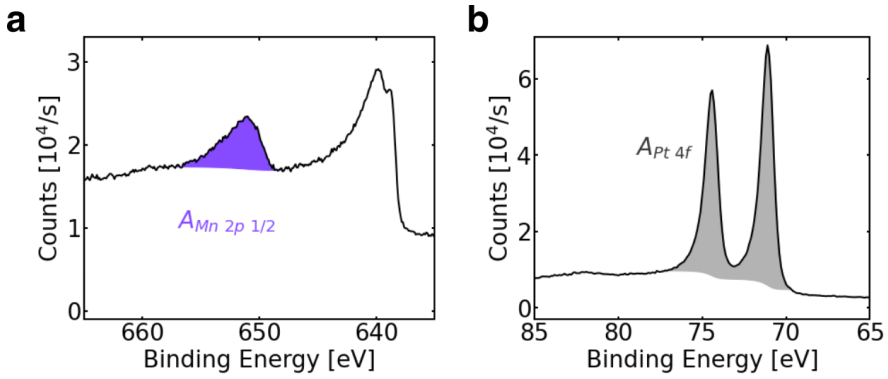

Figure 2.4: **X-ray Photoelectron Spectroscopy of Representative Mn and Pt Peaks for $PtMn_3$ on $SrTiO_3$.** **a**, The Mn 2p complex and quantification region (Mn 2p 1/2 peak, shaded purple), and **b** the Pt 4f complex and quantification region (shaded gray). Integrated peak intensity ratios are normalized to a reference target for quantification (see Figure B.3).

In general, $PtMn_3$ thin film samples were capped with SiC or TiO_2 to prevent long-term oxidation and required *in situ* rasterized ion milling with a beam of Ar ions during XPS measurements in order to sample the Mn and Pt peaks with a high signal-to-noise ratio. As per the discussion around Figure 2.1, there is a higher preferential sputtering rate for Mn, and so the ion milled area is not representative of the bulk Mn stoichiometry of the surrounding film. To compensate for this, a baseline calibration was performed on the backside of a 6:1 Mn:Pt sputtering target with known composition. The XPS spectra for the reference target, as well as a broad survey showing the effect of surface sputtering on the XPS profile, is shown in Figure B.3. Once the integrated peak areas $A_{Mn,Pt}$ shown in Figure 2.4 are obtained, the relative Mn stoichiometry $R = X_{Mn}/X_{Pt}$ can be quantified:

$$R = c\frac{3 \cdot A_{Mn/2p/1/2}/RSF_{Mn}}{A_{Pt4f}/RSF_{Pt}} \tag{2.3.1}$$

where $RSF_{Mn,Pt}$ are the relative sensitivity factors for each element to normalize for transition probabilities per atom of each element (see Appendix F. in [58]. Note that the Mn contribution is multiplied by 3 to account for the ignored Mn 2p 3/2 area). For the reference target, R is set to 6.0, and a calibration constant of $c = 1.306$ is obtained. In subsequent thin film scans, this constant is used to calculate R. For all grown $PtMn_3$ films, deposition conditions were tuned (see discussion around Figure 2.1b) to target a slight Mn deficiency (x = -0.07 for $Pt_{1-x}Mn_{3+x}$) in order to reduce transition temperatures below 400 K to make them more accessible for electronic measurements(see Fig. 4 in Ref. [39]). For the $PtMn_3$ thin films on $SrTiO_3$ used for harmonic Hall effect measurements, XPS spectra yield a stoichiometry of approximately $PtMn_{2.77\pm0.07}$ (x = -0.06 $\pm$ 0.02 for $Pt_{1-x}Mn_{3+x}$) near the surface of the film, within the target range.

In contrast to XPS, which is limited to the surface of the sample due to the high diffuse scattering of emitted electrons, neutron reflectometry can yield full depth profile of the $PtMn_3$ film composition due to the high neutron transparency of most materials. Unpolarized neutron reflectometry measurements were performed on a $SrTiO_3$/$PtMn_3$(95 nm)/SiC(20 nm) heterostructure using the CANDOR instrument at the NIST Center for Neutron Research (see Methods in Ref. [55]). The unpolarized neutron reflectivity, which is sensitive to the nuclear scattering length density (SLD), was measured as a function of the momentum transfer vector Q along the film normal. The reflectivity and resulting SLD profile for a $SrTiO_3$/$PtMn_3$(95 nm)/SiC(20 nm) sample are shown in Figure 2.5. The fitted scattering length density is related to the composition of $Pt_{1-x}Mn_{3+x}$ by

$$\text{SLD} \;=\; 10\frac{((3+x)b_{Mn}+(1-x)b_{Pt})}{a^2c} \tag{2.3.2}$$

where b_{Mn}, b_{Pt} are the respective nuclear scattering lengths, in fm, and a, c are the lattice constants in Å (a=c=3.84 Å for the cubic system). The resulting SLD profiles yield a Pt-rich transitional growth region of 18.4 $\pm$ 0.3 nm with an approximate stoichiometry of $PtMn_{2.0}$, followed by a uniform "bulk-like" layer of near optimal stoichiometry, approximately $PtMn_{2.7}$ (see Figure 2.5c). This transition region likely exists due to the large lattice mismatch ($\sim$ 1.8% in-plane lattice mismatch between (001)-oriented $SrTiO_3$ and bulk cubic $PtMn_3$), which favors a γ phase with reduced manganese stoichiometry to relax the epitaxial strain. The existence of this transition region necessitates $PtMn_3$ films thicker than 20 nm for harmonic Hall effect measurements, to ensure high $L1_2$ ordering near the top interface with Py. For X_{Mn}/X_{Pt} = 3.0, the expected SLD = -0.282 $\cdot$ 10^{-6}Å^{-2} for the bulk cubic system and SLD = -0.275 $\cdot$ 10^{-6}Å^{-2} for tetragonal films on MgO and $SrTiO_3$ with the measured a, c from X-ray diffraction (see Figure B.2). There is a Pt-rich transitional growth region of thickness 18.4 nm $\pm$ 0.3 nm and nuclear SLD of 0.471 $\cdot$ 10^{-6}Å^{-2} $\pm$ 0.007 $\cdot$ 10^{-6}Å^{-2} near the $SrTiO_3$ interface. The SLD of the thicker, more bulk-like, $PtMn_3$ layer in this case was -0.08 $\cdot$ 10^{-6}Å^{-2} $\pm$ 0.02 $\cdot$ 10^{-6}Å^{-2}. Both SLD values indicate that the film grown on $SrTiO_3$ is slightly more Pt-rich than the sample grown on MgO, with x = -0.326 $\pm$ 0.003 for the transition layer ($Pt_{1-x}Mn_{3+x} \sim PtMn_{2.0}$) and x = -0.084 $\pm$ 0.019 for the bulk of the film ($\sim$ $PtMn_{2.70}$), in good agreement with the XPS result of $PtMn_{2.77\pm0.07}$.

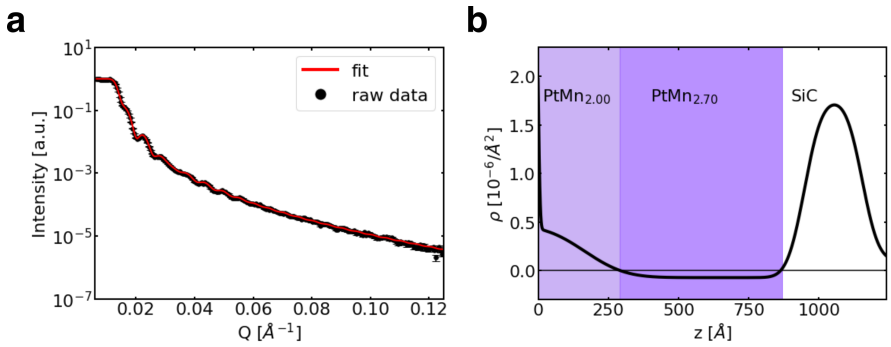

Figure 2.5: **Unpolarized Neutron reflectivity of $PtMn_3$ on $SrTiO_3$.** **a**, Reflectivity profile of $SrTiO_3$/$PtMn_3$(95 nm)/SiC(20 nm) and **b**, the resulting nuclear scattering length density (SLD). Both MgO and $SrTiO_3$ samples show a 15-20 nm transition region with reduced Mn stoichiometry, followed by an approximately stoichiometric "bulk" region for the rest of the film. This data was obtained in collaboration with A.J. Grutter and R.F. Need [55].

CHAPTER 3

Magnetic Characterization of $PtMn_3$ and $PtMn_3$/Py Thin Films

3.1 Neutron Diffraction of $PtMn_3$ Thin Films on MgO

To probe the antiferromagnetic order in the $PtMn_3$ thin films directly, neutron diffraction measurements of the 101 peak on the BT-7 and BT-4 triple axis spectrometers were performed at the NIST Center for Neutron Research (see Methods in Ref. [55]). Measurements were carried out in a temperature range of 100-420 K in a closed-cycle refrigerator. Though the $L1_2$ ordering on $SrTiO_3$ is markedly higher, a distinct 101 $PtMn_3$ peak was not resolved due to the high overlap with the substrate. Unlike the XRD RSM measurements (see Figure B.2), the Q range of higher order peaks (e.g. 024 or equivalent) is out of the measurement range. For this reason, the temperature dependent neutron diffraction measurements were performed on MgO/$PtMn_3$ samples as the in-plane peak separation is higher than with the samples on $SrTiO_3$ and MgO does not have 001 and 003 peaks. The temperature dependent neutron diffraction measurements of the 101 $PtMn_3$ peak are shown in Figure 3.1a. The integrated peak intensities and their standard errors are extracted via gaussian fits to each profile using the DREAM algorithm [59] in the Bumps python package (v0.8.0) [60] (see section E for example use). The peak intensities are plotted versus temperature in Figure 3.1b. The order parameter $M(T)$ was fit to the temperature dependent intensity within 100 K of T_N with $I_{101} = M_{101}^2 \left(\frac{(T_N - T)}{T_N}\right)^{2\beta} + I_0$, where M_{101} is a scattering intensity proportional to the Fourier component of the magnetic lattice for the 101 Q vector, and I_0 is the background intensity from incoherent scattering. The fit yields T_N = 403 $\pm$ 2 K, and β = 0.358 $\pm$ 0.032, which is within the expected range for a 3D Heisenberg AFM ($\beta \sim 0.37$). The variance in β could be well explained by the large γ-$PtMn_3$ content in the MgO samples (40% by volume) and the tendency to form isolated planes of Mn in this phase, as per Figure 2.2c, which would result in mixed 2D/3D AFM behavior. Compared to the ideal bulk cubic material (T_N = 450-475 K [39]), the $PtMn_3$ films

on MgO also have a T_N that is approximately 50 K lower.

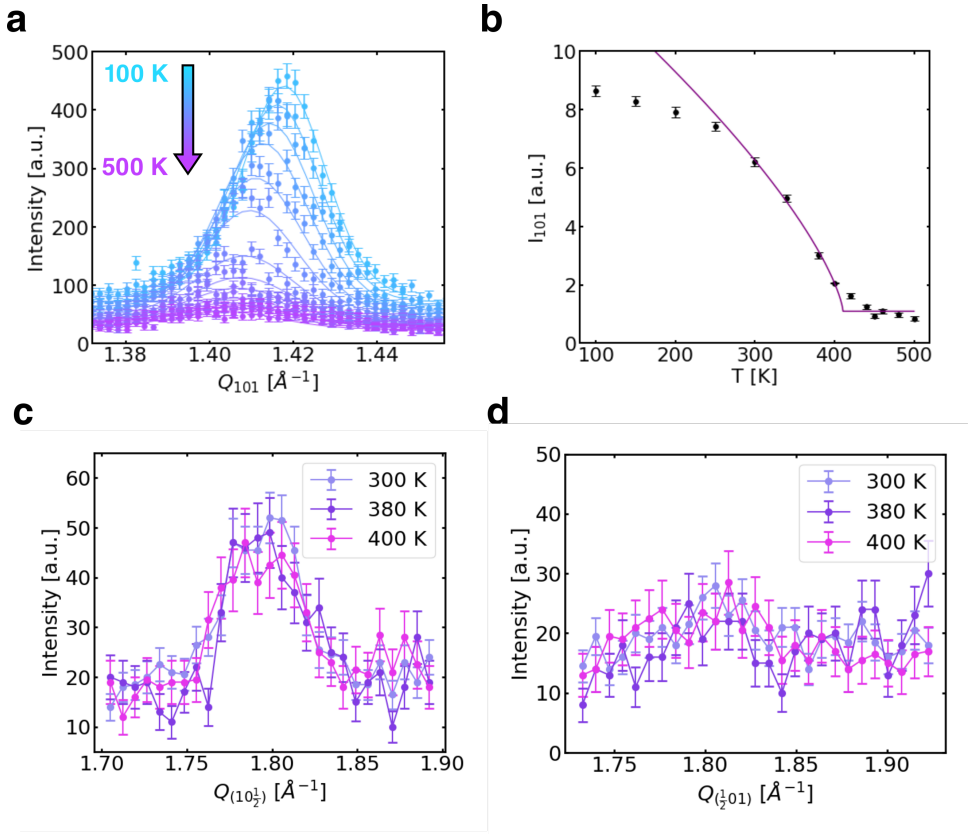

Figure 3.1: **Neutron diffraction of (001)-oriented $PtMn_3$ on MgO**. **a**, Temperature dependent neutron diffraction of the 101 $PtMn_3$ peak for MgO/$PtMn_3$(152 nm)/Py(8.9 nm)/TiO_2. **b**, Order parameter fit to 101 peak amplitudes with T_N = 403(2) K and β = 0.358(32) near T_N, in good agreement with a 3D Heisenberg system. In general, the $PtMn_3$ films on MgO and $SrTiO_3$ exhibit tetragonal strain and have lower transition temperatures compared to the bulk cubic film. **c**, $10\frac{1}{2}$ and **d**, $\frac{1}{2}01$ diffraction peaks in the same system on MgO showing no change in amplitude between 3 K - 400 K. The difference in peak height between $10\frac{1}{2}$ and $\frac{1}{2}01$ is attributed to slight misalignment due to temperature dependent tetragonal strain. The lack of Néel or first order transition for these peaks suggests total suppression of the collinear AFM phase in films grown on MgO. Error bars represent ± 1 standard deviation. Neutron diffraction data was obtained in collaboration with A.J. Grutter and R.F. Need [55].

In the $PtMn_3$ on MgO, there was no apparent first-order transition in the 101 neutron peak, as there was in a prior bulk study [39]. To determine which antiferromagnetic phase was present below the Néel transition, temperature dependent neutron diffraction of the half order $10\frac{1}{2}$ and $\frac{1}{2}01$, characteristic of the double-cell collinear AFM phase [39], was performed from 300-400 K. Unlike the clear second-order behavior of the 101 peak shown in Figure 3.1a-b, the intensity of the $10\frac{1}{2}$ peak (Figure 3.1c) is temperature independent, as is the $\frac{1}{2}01$ peak (Figure 3.1d). This contrasts

with neutron diffraction measurements of bulk $PtMn_3$ crystals, which show an obvious first-order transition between non-collinear and collinear phases between 300-400 K depending on the Mn stoichiometry [39]. For the $PtMn_3$ films on MgO, the evidence points towards a smooth second order phase transition from the non-collinear phase to a magnetically disordered phase above 404 K. The disappearance of the collinear phase for these highly strained films is not completely surprising, as it also disappears in other alloys in this family such as $RhMn_3$ [61]. The emergence of the collinear and non-collinear phases, as well as the associated Néel and transition temperatures are clearly sensitive to chemical composition and lattice strain, commensurate with prior studies [39].

In contrast to films grown on MgO, neutron diffraction on $SrTiO_3$/$PtMn_3$ samples represents a significant challenge, as the films are epitaxially strained in-plane to closely match the $SrTiO_3$ lattice constant of 3.905 Å. Relative to films on MgO, the substrate/film peak separation is also substantially reduced along the c-axis, with a $PtMn_3$ lattice constants of 3.82 Å along this direction, as shown in Figure B.2e. Such separation is generally insufficient to separately resolve a 101 thin film peak using neutron diffraction. A high-resolution measurement of a 95 nm $PtMn_3$ film on $SrTiO_3$ was attempted with CANDOR, the white beam reflectometer/diffractometer at the NIST Center for Neutron Research. Unfortunately, the tail of the $SrTiO_3$ 101 peak overwhelmingly dominates the signal near the $PtMn_3$ 101 peak position even for extremely tight beam collimation, and it was not possible to separate the two for analysis.

3.2 Polarized Neutron Reflectometry of $PtMn_3$ Thin films on MgO

The neutron reflectometry measurements of $PtMn_3$ films on STO (see discussion around Figure 2.5), gave a compositional profile of the film cross section that confirmed the desired stoichiometry in the bulk portion of the film. In addition to confirming the stoichiometry, proving that the $PtMn_3$ thin films have no ferromagnetisim and are completely antiferromagnetic is important in establishing the origin of the measured intrinsic spin Hall conductivity. Polarized neutron reflectometry measurements were performed using the PBR instrument at the NIST Center for Neutron Research (see Methods in Ref. [55]). The polarized measurements were performed on a MgO/$PtMn_3$ (150 nm)/Py (9 nm)/TiO_2 (6 nm) heterostructure at room temperature in an applied magnetic field of 3 T. Incident and scattered neutrons were spin-polarized parallel or antiparallel to the applied magnetic field, and data was corrected for imperfect beam polarization and spin-flipper performance. The spin-dependent reflectivity was measured as a function of the momentum transfer vector Q along the film normal. The fitted neutron reflectivity profiles for a MgO/$PtMn_3$(152

nm)/Py(8.9 nm)/TiO_2(6 nm) sample are shown in Figure 3.2a (see Methods in Ref. [55]). There is no evidence for a net magnetization in the $PtMn_3$, as per the spin asymmetry of the reflectivity profiles (Figure 3.2b) and the resulting magnetic SLD profile (Figure 3.2c). As with the fitting to the unpolarized reflectivity from the films on $SrTiO_3$, obtaining a high-quality fit to the data required breaking up the $PtMn_3$ into two separate layers, with a 15.5 nm $\pm$ 0.5 nm thick transition growth region. This transitional growth region exhibits a higher nuclear SLD ($0.317 \cdot 10^{-6}\text{Å}^{-2} \pm 0.084 \cdot 10^{-6}\text{Å}^{-2}$ than the bulk $PtMn_3$ layer ($-0.30 \cdot 10^{-6}\text{Å}^{-2} \pm 0.02 \cdot 10^{-6}\text{Å}^{-2}$). For the MgO sample, we find that x = -0.258 $\pm$ 0.037 for the transition layer ($Pt_{1-x}Mn_{3+x} \sim PtMn_{2.18}$) and x = 0.010 $\pm$ 0.008 for the bulk of the film ($\sim PtMn_{3.04}$). As previously discussed in chapter 2, the lowered Mn content near the substrate interface is postulated to be a method of lattice parameter relaxation.

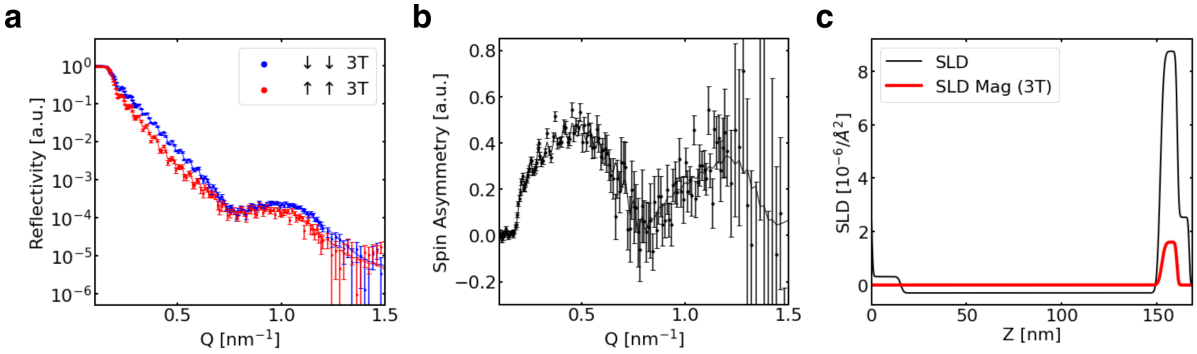

Figure 3.2: **Polarized neutron reflectivity of $PtMn_3$/Py on MgO**. **a**, Non-spin flip reflectivities of MgO/$PtMn_3$(152 nm)/Py(8.9 nm)/TiO_2(6 nm), and **b**, the resulting spin asymmetry. **c**, The extracted magnetic (red) and non-magnetic SLD (black). The magnetic SLD shows a clear lack of any net magnetization in the $PtMn_3$ layer, with only the Py layer showing a non-zero net magnetization as expected. Error bars represent ±1 standard deviation. This data was obtained in collaboration with A.J. Grutter and R.F. Need [55].

3.3 Probing the Magnetic Order Through the Anomalous Hall Effect

Though the magnetic order of the $PtMn_3$ films on $SrTiO_3$ was not directly measurable with neutron diffraction, it is possible to indirectly probe it through electronic measurement as antiferromagnets with the appropriate symmetry can also host an intrinsic AHE (as discussed in chapter 1). Presumably, as the $PtMn_3$ goes through different magnetic transitions, the intrinsic AHE should behave as an order parameter and go through a Néel and first-order transition if both bulk antiferromagnetic phases are present. Electronic measurements of $PtMn_3$, Py, and $PtMn_3$/Py films were performed

on Hall devices with 10 μm x 40 μm channels for all longitudinal and Hall resistivity measurements in this work. Thin film samples were patterned using conventional UV photolithography processes at the University of Michigan Lurie Nanofabrication Facility. Designs were written on 4" fused silica mask plates using a Heidelberg DWL-2000 mask maker with a 4 mm write head. The photolithography for the ion milling and deposition patterns was done using a conventional SPR 220 based process. All samples were ion milled using an Intivac Nanoquest II Ar ion mill at the lowest beam setting of 200V/165 mA (the resulting plasma power density is approximately 0.7 W cm^{-2}), a working temperature of 15 °C and an incident beam angle of 15°. After all ion milling, the backplane of the sample is measured for electrical conductivity with 5-10 μm probe tips placed 20-50 μm apart at assorted points on the sample. This ensures that there is no remnant $PtMn_3$ backplane shunting current, or that the substrate was made conductive through defect or vacancy formation from ion bombardment. The metal contact layers, either Ti(10 nm)/Pt(100 nm) or Cr(10 nm)/Pt(100 nm), were deposited onto a contact deposition lithography mask via pulsed laser deposition or thermal evaporation within a standard metal lift-off process (for cryogenic measurements, Cr seems to behave better as a wetting layer and is suggested over Ti, if available).

The general electronic measurement scheme and coordinate system for patterned Hall devices is shown in Figure 3.3a. The temperature dependent Hall resistance R_{xy} was measured from 120-400 K in a Quantum Design Dynacool PPMS using a standard ETO puck. Zero field R_{xy} versus temperature of $SrTiO_3$/$PtMn_3$(95 nm) films is shown in Figure 3.3b. There is a clear intermediate phase between 150-200 K where the films have significant remnant magnetization in the out-of-plane direction that does not saturate for maximum fields up to 9 T (see Figure C.1). As shown in Figure 3.3, an increase in the zero-field Hall resistance emerges smoothly below T_N and undergoes a first-order transition between 200-300 K, after which it diminishes. The temperature difference between the first-order and Néel transition is ∼150 K, and the overall profile matches that of the neutron diffraction intensity of the half-order $\left(10\frac{1}{2}\right)$ peaks in prior studies of bulk $PtMn_3$ with stoichiometry that closely matches that of the $PtMn_3$ films on $SrTiO_3$ [39], as per the XPS and unpolarized neutron reflectometry measurements discussed in chapter 2. These peaks correspond well to the emergence of an intermediate collinear AFM state, which has a magnetic lattice symmetry between the high temperature non-magnetic metal and the low temperature non-collinear AFM. With respect to the bulk material, the transition temperatures in the $SrTiO_3$/$PtMn_3$ samples are shifted downwards 50-100 K, which is attributed to a combination of tetragonal strain from the substrate lattice mismatch (c/a ∼ 0.98 at 300 K) and reduced Mn stoichiometry. Despite the inability to probe the phases directly with neutron diffraction, AHE measurements have shown that the $PtMn_3$ films on $SrTiO_3$ plausibly have both of the bulk antiferromagnetic phases. As the Néel and first-order transition are now electronically accessible, the spin Hall conductivity can be evaluated in each explicit regime and its structure can be directly linked to the antiferromagnetic order.

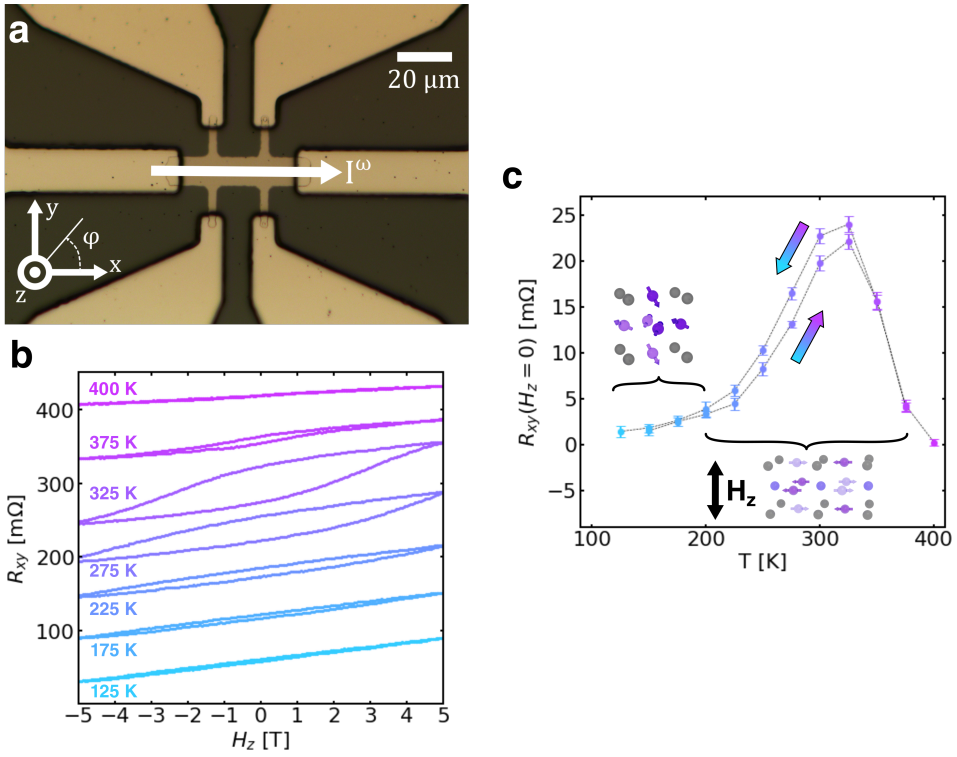

Figure 3.3: **Collinear to non-collinear AFM transition in L1$_2$ ordered PtMn$_3$ thin films**. **a**, Schematic of longitudinal and transverse measurement coordinates for patterned PtMn$_3$ and PtMn$_3$/Py Hall devices. **b**, Anomalous Hall resistance of SrTiO$_3$/PtMn$_3$(95 nm) versus out-of-plane field H_z and temperature T (offset for clarity). **c**, Remnant zero-field anomalous Hall resistance from 5 T training field versus temperature of SrTiO$_3$/PtMn$_3$(95 nm). The intermediate state of large $R_{xy}(H_z = 0)$ corresponds well to a high susceptibility state with remnant ferromagnetic canting in the out-of-plane direction from field cooling (inset). The observed first order transition between 250 K - 300 K is consistent with bulk PtMn$_3$, but shifted lower in temperature by 50 K - 100 K.

CHAPTER 4

Harmonic Hall Effect Measurement of Spin Transfer Torques in $PtMn_3$/Py Heterostructures

4.1 Theoretical Description of Spin Torque Measurement via the Harmonic Hall Effect

The intrinsic spin Hall conductivity in $PtMn_3$ can be probed through its effect on an adjacent ferromagnetic thin film via the anomalous and planar Hall resistances. Specifically, effective magnetic fields from the spin current diffusion into the ferromagnet are measured through the harmonic Hall effect, whereby a harmonic current is applied to the bilayer that induces deflections in the ferromagnet layer which are encoded in the second harmonic transverse magnetoresistance [62–64]. To link the electronic measurement with the effect of the injected spin currents on the ferromagnet magnetization $\boldsymbol{m} = M_S\hat{m}$, it is necessary to understand its dynamics. When a spin current with polarization $\hat{p}$ is injected into a saturated ferromagnet with some orientation $\hat{m}$, the macroscopic dynamics are described by the Landau-Lifshitz-Gilbert-Slonczewski (LLGS) equation [65–67]:

$$\dot{\hat{m}} = -\gamma\hat{m} \times \boldsymbol{H}_{eff} + \alpha\hat{m} \times \dot{\hat{m}} + \gamma H_{\parallel}\hat{m} \times \hat{p} \times \hat{m} + \gamma H_{\perp}\hat{p} \times \hat{m} \tag{4.1.1}$$

where H_{eff} encapsulates crystal and shape anisotropy fields, as well as any external fields H_{ext}, and $H_{\parallel}$ and $H_{\perp}$ are the damping-like and field-like spin torque effective fields, respectively. For a thorough review of spin transfer torque physics and the nuances of spin current diffusion across magnetic interfaces see Ref. [68]. In general, solving Equation 4.1.1 requires a micromagnetic computation model, but there are two analytical limits where the dynamics of $\hat{m}$ can take nice periodic forms and are readily useful in physical experiments. The first limit is near the ferromagnetic resonance frequency, and is employed in spin-torque ferromagnetic resonance (STFMR) experiments with driving currents in the 1-10 GHz range [10, 11]. This technique is popular, but

requires tightly constrained electrical signal pathways and device geometries to ensure delivery of the expected RF power to the device. The other limit, is the quasistatic limit for low enough frequencies where the precession is minimal and the equilibrium orientation of $\hat{m}$ tracks with the applied current (this is well satisfied in the low kHz range used here). In this regime, $\dot{\hat{m}} \sim 0$ and the magnetization lines up with the total effective field:

$$\hat{m} \parallel \boldsymbol{H}_{eff} + H_{\parallel}\hat{m} \times \hat{p} = \boldsymbol{H}_A + \boldsymbol{H}_D + \boldsymbol{H}_{ext}(\chi, \phi) + \Delta H(I, \theta, \varphi) \tag{4.1.2}$$

where $\boldsymbol{H}_A$ is the crystal anisotropy field, $\boldsymbol{H}_D$ is the demagnetization field from thin film shape anisotropy, $\boldsymbol{H}_{ext}$ is the applied external field, and ΔH contains contributions from spin current torques and the Oersted field from film layers or interfaces adjacent to the ferromagnet layer. In general, there is a complex relationship between the applied field coordinates (χ, ϕ) from the magnetization coordinates (θ, φ) which depends on the external field magnitude and orientation with respect to the equilibrium effective fields and their anisotropy. For example, in a canonical SHE material such as Pt, W with only nonzero σ^y_{xz}, when a current is applied in the $\hat{x}$, direction, the out-of-plane spin current polarization is $\hat{p} = -\hat{y}$ [9–12]. The resulting effective field $\Delta\boldsymbol{H}$ is:

$$\begin{aligned} \Delta\boldsymbol{H} &= (H_{FL} - H_{Oe})\,\hat{y} + H_{DL}\hat{m} \times \hat{y} \\ &= -H_{DL}\cos\theta\hat{x} + (H_{FL} - H_{Oe})\,\hat{y} + H_{DL}\sin\theta\cos\varphi\hat{z} \end{aligned} \tag{4.1.3}$$

Here, the notation $H_{\parallel} = H_{DL}$ and $H_{\perp} = H_{FL} - H_{Oe}$ is adopted to separate the damping-like and field-like contributions from spin transfer torques (H_{DL}, H_{FL}) from that of the Oersted field from an applied total current in adjacent film layers or interfaces (H_{Oe}). In this work, ferromagnetic films and external field amplitudes are chosen so that the ferromagnetic layer is always saturated, and these are taken to be the same. If the ferromagnet $\hat{m}$ in the quasistatic regime has a well defined equilibrum notation and the deflections from $\Delta\boldsymbol{H}$ are perturbative, the magnetization deflection is linear in $|\Delta\boldsymbol{H}|$ and the spin torque effective fields can be exactly quantified.

Given the link between incident spin currents with polarization $\hat{p}$, and the deflection of the magnetization $\hat{m}$, if the deflection can be measured precisely then the spin torque effective fields H_{DL}, H_{FL} can be extracted. This deflection is usually measured with optical methods, such as polarized X-ray reflectivity [69] and the magneto-optical Kerr effect [70, 71], or electronically through the effect of the deflection on the magnetoresistance. In this work, the quasistatic LLGS behavior is measured through the anomalous and planar Hall resistance:

$$R_{xy}(\theta, \varphi) = R_A\cos\theta + R_P\sin^2\theta\sin 2\varphi \tag{4.1.4}$$

where the magnetization orientation is $\hat{m} = \cos\varphi\cos\theta\hat{x} + \sin\varphi\sin\theta\hat{y} + \cos\theta\hat{z}$, with $\hat{z} \parallel [001]$ for all thin film samples in this work. When a current is applied to the heterostructure, the spin currents generated in the $PtMn_3$ layer diffuse upwards into the Py and deflect the magnetization away from its equilibrium orientation by some small $\Delta\theta, \Delta\varphi$. The tilting of the magnetization direction from equilibrium by the perturbative spin torque fields is generally small, and it would be difficult to make a DC Hall measurement and fit for $\Delta\theta, \Delta\varphi$ with a high accuracy. To demodulate this component with a high signal-to-noise ratio, a harmonic current is used instead. Because the spin torque fields are now harmonic, the perturbed magnetization now also harmonic, so there is a mixing effect through the newly harmonic magnetoresistance and the applied current:

$$V(t) = I_a \sin\omega t R_{xy}(\theta + \Delta\theta(\sin\omega t), \varphi + \Delta\varphi(\sin\omega t)) \tag{4.1.5}$$

As a result, DC and second Harmonic signals are generated which encode the perturbative deflection. Of the two, the second Harmonic signal is typically chosen for analysis to avoid other general parasitic DC signals. To first order in $\Delta\theta, \Delta\varphi$, the second harmonic response to the magnetization deflection is:

$$V_{xy}^{2\omega} \propto \nabla_{\varphi,\theta} V_{xy}|_{H_{ext},I,\varphi_0,\theta_0} \cdot (\Delta\varphi(H, I, \varphi_0, \theta_0), \Delta\theta(H, I, \varphi_0, \theta_0)) \tag{4.1.6}$$

A general schematic for this measurement is shown in Figure 4.1a, where typically a single lock-in amplifier supplies the longitudinal harmonic drive current with frequency ω, and demodulates the Hall voltage with frequency $n\omega,\ n \in \mathbb{N}$.

The second harmonic response described by Equation 4.1.6 is generally complex, and to derive an analytic form requires choosing ferromagnet layers with well behaved anisotropy and a favorable path in φ, θ (though it has been caclculated with a recursive micromagnetic simulation for semi-arbitrary external field orientations [64]). Thin film metallic ferromagnets such as Py that are dominated by shape anisotropy are particularly convenient for second harmonic Hall effect measurements. With an applied out-of-plane external field ($\boldsymbol{H}_{ext} \parallel \hat{z}$), the magnetization is linear up to the saturation field H_S, and for an in-plane external field ($\boldsymbol{H}_{ext} \perp \hat{z}$), the magnetization follows the field exactly if the (weak) crystalline and shape aniosotropy is overcome [72]. For all in-plane harmonic Hall effect scans in this work, the following condition is satisfied:

$$\hat{m} = \left(H_{ext}\hat{h} + H_a(\hat{m} \times \hat{b})\hat{b}\right)\frac{1}{H_{eff}} \approx \hat{h} \mid H_{ext} >> H_c, H_a \tag{4.1.7}$$

where H_c is the in-plane coercive field from the magnetocrystalline anisotropy, and H_a is the shape anisotropy field for a pattern with a long axis in $\hat{b}$. With ideal uniaxial in-plane anisotropy, and an

external field that saturates the magnetization in-plane, the perturbative deflections to $\hat{m}$ from the spin torque effective fields can be readily defined to leading order in $\Delta\boldsymbol{H}$ [62–64, 73]:

$$\begin{aligned}\Delta\theta &= \frac{\Delta H_\theta}{H_{ext} + H_S + \Delta H_r} \approx \frac{\Delta H_\theta}{H_{ext} + H_S} \\ \Delta\varphi &= \frac{\Delta H_\varphi}{H_{ext} + \Delta H_r} \approx \frac{\Delta H_\varphi}{H_{ext}}\end{aligned} \tag{4.1.8}$$

The experimental setup for such a configuration is shown in Figure 4.1b-c for a canonical spin Hall material which induces in and out-of-plane spin torque effective fields as per Equation 4.1.3 for $\theta_0 = \pi/2$. The physical conditions for Equation 4.1.8 are well justified in this work by the out-of-plane AHE scans in Figure C.2, and with the in-plane VSM data in Figure C.3, given that $H_{ext} \geq 250$ Oe for all harmonic Hall effect measurements.

As the film plane in the (001)-oriented $PtMn_3$ is not the high symmetry (111) orientation of the non-collinear AFM state, there is an expected orientation-dependent anisotropy of spin Hall conductivity which can be measured by orienting Hall devices along the [100], [110], [010], and [$\bar{1}$10] crystal axes. The expected anisotropy in each set of devices can be determined from the symmetry transformations of spin Hall conductivity tensors as done previously [33], and projected into the respective Hall devices coordinate system, as shown in Figure 1.3. In general, the σ^i_{xz} components are highly anisotropic with respect to the crystal orientation, and each component has a respective set of orientations where it is expected to dominate. In the most general case, a single global AFM domain will generate some combination of $\hat{p} = \hat{x}, \hat{y}, \hat{z}$ polarized spin current. Assuming some contribution from all possible polarization components, Equation 4.1.4, 4.1.6, and 4.1.8 can be combined to obtain an analytical form for the expected in-plane second harmonic response:

$$\begin{aligned}V^{2\omega}_{xy} &= CR_0I_a^2\cos\varphi \\ &+\frac{1}{2}\frac{R_AI_{FM}J_{SHM}}{H_{ext}+H_S}\left(h^x_{DL}\sin\varphi - h^y_{DL}\cos\varphi + h^z_{FL}\right) \\ &+\frac{R_PI_{FM}J_{SHM}}{H_{ext}}\cos 2\varphi\left(h^x_{FL}\sin\varphi - (h^y_{FL}-h_{Oe})\cos\varphi + h^z_{DL}\right)\end{aligned} \tag{4.1.9}$$

where R_A and R_P are the anomalous and planar Hall resistances, respectively, J_{SHM} is the current density in the spin Hall material, here $PtMn_3$, $H^i_{FL,DL} = J_{SHM}h^i_{FL,DL}$ for $i \in (x, y, z)$ are the effective fields from components of spin current polarization, and the first term, $CR_0I^2_{total}\cos\varphi$ is a separate contribution from the anomalous Nernst effect, which arises from out-of-plane thermal gradients present in every thin film system [63, 74, 75]. For the spin torque effective fields used here, a dependence on current density is used with units of Oe per 10^7 A cm^{-2}(1 Oe = 79.6 A/m),

instead of total film current. Due to the small spin diffusion lengths in metals (1 nm - 10 nm) [76], only the $PtMn_3$ close to the top interface is expected to significantly contribute to $V_{xy}^{2\omega}$. In all harmonic Hall effect measurements in this work, $J_{SHM} < 5{\cdot}10^6$ A cm^{-2} to reduce thermal drift and the baseline thermoelectric contribution. This results in $h_{Oe} < 30$ Oe per 10^7 A cm^{-2} for the $SrTiO_3$/$PtMn_3$(46.6 nm)/Py(6.8 nm) devices.

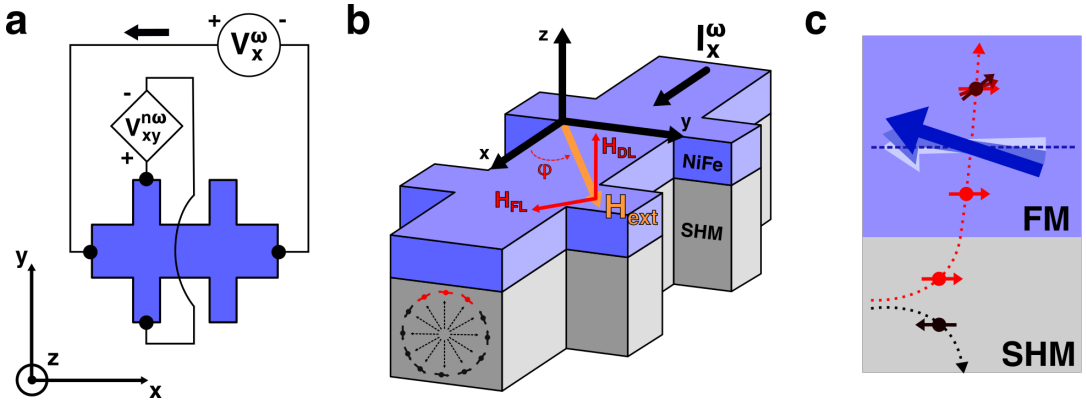

Figure 4.1: **Electrical and coordinate schematic for harmonic Hall effect measurement of spin transfer torques**. **a**, Electrical setup for measuring the harmonic Hall resistance in a ferromagnet (FM) and SHE material (SHM) bilayer Hall device, where a lock-in amplifier applies a longitudinal voltage with frequency ω, and then demodulates the transverse Hall voltage of frequency $n\omega \mid n \in \mathbb{N}$. **b**, The FM layer magnetization is oriented with an external field H_{ext} to measure the resulting field-like H_{FL} and damping-like H_{DL} spin transfer torques from out-of-plane spin current injection from the SHM. **c**, Damping-like "spin-transfer" torque is due to spin current interaction with the magnetic lattice versus the field-like torque from local spin accumulation.

The harmonic Hall effect measurements in this work were done with heterostructures of $SrTiO_3$/$PtMn_3$(46.6 nm)/Py(6.8 nm)/SiC, with the $PtMn_3$ and Py layers deposited with RF magnetron sputtering, as discussed in chapter 2, and SiC deposited *ex situ* as a capping layer to prevent oxidation (see Methods in Ref. [55]). The $PtMn_3$ layer was purposefully grown > 40 nm, to ensure a large $L1_2$ ordering near the surface that is clear of the ~ 20 nm transition region discussed in chapter 2 and 3. It is also necessary to keep the Py layer below 10 nm thickness to minimize any anomalous second harmonic response from out-of-plane spin texture formation due to interfacial exchange and shape anisotropy [77]. To quantify the current distribution in bilayer $PtMn_3$/Py devices, 4-wire resistivity measurements were performed on isolated films and a parallel resistor model was used to estimate the current splitting. The ratio of total longitudinal current in each film in the $SrTiO_3$/$PtMn_3$(46.6 nm)/Py(6.8 nm)/SiC heterostructures is calculated by using measured resistivities from isolated films (see Figure D.2a) and combining them in a parallel resistor model. Using the calculated resistances for the individual film channels, the ratio of total current in each channel can be estimated, as shown in Figure D.2b. The total resistance of the 46 nm $PtMn_3$

and 6.8 nm Py layers in the Hall channel is calculated and combined in parallel to estimate the 2-wire resistance of the Hall device, as shown in Figure D.2c, and the calculations are in are in excellent agreement with the explicit two wire measurements of the patterned $SrTiO_3$/$PtMn_3$(46.6 nm)/Py(6.8 nm)/SiC devices (this is also good evidence that the $SrTiO_3$ backplane is not significantly conducting across the full temperature range). The respective current ratios are used to calculate I_{FM}, J_{SHM} at each temperature for the in-plane second harmonic model in Equation 4.1.9, and are accounted for in the current-normalized effective fields $h^i_{DL,FL}$ in units of Oe per 10^7 A cm^{-2}.

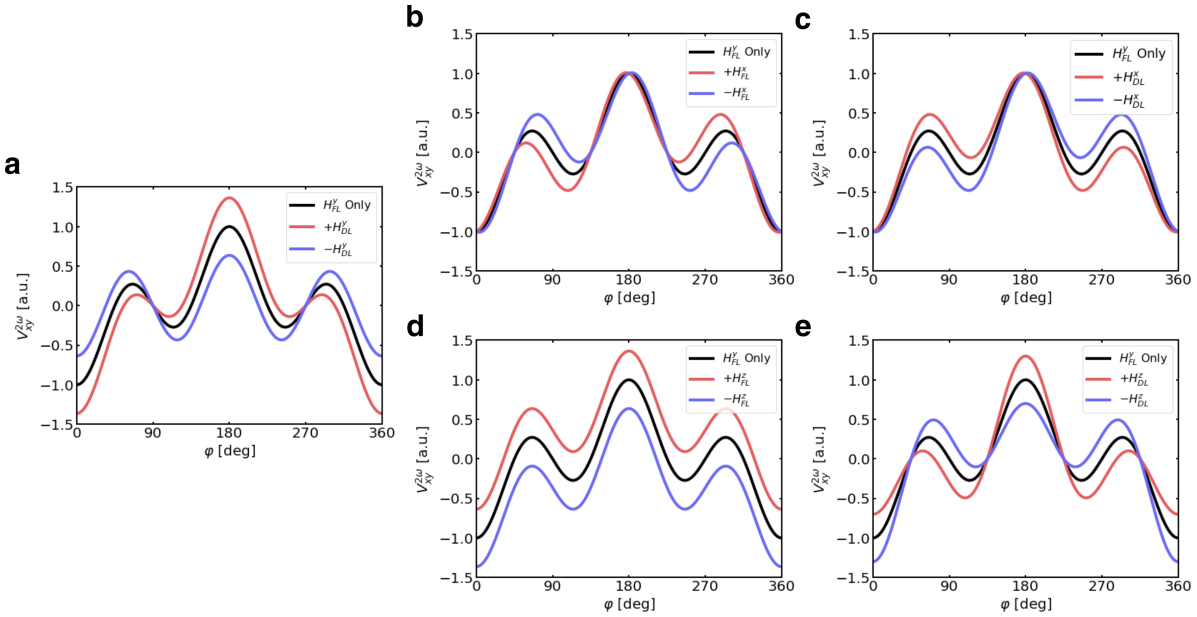

Figure 4.2: **Second harmonic dependence on spin torque effective fields from $\hat{x}, \hat{y}, \hat{z}$ polarized spin currents**. **a**, Typical $V^{2\omega}_{xy}(\varphi)$ profile for only H^y_{FL} (black, in all subfigures) from SOT or ASOT, and effect of $\pm H^y_{DL}$ (red/blue) from some σ^y_{xz}. **b**, Effect of $\pm H^x_{FL}$ (φ asymmetry around 180°), and **c**, $\pm H^x_{DL}$ (opposite φ asymmetry around 180°). **d**, Effect of $\pm H^z_{FL}$ (voltage asymmetry), and **e**, $\pm H^z_{DL}$ (voltage shift). Except for $H^x_{(DL,FL)}$, which could be easily confused if not fit for precisely, any $\hat{p} = \hat{y}, \hat{z}$ spin currents of significant amplitude injected into the Py layer should be visibly apparent based on their distinct effects on $V^{2\omega}_{xy}$.

As the individual spin torque effective fields have different symmetry and field dependence, the presence of the distinct components of Equation 4.1.9 can be visually identified in the $V^{2\omega}_{xy}$ data if they are of sufficient magnitude. To provide a useful visual reference, the addition of positive/negative components of these fields to a basic response from a $\hat{p} = \hat{y}$ or Oersted-like field is plotted in Figure 4.2. Of the six components, all but the $H^x_{FL,DL}$ are uniquely identifiable due to a distinct effect on the harmonic profile (satellite peak amplitude change, vertical shift, vertical asymmetry). If high precision measurements of $H^x_{FL,DL}$ are desired, then this geometry may not

be optimal due to the similarity of the perturbative effect from the field and damping-like torques, as shown in Figure 4.2b-c.

4.2 Extraction of Spin Torque Effective Fields in $PtMn_3$/Py with the Harmonic Hall Effect

If the ferromagnet in a spin Hall material/ferromagnet bilayer has ideal uniaxial in-plane anisotropy it is possible to extract all necessary physical parameters to extract the spin torque effective field components $h^i_{FL,DL}$ from Equation 4.1.9 at particular temperature with just two measurements: an out-of-plane field sweep to extract the anomalous Hall resistance, and an in-plane first and second harmonic scan versus φ, H_{ext} to extract the planar Hall resistance and the field-scaling of the second harmonic Hall signal. Luckily, for metallic ferromagnets such as Py, the shape anisotropy is dominant, and the ideal in-plane anisotropy is always realized in the thin film limit. Out-of-plane magnetization versus field for isolated Py films and $PtMn_3$/Py bilayers is shown in Figure C.2, confirming the expected anisotropy. For all samples in this study, electronic measurements in the range of 20-400 K were performed in a Quantum Design Dynacool PPMS with the standard ETO puck, the horizontal rotator accessory option, and a custom breakout box for electronic instruments. For harmonic Hall effect measurements, first and second harmonic components were demodulated simultaneously using an Ametek DSP 7265 lock-in amplifier running in dual harmonic mode at a source frequency of 1937 or 2377 Hz for temperatures between 120-400 K. Samples were thermalized at each temperature setpoint for 0.5-1.0 h with the standard ETO puck and up to 1.5 hours with the horizontal rotator. Longitudinal and Hall resistances of patterned Hall devices were obtained via DC 4-wire measurements with a Keithley 2450 sourcemeter.

Ensuring that there are no significant interfacial exchange effects on the Py magnetization is crucial, as inadvertently training a large interfacial spin glass layer and changing the effective ferromagnet thickness, anisotropy, or M_S would make it difficult to quantify the spin torque effective fields, and claim that they originate from intrinsic spin Hall conductivity in the $PtMn_3$ layer. Anomalous Hall effect measurements of $PtMn_3$/Py films show identical M_S versus temperature behavior as isolated Py films (see Figure C.2). Further, vibrating sample magnetometry of the same sample used for harmonic Hall effect measurements establishes that there is no significant exchange bias in the down to 120 K, the minimum temperature used in the study, as shown in Figure C.3.

If the ferromagnetic layer has the ideal uniaxial in-plane magnetization, then the anomalous Hall resistance term for Equation 4.1.9 can be extracted with an out-of-plane field scan of the first

harmonic Hall voltage:

$$V_{xy}^{\omega} = I_{total}^{\omega} R_0 + I_{FM}^{\omega} \left(R_H H_z + R_A \begin{cases} 1 & H_z \geq H_S \\ \frac{H_z}{H_S} & H_z \leq H_S \end{cases} \right) \tag{4.2.1}$$

where R_0 is the base resistance, R_H is the classical Hall resistance based on carrier density, carrier mobility, and external field strength, and R_A is the anomalous Hall resistance. Ideally, $R_0 = 0$, but there is usually a small parasitic longitudinal resistance due to contact pattern misalignment or Hall bar pattern defects. Conveniently, R_P is extracted in tandem with the in-plane $V_{xy}^{2\omega}$ ($\theta_0 = \pi/2$) by running the lock-in amplifiers in dual harmonic mode:

$$V_{xy}^{\omega} = R_P I_{FM}^{\omega} \sin 2\varphi + I_{total}^{\omega} R_0 \tag{4.2.2}$$

With data for Equation 4.1.9, 4.2.1, and 4.2.2, as well as the current splitting between $PtMn_3$ and Py, the spin torque effective fields $h_{FL,DL}^{i}$ for each σ_{xz}^{i} component can be extracted precisely.

The extracted spin torque effective fields $h_{FL,DL}^{i}$ detected in the Py layer are a direct measure of spin current generated by the $PtMn_3$. The field-like h_{FL}^{i} is simply a measure of local spin accumulation, as the spin current acts on the magnetization just like an external field would. The damping-like h_{DL}^{i} are typically used as a performance metric in SHE/FM bilayers, as they are taken to be a measure of out-of-plane spin current diffusion through the ferromagnet interface [9, 10, 68]. With a measured h_{DL}^{i}, the out-of-plane spin current with polarization $\hat{p} = \hat{i}$ is taken to be:

$$J_S^i = \left(\frac{2e}{\hbar} \right) M_s t_{FM} J_{SHM} h_{DL}^{i} \tag{4.2.3}$$

The final figure of merit is usually the efficiency of generating this spin current $\xi_{STT}^{i} = J_S^i / J_{SHM}$, which is expressed here in units common to this work:

$$\xi_{STT}^{i} = 3.039 \cdot 10^{-6} \left[\frac{\text{A} \cdot \text{cm}}{\text{emu} \cdot \text{Oe} \cdot \text{nm}} \right] \cdot M_S \left[\frac{\text{emu}}{\text{cm}^3} \right] \cdot t_{FM} \, [\text{nm}] \cdot h_{DL}^{i} \left[\frac{\text{Oe}}{10^7 \frac{\text{A}}{cm^2}} \right] \tag{4.2.4}$$

As a standalone fun fact, a convenient relation can be found here if the Py layer is exactly 4.17 nm thick (4-6 nm is a fairly common thickness) and $M_S \sim 800$ emu cm^{-3} (the bulk value, with $H_S \sim$ 1.0 T [78]), then $\xi_{STT} \approx 0.01 h_{DL}$ when h_{DL} is in units of Oe per 10^7 A cm^{-2}. In prior literature, it is common for ξ_{STT}^{i} to also be referred to as the spin Hall angle (θ_{SH} or θ_{SHA}), taken to be the intrinsic generation efficiency of the spin Hall material. The contemporary understanding is that it is difficult to obtain the true intrinsic efficiency due to complicated scattering of spin current from different bilayer interfaces with varying quality and material types, a concept referred to as

"interface transparency" [79]. The two parameters are related, with $\xi^i_{STT} = \eta\theta^i_{SHA}$, where $\eta \leq 1$ takes the interface transparency into account.

4.3 Effects of Antiferromagnetic Domain Degeneracy on Intrinsic Spin Hall Conductivity in the Non-collinear $PtMn_3$ State

As outlined in the chapter 1 discussion around Figure 1.3, the anisotropy of the intrinsic spin Hall conductivity of $PtMn_3$ can theoretically be used for orientation-dependent selectivity of a dominant σ^i_{xz} component. In addition to current orientation, it is critical to consider the size and orientation of antiferromagnetic domains. Below the first-order transition, the Kagome planes of the low-temperature $PtMn_3$ phase could be oriented in any [111] equivalent direction. If a Hall device is rotated 90 degrees in-plane with respect to the crystal lattice, but the AFM lattice is also rotated accordingly, then there is no change to the system from re-orienting the device, as outlined in Figure 4.3c. In general, field-training non-collinear antiferromagnetic domains is not a well-defined practice, and so multiple devices of the same crystal orientation are sampled instead. Additionally, the size of AFM domains in thin films can range from 10s of nm to several μm [80–82], and it is plausible that 10 μm wide Hall devices can contain multiple domains. In general, multiple AFM domains in equivalent proportion serve to reduce the orientation dependent anisotropy of the σ^i_{xz}, and in the case of having all possible domains equally present, quenches them entirely (see section A and the discussion around Figure A.1). Despite the difficulties in orienting the non-collinear AFM lattice, second harmonic Hall effect data is observed which yields a clear contribution from $+\sigma^x_{xz}$, σ^y_{xz}, $-\sigma^x_{xz}$, and σ^z_{xz}, respectively, in Figure A.1d-g. These profiles emerge at temperatures below 200 K, below the observed first-order transition in the zero-field AHE data in Figure 3.3, and suggest that these devices are mostly a single AFM domain. Whenever there is a dominant σ^i_{xz} component, it is possible to visually identify it from the second harmonic data due to the unique symmetry in φ for each spin torque effective field contribution to $R^{2\omega}_{xy}$, as per the expected profiles in Figure 4.2.

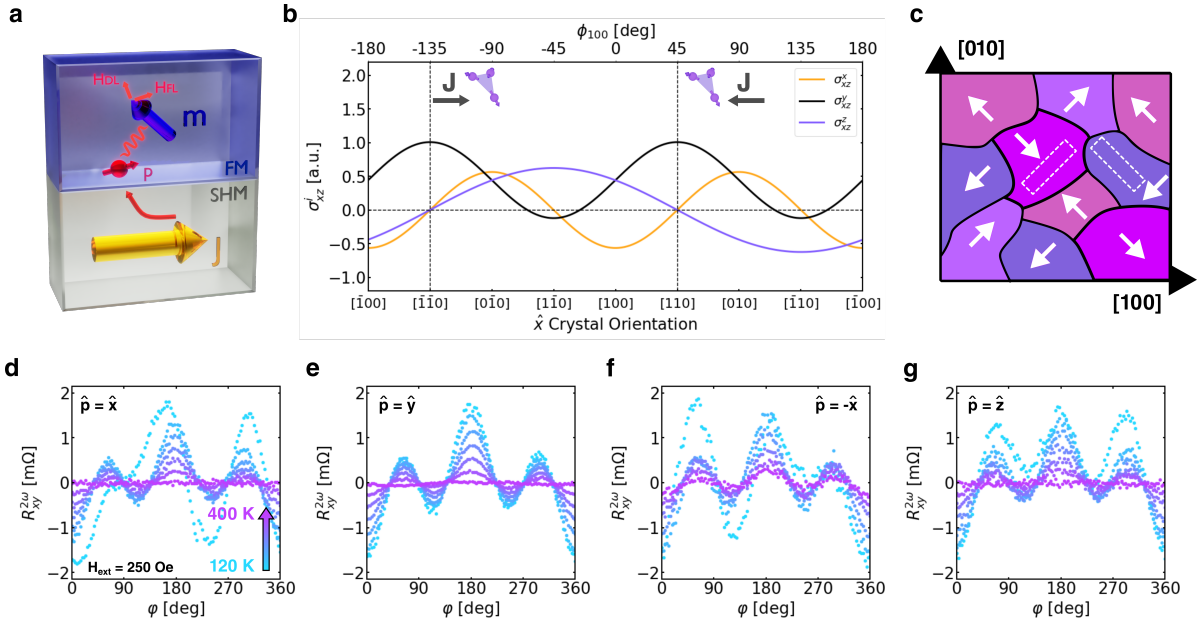

Figure 4.3: **Current and domain orientation versus spin torque components in $PtMn_3$/Py**. **a**, Simplified schematic of out-of-plane spin current from σ^i_{xz}, $i = (x, y, z)$ generated in the AFM spin Hall material with net polarization $\hat{p}$ diffusing into a ferromagnetic layer and causing field-like and damping-like spin torques. **b**, Current orientation dependence of σ^i_{xz} for a $PtMn_3$ thin film with a single (111)-oriented antiferromagnetic domain, and with a Hall device $\hat{x}$ oriented at an in-plane angle ϕ_{100} from the [100] crystal direction using $\underline{\sigma}^i$ from Ref. [33] and transforming into the device coordinates. **c**, Schematic of possible non-collinear AFM domain orientation in (001) plane (white arrows are in-plane [111] projections), and degeneracy with two Hall bars oriented orthogonally to the crystal lattice but with identical magnetic lattices. Second harmonic sweeps at H_{ext} = 250 Oe for temperatures between 120 K - 400 K for devices with dominant **d**, $+\sigma^x_{xz}$, **e**, σ^z_{xz}, **f**, σ^y_{xz} and **g**, $-\sigma^x_{xz}$ which emerge below 200 K. Aligning devices to a preferred AFM texture orientation is difficult due to the AFM domain degeneracy highlighted in **c**, though it is possible to find devices with a dominant $\hat{p} = \hat{x}, \hat{y}, \hat{z}$ component.

4.4 Spin Torque Effective Fields versus Temperature and Antiferromagnetic Phase of $PtMn_3$

When fitting Equation 4.1.9 to temperature dependent in-plane second harmonic Hall effect data, a fitting procedure must be used which includes parameter correlation and error analysis. The specific forms for each $h^i_{FL,DL}$ contribution for Equation 4.1.9 have a unique symmetry, but form a set of sinusoidal functions on the $\varphi \in [0, 2\pi]$ domain which almost mirrors a Fourier basis but with only six of the first few components. For particular measurements, such as those with large σ^x_{xz} components, it may be difficult to find a good fit with common methods, as per the discus-

sion around Figure 4.2. The fitting method of choice here is the Differential Evolution Adaptive Metropolis (DREAM) algorithm [59] as implemented in the Bumps python package (v0.8.0) [60], which loads the best parameter fits from a differential evolution burn-in run and performs Markov chain Monte Carlo sampling of the parameter space as weighted by the χ^2 error. Example fitting scripts for second harmonic Hall effect data used in this work are included in section E. Fitting with DREAM was performed for all datasets corresponding to Equation 4.1.9, 4.2.1, and 4.2.2. An example of a good fit is shown in Figure E.1 for the free parameter fit shown in Figure 4.4a-h, where the parameters have a well defined distribution that is not artificially constrained by their bounds, and the relative error is small.

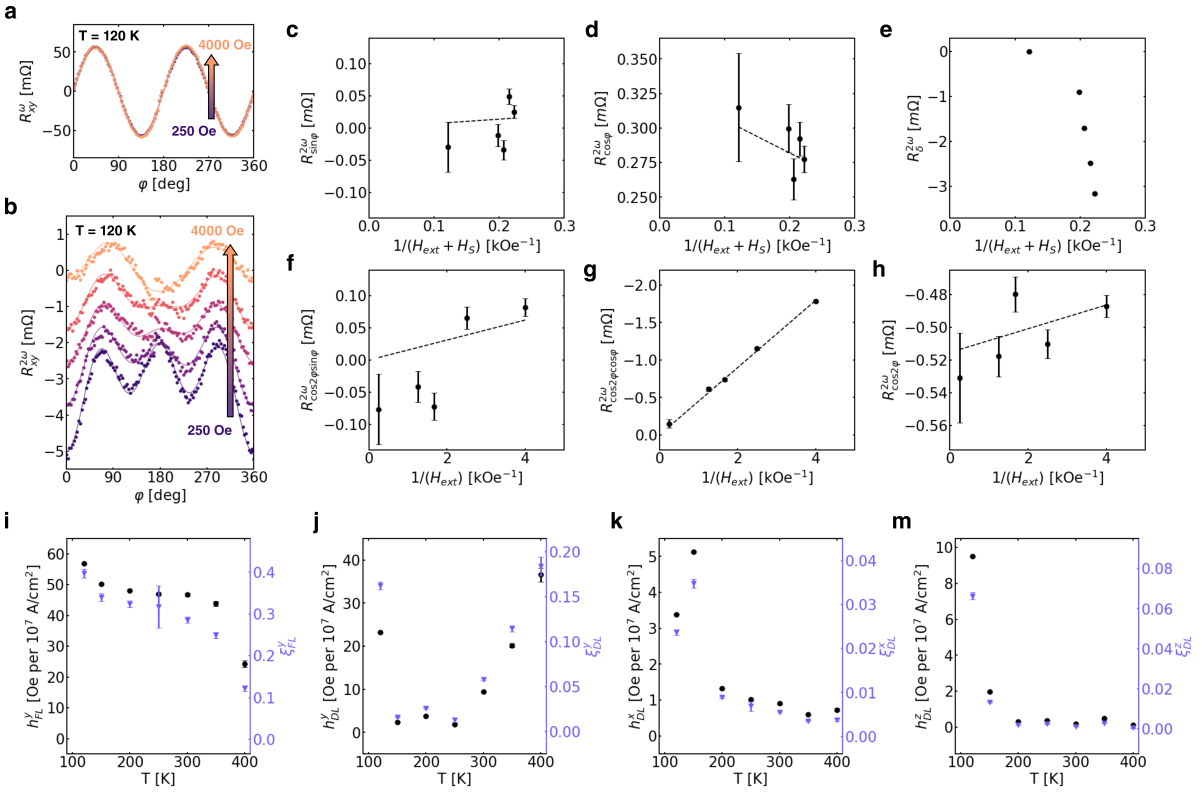

Figure 4.4: **Second harmonic Hall effect and spin torque effective fields versus temperature in $PtMn_3$/Py Hall devices**. Representative φ, H_{ext} scans of **a**, first and **b**, second harmonic Hall resistance of a $PtMn_3$(46.6 nm)/Py(6.8 nm) device with prominent σ^z_{xz}. **c**-**h**, A breakdown of components by symmetry as a function of $1/H_{ext}$ and $1/(H_{ext}+H_S)$. All components follow the expected field relations well except for the vertical offset (h^z_{FL}) component, which is much larger and nonlinear in $1/(H_{ext}+H_S)$. For the same device, the resulting **i**, field-like (h^y_{FL}) and **j**, damping-like (h^y_{DL}) spin torque effective fields and efficiencies from σ^y_{xz} vs. temperature, and damping-like spin torque effective fields (black circles) and efficiencies ξ (purple triangles) from **k**, σ^x_{xz} (h^x_{DL}) and **m**, σ^z_{xz} ($h_D L^z$) vs. temperature. The torques from the $\hat{x}, \hat{z}$ polarized spin currents are only significant below 200 K - 250 K, commensurate with the emergence of the noncollinear $PtMn_3$ AFM phase.

The field and in-plane angle dependence of a representative first and second harmonic scan is shown in Figure 4.4a-b for a $SrTiO_3$/$PtMn_3$(46.6 nm)/Py(6.8 nm)/SiC Hall device oriented in a (100)-equivalent direction at 120 K. The first harmonic profile does not change significantly with H_{ext} and follows the expected $\sin 2\varphi$ profile with no change in amplitude, which indicates good saturation of the Py layer for all H_{ext}, and good thermalization. The corresponding second harmonic profiles are drastically different from the typical spin Hall effect result, which only has $\cos 2\varphi \cos \varphi$ and $\cos \varphi$ components. Here, the dominant spin conductivity is σ_{xz}^{z} and there is a strong field-dependent $\cos 2\varphi$ and vertical offset instead. The dependence of each separate $R_{xy}^{2\omega}$ component versus $1/H_{ext}$ (for in-plane deflections) and $1/(H_{ext} + H_S)$ (for out-of-plane deflections) is shown in Figure 4.4c-h for the same device at 120 K, and the extracted spin torque effective fields and corresponding spin transfer torque efficiencies ξ_{STT}^{i} are shown in Figure 4.4i-m over the full temperature range of 120-400 K. The components corresponding to fields from $\hat{x}, \hat{y}$ polarized spin currents, when significant, follow the expected field relations well. The field like component for the $\hat{z}$ polarized current is expected to be a field-dependent offset that goes like $1/(H_{ext} + H_S)$, but seems to scale inversely with field and does not have the expected linear behavior (Figure 4.4e). For devices with field-dependent offsets and $\cos 2\varphi$ components, h_{FL}^{z} can be extracted by fitting a slope to the coefficients shown in Figure 4.4e (ignoring the fact that the that the inverse field scaling is nonlinear), but this yields $\sim$1000 Oe per 10^7 A cm^{-2}, which is quite unlikely due to the relatively smaller h_{FL}^{y} ($<$ 100 Oe per 10^7 A cm^{-2} for all devices).

Though the exact origin of the anomalous scaling of the h_{FL}^{z} components in the high σ_{xz}^{z} samples remains undetermined, $R_{xy}^{2\omega}$ may be complicated by either an additional thermoelectric contribution from any anomalous spin textures near the interface, or by a spin polarization of the charge current from field-induced canting of the $PtMn_3$. From the VSM data in Figure C.3, there is no evidence for an anomalous ferromagnetic component e.g. from a spin glass layer formed by exchange interaction with the $PtMn_3$. Further, any effective fields from injected spin current would still be expected to follow $1/H_{ext}$, $1/(H_{ext} + H_S)$ field dependencies. Additionally, the Py layer seems to be a well behaved uniaxial in-plane ferromagnet with no significant exchange bias in the antiferromagnetic $PtMn_3$ phases (Figure C.3). There is also a general over-fitting concern with the $h_{DL,FL}^{x}$ components due to their near identical but opposite polarity contributions to $R_{xy}^{2\omega}$ as per Figure 4.2b-c. It is likely that some amplitude is exchanged between the two components during the fitting procedure, and that this is responsible for the low-temperature discrepancy between the $h_{DL,FL}^{x}$ amplitudes shown in Figure 4.5. In general, the interactions across a ferromagnet-antiferromagnet interface may complicate the established second harmonic Hall effect model described by Equation 4.1.9, due to interfacial transport phenomena being sensitive to small volumes of anomalous spin texture across the interface. In all cases but the h_{FL}^{z} field-dependent offset, effective fields can be reasonably be extracted from the in-plane second harmonic data across the

full temperature range.

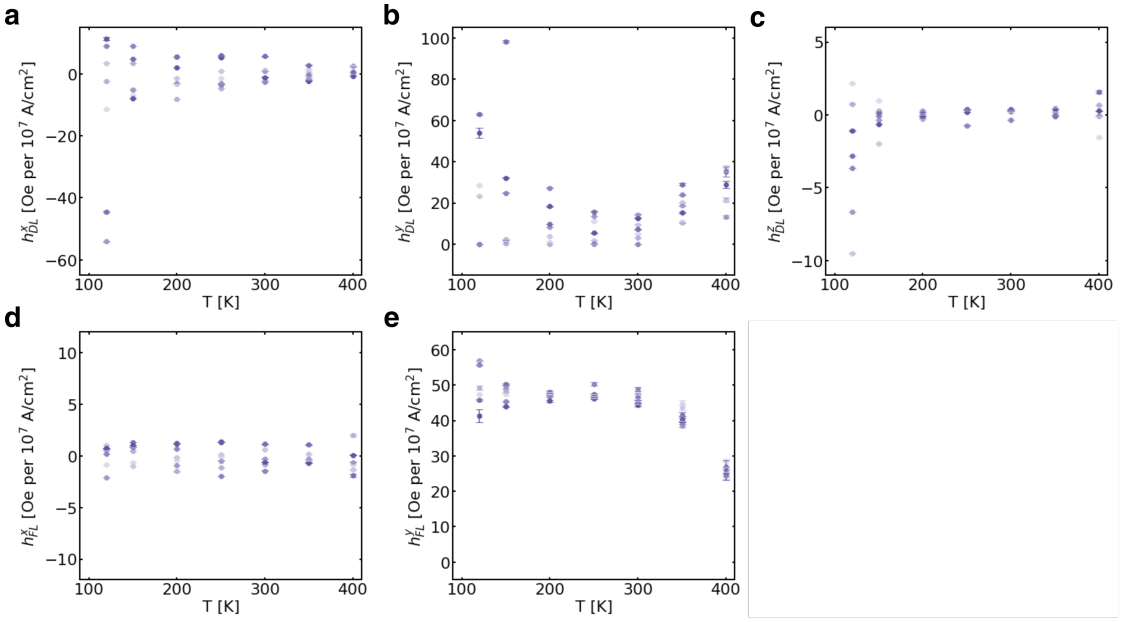

Figure 4.5: **Spin torque effective field components in $PtMn_3$/Py vs. Temperature**. Extracted spin torque effective fields from the in-plane second harmonic Hall effect measurements of the $SrTiO_3$/$PtMn_3$(46.6 nm)/Py(6.8 nm)/SiC devices for damping-like torques from **a**, $\hat{x}$, **b**, $\hat{y}$, and **c**, $\hat{z}$ out-of-plane spin currents, and for the field-like torques from **d**, $\hat{x}$, and e, $\hat{y}$ out-of-plane spin currents. In general, the devices exhibit a typical spin Hall effect-like σ_{xz}^{y} that follows the Néel transition and has an amplitude exceeding typical Pt/Py devices by a factor of ∼3. Components relating to σ_{xz}^{x}, σ_{xz}^{z} arise below the first-order transition at 200 K - 250 K, and the σ_{xz}^{y} diverges as well, which can be attributed to the anisotropic spin Hall conductivity expected in the non-collinear AFM phase.

The field-like and damping-like spin torque effective fields are shown for all devices in this study as a function of temperature are shown in Figure 4.5. As with the fields from the (100)-equivalent device, shown in Figure 4.4i-m, the effective fields from the spin Hall conductivities σ_{xz}^{x} and σ_{xz}^{z} emerge suddenly below 200-250 K and are near zero at higher temperatures, corresponding well to the phase transitions seen in the anomalous Hall conductivity profile in Figure 3.3. At 120 K, devices with significant σ_{xz}^{z} yield h_{DL}^{z} = 8.07 ± 1.43 Oe per 10^7 A cm^{-2}, and devices with significant σ_{xz}^{x} contributions yield h_{DL}^{x} = 26 ± 19 Oe per 10^7 A cm^{-2}. In the large σ_{xz}^{x} and σ_{xz}^{z} devices at 120 K, σ_{STT}^{z} = 0.056 ± 0.009 and ξ_{STT}^{x} = 0.18 ± 0.13. These values are comparable to typical ξ_{STT}^{y} reported for intrinsic SHE in single heavy element thin films [9, 76, 83] despite the 75% reduction in Pt content, and are attributed to the stronger itinerant exchange physics from the antiferromagnetic order. Unlike the corresponding $\hat{p} = \hat{x}, \hat{z}$ components, h_{FL}^{y} follows the profile of a typical Néel transition, rising monotonically below 400 K, though there is a slight bifurcation between devices below 200 K which is attributed to the onset of the intrinsic and

orientation-dependent σ^{y}_{xz} from the non-collinear state, the polarity of which can vary with AFM lattice orientation. The baseline level of h^{y}_{DL} = 26 $\pm$ 8 Oe per 10^7 A cm^{-2} (ξ^{y}_{STT} = 0.13 $\pm$ 0.03) at 400 K is attributed to the nonmagnetic SHE due to band spin-orbit coupling and is well within the range reported for Pt [64] or Pt alloys [84]. At 120 K, h^{y}_{DL} = 42 $\pm$ 16 Oe per 10^7 A cm^{-2} (ξ^{y}_{STT} = 0.30 $\pm$ 0.12), an increase attributed to the intrinsic conductivity from onset of the AFM phases. While there are no expected $\sigma^{x}_{xz}, \sigma^{z}_{xz}$ from the collinear AFM state, the symmetry does not prevent an intrinsic isotropic σ^{y}_{xz} [13, 38, 85] and the additional change from the onset of the non-collinear phase is $< 10\%$ of the intermediate phase value. In contrast to other recent observations of $\hat{p} = \hat{x}, \hat{z}$ spin currents in non-collinear AFMs [15, 47], the samples in this work yield higher h^{x}_{DL}/h^{y}_{FL} (up to 0.8) and h^{z}_{DL}/h^{y}_{FL} (up to 0.2), and are highly anisotropic with respect to crystal/AFM domain orientation. The notion that these components are exclusively tied to s-d exchange physics in the non-collinear state is well supported by their lack of existence in the collinear and non-magnetic states above 200 K - 250 K. This corresponds well with a recent study of Mn_3GaN, which has no intermediate collinear state, and where these components emerge smoothly through the Néel transition [15].

CHAPTER 5

Conclusion and Outlook

5.1 Summary of Results

This body of work has shown that thin film $L1_2$-ordered $PtMn_3$ generates unconventional spin Hall conductivity tensor components ($\sigma^x_{xz}, \sigma^z_{xz}$) that have an orientation-dependent anisotropy, are unique to the non-collinear antiferromagnet state, and are consistent with symmetry analysis. This current direction-dependent anisotropy can be used to change the ratio of $\hat{p} = \hat{x}, \hat{y}, \hat{z}$ out-of-plane spin current and select for a dominant polarization component. The mean spin transfer torque efficiencies in the $PtMn_3$/Py devices (ξ^x_{DL} = 0.18, ξ^z_{DL} = 0.06, ξ^y_{DL} = 0.30) exceed that of the canonical fcc Pt ($\xi^y_{DL} \sim 0.1$), which supports itinerant electron exchange with the magnetic lattice as a stronger mechanism for spin current generation than spin-orbit coupling [38]. These results suggest that non-collinear antiferromagnets could bridge the gap in spin torque efficiency between heavy metals such as Pt, W and topological insulators such as 2D bismuth selenides [8] and tellurides [73]. Moreover, the strong orientation-dependent anisotropy of the spin Hall conductivity offers selectivity of out-of-plane spin current polarization, which may enable new developments in low power non-volatile spin-based electronics.

The remainder of this thesis outlines prospective extensions of the existing work for further materials development and for novel electronic applications. As discussed in chapter 4, an inability to control antiferromagnetic domain formation can result in devices with higher global symmetry where the expected linear response behavior is lost. Below, a proposal is outlined for controlling antiferromagnetic domain formation by using exchange coupling with an adjacent ferromagnetic thin film with favorable anisotropy. As the harmonic Hall effect data in chapter 4 shows, there is an emergent σ^z_{xz} in the low temperature non-collinear phase. This $\hat{z}$-polarized spin current could be used to deterministically and efficiently switch ferromagnetic films with perpendicular magnetic anisotropy (or as an efficient readout method through the inverse effect). An attempt at integrating a Pt/Co PMA ferromagnet with $PtMn_3$ and performing electric field switching is

outlined, and guidance is issued for future experiments. Finally, the prospect of $PtMn_3$ as a high "quantum inductor" is outlined. In non-collinear antiferromagnets, self-induction from moment canting under an applied internal current offers extraordinarily high inductance that has significant potential in RF nanoelectronics.

5.2 Control of Non-collinear Domain Formation with Magnetic Exchange

The control of antiferromagnetic domain formation in $PtMn_3$ is critical to ensure that there is a low global symmetry and to prevent cancellation of σ^i_{xz} via the existence of multiple domains in one device, as per Figure A.1. It may be possible to guarantee a single global domain with sufficient exchange coupling with a ferromagnetic substrate or interfacial layer that has an anisotropy axis in a [110]-equivalent direction, which would serve to orient the Kagome planes in the low temperature non-collinear state of $PtMn_3$ in the [111] direction globally. A plausible option for a compatible substrate with appropriate ferromagnetic geometry is $BiFeO_3$, a well-studied magnetoelectric multiferroic with an orthogonal polarization and magnetization coupling that can be oriented along [111]-equivalent directions with an external electric field [86]. The magnetic moment per iron atom in $BiFeO_3$ is 0.1-1 μ_B per Fe, depending on the overall film quality [87, 88], and exchange coupling to a ferromagnetic film has been previously demonstrated [89]. Epitaxially, $BiFeO_3$ should be compatible with $PtMn_3$, as highly ordered growth was previously demonstrated on a ferroelectric $BiTiO_3$ substrate [46]. One likely caveat to this approach is that the magnetic and ferroelectric ordering in multiferroics is linked directly to the crystal structure, and grain boundaries act as a hard limit on the maximum ordering length (these can be as low as 10s of nm in poorly optimized $BiFeO_3$ [90]). If epitaxial compatibility could be guaranteed, a metallic ferromagnet may be more conducive to the formation of a single global domain.

An excellent candidate for a ferromagnetic metal system that is both epitaxially compatible with $PtMn_3$ and can be grown to magnetically orient along the [110] direction is chemically disordered $Fe_{1-x}Ga_x$ (FeGa), a material this research group has significant experience with [91]. The lattice constant of bulk FeGa is around 2.9 Å, and it has a high magnetization of 1.8-2.2 μ_B per Fe [92]. High quality epitaxial growth of FeGa was recently demonstrated on a ferroelectric $(PbMg_{0.33}Nb_{0.67}O_3)_{1-x}$:$(PbTiO_3)_x$ (PMN-PT, a = 4.02 Å) substrate [91], with the FeGa [100] axis templating along the PMN-PT [110] direction for a better lattice match. This scheme is epitaxially compatible with both MgO (a = 4.2 Å) and STO (a = 3.9 Å), and the diagonally oriented FeGa could potentially be integrated with $PtMn_3$ as per the proposed heterostructure in Figure 5.1a.

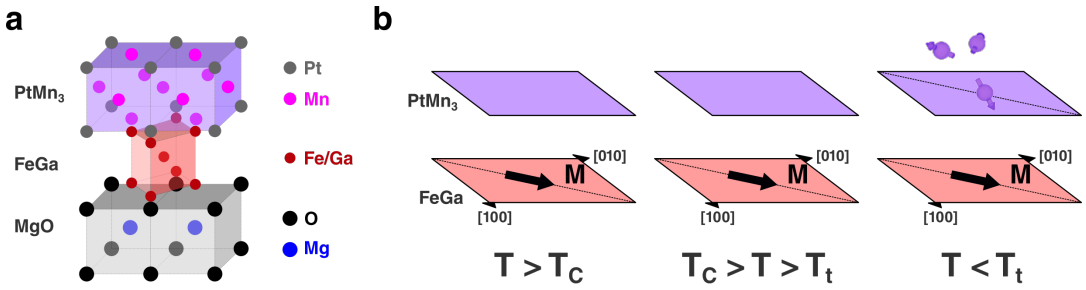

Figure 5.1: **Control of antiferromagnetic domain formation through exchange coupling with a ferromagnet**. **a**, Proposed thin film heterostructure of $PtMn_3$ with a FeGa alloy on MgO, which epitaxially templates along the [110] MgO direction due to the significantly lower lattice constant (previously grown in a prior work on PMN-PT [91]). **b**, As the FeGa Curie temperature ($>$ 900 K, can be tuned with Ga composition [92]) is higher than the $PtMn_3$ first order transition temperature ($<$ 400 K), it can be aligned along [110] with a cooling field and potentially induce global ordering of the $PtMn_3$ non-collinear texture along the same axis through exchange coupling.

As the Curie temperature of FeGa ($>$ 900 K [92]) is significantly higher than the $PtMn_3$ Néel transition, an applied external magnetic field along the substrate/$PtMn_3$ [110] direction during post-growth cooling would first align the FeGa to that direction. Then, due to exchange coupling with the globally magnetized FeGa, the $PtMn_3$ would ideally align to the same direction as it passes through the first order transition temperature (see Figure 5.1b). This alignment could potentially be done post film growth, assuming a vaccuum annealing apparatus existed that could assert the required magnetic field while reaching sample temperatures of $>$ 900 K. This method could potentially result in a single global non-collinear AFM domain and large, orientation-selectable out-of-plane spin current polarization, as per Figure A.1b.

5.3 Switching of Perpendicular Magnetic Anisotropy Ferromagnets

The primary target application of intrinsic spin current generating materials is the switching of patterned magnetic devices, such as the SHE-assisted MTJ structure shown in Figure 1.1f with in-plane anisotropy magnets such as CoFeB, Py, etc. In general, in-plane anisotropy magnets rely on shape anisotropy to define their hard axes, which mandates specific patterning of MTJ stacks and can be challenging for arbitrary device configurations and for dimensional scaling. In contrast, the anisotropy of perpendicularly magnetized (PMA) ferromagnets can stem from internal crystal anisotropy [93, 94], or interfacial exchange such as the Dzyaloshinskii–Moriya interaction

(DMI) [95–97]. In the latter case, it is possible to have very strong PMA nanomagnets with films that are only a few atomic layers thick, which is advantageous for device scaling. Additionally, the different fundamental anisotropy means that PMA magnets have lower critical switching currents [98]. Unfortunately, canonical SHE materials do not deterministically switch PMA magnets, as they only have σ_{xz}^{y} spin Hall conductivity in the out-of-plane direction. As shown in Figure 5.2a, spin currents with polarization perpendicular to the anisotropy axis (in this case $\hat{z}$), can only cause continual precession as there is no equilibrium precession around a stable direction. However, for $\hat{p} = \pm\hat{z}$ spin currents, as observed in the low temperature non-collinear state of $PtMn_3$, there is a stable equilibrium direction that the PMA magnetic moment precesses around, and stable deterministic switching can occur.

Preliminary attempts have been made to deposit a Pt/Co PMA stack onto $PtMn_3$ thin films and evalute the spin current switching ability at low temperature. The electrical schematic for this experiment is shown in Figure 5.2b, where a patterned $PtMn_3$(35 nm)/Pt(2 nm)/Co(1 nm)/Pt(3 nm) device is connected in parallel with a lock-in amplifier which measures the magnetization direction through the anomalous Hall resistance, and a DC current source. In this configuration, care must be taken to avoid electrical coupling between instruments, and so appropriate high/low-pass filters are placed on all Hall bar terminals to route the DC and harmonic signals correctly. To avoid anomalous switching and excess sample heating with the AC sense current with the lock-in amplifier, the amplitude is kept small, usually 100 times less than the maximum DC current. In Figure 5.2c-d, the field-dependent R_{xy} is measured for a Pt(2 nm)/Co(1 nm)/Pt(3 nm) PMA control sample, and the stack on $PtMn_3$, respectively. Both samples exhibit good perpendicular anisotropy across the full temperature range from 120-400 K, and have increased M_S and H_C at low temperature, as expected. The PMA stack on $PtMn_3$ shows some slight in-plane anisotropy at temperatures below 200 K, attributed to exchange with the non-collinear $PtMn_3$ spin texture, which has some in-plane projection in all domain orientations. For out-of-plane spin current switching, it would be ideal if the magnetic film was directly on top of the $PtMn_3$, but the first Pt layer was deemed necessary due to inconsistent PMA with $PtMn_3$/Co/Pt films. In general, the interface chemistry and growth kinetics present a challenge for integrating DMI-based PMA films with arbitrary materials. In this regard, further film growth development is required to get the Co layer as close as possible to the $PtMn_3$, and reduce the spin current dissipation in the interfacial Pt, which has a spin diffusion length in the 1-10 nm range [76].

Current switching of the $PtMn_3$(35 nm)/Pt(2 nm)/Co(1 nm)/Pt(3 nm) samples was attempted at 120 K in a Quantum Design Dynacool PPMS using the standard ETO puck and a custom break-out module to connect a lock-in amplifier and current source, as in Figure 5.2b. The Hall voltage versus $PtMn_3$ current density is shown in Figure 5.2e. Instead of the expected PMA switching

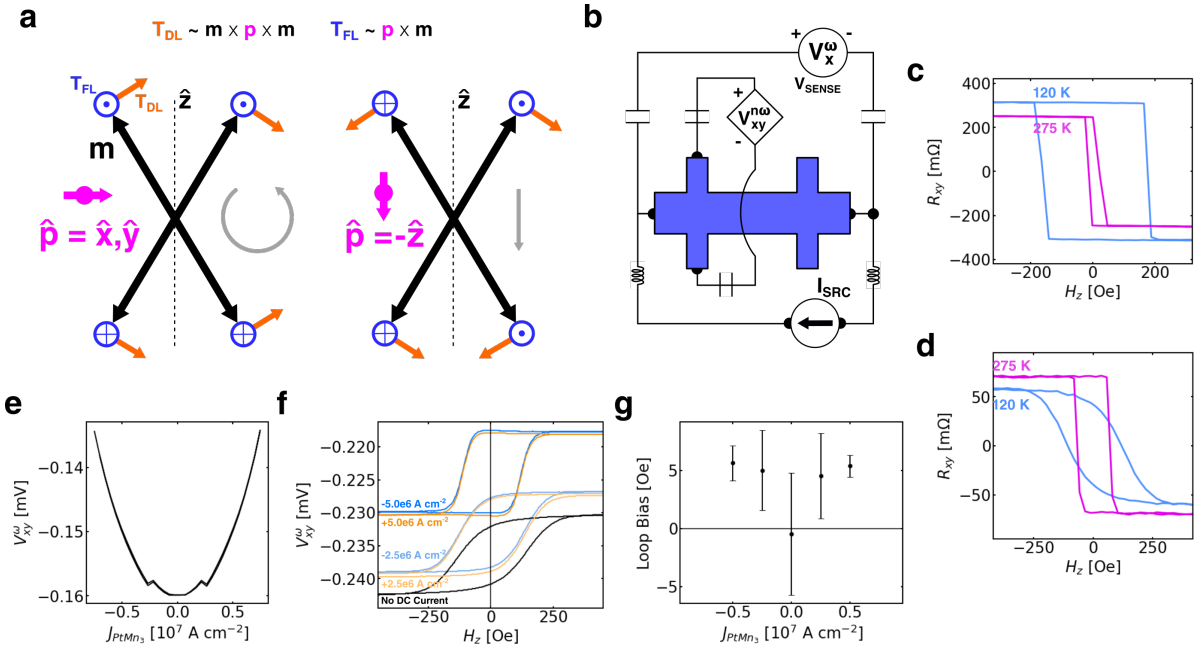

Figure 5.2: **Deterministic switching of a perpendicularly magnetized ferromagnet with $PtMn_3$.** **a**, Process schematic for spin current switching of a perpendicular magnetic anisotropy (PMA) ferromagnet with in-plane spin current $\hat{p} = \hat{x}, \hat{y}$ as from the canonical SHE (left), and unconventional out-of-plane $\hat{p} = -\hat{z}$ as found in the non-collinear $PtMn_3$ system (right). The combined effect of the damping-like (DL) and field-like (FL) torques with the in-plane $\hat{p} = \hat{x}, \hat{y}$ causes continous out-of-plane switching, while the $\hat{p} = -\hat{z}$ has a clear stable equilibrium near $\hat{m} = -\hat{z}$. **b**, Electrical measurement setup for DC PMA switching experiemtn with a $PtMn_3$/PMA heterostructure with a lock-in amplifier supplying small signal V_x^ω to measure the Hall resistance and a DC current source for switching. Sources are appropriately filtered to prevent DC/AC current injection between instruments. Anomalous Hall resistance versus out-of-plane external field H_z for patterned Hall devices of **c**, Pt(2 nm)/Co(1 nm)/Pt(3 nm) PMA control sample and, **d** $PtMn_3$(40 nm)/Pt(2 nm)/Co(1 nm)/Pt(3 nm) at 275 K and 120 K. The PMA stack on $PtMn_3$ shows broadening at high temperature and partial loss of perpendicular anisotropy at low temperature, perhaps due to exchange interactions with the different antiferromagnetic phases of $PtMn_3$. **e**, DC switching attempt of $PtMn_3$/PMA sample at 120 K showing only the standard heating response $V \sim J^2$ before device destruction in the $J_{PtMn_3} \sim 10^7$ A cm^{-2} range. **f**, Measurement of DC current induced bias in Hall voltage versus H_z loops, and **g** the extracted offset fields, which suggest a bias of ~ 10 Oe per 10^7 A cm^{-2}. In general, the expected effective field from σ_{xz}^z in the $PtMn_3$ layer is small compared to the coercive field at 120 K, and devices are destroyed before a significant bias can be detected. Pt/Co PMA control samples and heterostructures with $PtMn_3$ were developed in collaboration with N.M. Vu.

curve from Figure 5.2d, only a quadratic signal is detected, due to excessive device heating when the $PtMn_3$ current density approaches 10^7 A cm^{-2}. At $J_{PtMn_3} \sim 10^7$ A cm^{-2}, irreversible damage occurs, with full or partial loss of the magnetic response in Figure 5.2d. This current density limit

is too low to expect any switching to occur, given the respective properties of the $PtMn_3$ and the PMA stack at low temperature. Though it was not possible to evalute the field-like torques from $\hat{p} = \hat{z}$ out-of-plane spin currents in the main $PtMn_3$/Py study, the respective damping-like torques were measured to be ≤ 10 Oe per 10^7 A cm^{-2}. Assuming the a highly optimistic case that the $\hat{p} = \hat{z}, \hat{y}$ fields are of comparable value, the results in Figure 4.5 point to a maximum field strength of any component in the range of ~ 50 Oe per 10^7 A cm^{-2}. As per the external field switching of the $PtMn_3$/Pt(2 nm)/Co(1 nm)/Pt(3 nm) shown in Figure 5.2d, the saturation field is ~ 250 Oe, and would require $J_{PtMn_3} \geq 5 \cdot 10^7$ A cm^{-2} in the best case, which is currently unreachable due to excessive heating. An attempt was made to detect even small shifts in the PMA hysteresis loop with DC current biasing the Hall devices and measuring the offset in the field-dependent R_{xy}, shown in Figure 5.2f. The hysteresis loops shift significantly from the excessive sample heating, and show a perceptible bias in the range of 5 Oe (Figure 5.2g), but it is inexplicably unipolar with current, and the relative uncertainty is high (the shifts could represent a constant offset from the remnant magnetization of the PPMS bore). Realization of successful PMA switching with $PtMn_3$ will require additional development to increase the $\hat{p} = \hat{z}$ spin current reaching the Co without destroying the devices. If high quality $L1_2$ ordered $PtMn_3$ can be grown thinner, e.g. in the range of ~ 5 nm, it would decrease the power dissipated in the device for the same current density. Additionally, if the non-collinear phase could be stabilized at higher temperatures, as was done in a prior work [46], the PMA saturation field would be lower, approximately 50 Oe at room temperature. The potential for deterministic PMA switching with $PtMn_3$ is present, but will require further development to match the $\hat{z}$-polarized spin current efficiency with the thermal, structural, and magnetic requirements of the full device.

5.4 Quantum Self-Inductance

The main focus of this thesis is the spin Hall conductivity acquired by conduction electrons fron a linear response due to itinerant electron exchange with the magnetic lattice. In a spintronics mindset, it makes sense to focus on the spin current generation, and the structure of the spin Hall conductivity tensor. There is however, a complementary set of effects in the charge conductivity tensor. For conduction electrons travelling through an arbitrary spin texture with local magnetic orientation $\boldsymbol{n}(\boldsymbol{x})$, there arises an internal electric field [99]:

$$\mathcal{E}_i = \frac{\hbar}{e} \boldsymbol{n} \cdot (\partial_i \boldsymbol{n} \times \partial_t \boldsymbol{n}) \tag{5.4.1}$$

It is clear from this expression that ferromagnets and collinear antiferromagnets would not produce large $\mathcal{E}_i$ due to the lack of significant spatial variation in the spin texture, encoded by $\partial_i \boldsymbol{n}$, and the overall low solid angle in the magnetization coordinate that their precession would cause. For non-collinear antiferromagnets with simple enough textures, Equation 5.4.1 can be worked out exactly, as in the case of helical antiferromagnets that spiral along a main anisotropy axis [100]. For that system specifically:

$$\mathcal{E}_i = \frac{\hbar}{e}\frac{2\pi P}{\lambda}\partial_t \phi \sim \mathcal{L}\partial_t J \tag{5.4.2}$$

where ϕ is the moment tilt angle, proportional to the applied current density J, P is the spin polarization factor, and λ is the periodicity of the full spin structure. Because of the direct current dependence of ϕ, this is equivalently a function of $\partial_t J$ proportional to some effective inductance $\mathcal{L}$, as shown. This phenomenon has been termed "quantum self-inductance", and has been recently observed in assorted non-collinear magnets, with the largest effects being seen in the helical non-collinear antiferromagnet $Gd_3Ru_4Al_{12}$ [101]. In the case of $Gd_3Ru_4Al_{12}$, the volumetric quantum inductance (in H m^{-3}) was shown to be $\sim 10^6$ times larger in amplitude than the leading commercial alternatives at the time, as well as *negative* [101].

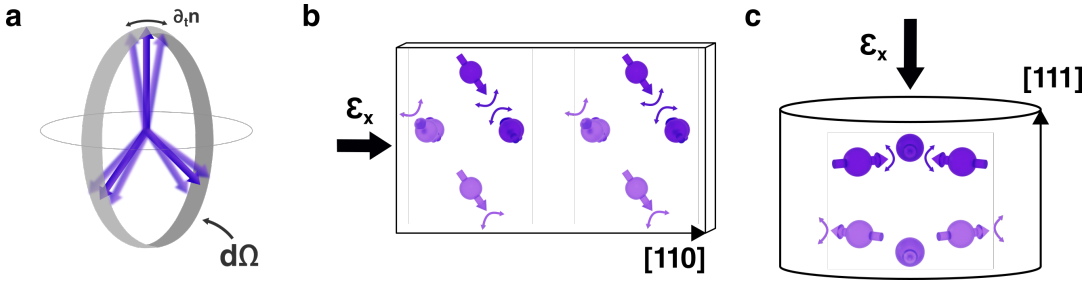

Figure 5.3: **Quantum self-inductance in $PtMn_3$.** **a**, Schematic of the antiferromagnetic sublattices of $PtMn_3$ deflecting under applied current in the [111] direction, and the resulting solid angle $d\Omega$, which is proportional to the quantum self-inductance. **b**, Hypothetical bar inductor device for a (001)-oriented $PtMn_3$ thin film, as in this work. **c**, If synthesis of (111)-oriented $L1_2$ $PtMn_3$ film is possible, it could be patterned into disk/pillar out-of-plane inductive devices, greatly reducing the device footprint.

The spin structure of the non-collinear antiferromagnetic phase of $PtMn_3$ suggests that it may be a good quantum inductor. The emergent electric field in the helical spiral texture in $Gd_3Ru_4Al_{12}$ is inversely proportional to the periodicity, and directly proportional to the solid angle covered by the magnetic moments during one oscillation. For $PtMn_3$, the periodicity of the texture is the distance between identical Kagome planes d = $\sqrt{3}a \sim 6.65$ Å, significantly smaller than the $Gd_3Ru_4Al_{12}$ spiral period of ~ 28 Å. Additionally, the magnetic moments in non-collinear $PtMn_3$ carve out a full hemisphere as per Figure 5.3a. With the existing (001)-oriented thin films,

longitudinal measurements of the quantum inductance could be obtained at various orientations, for example the [110]-oriented bar shown in Figure 5.3b. Additionally, if the lattice periodicity is to be minimized, it may be worthwhile to explore growth of (111)-oriented $L1_2$ $PtMn_3$, and pattern pillar devices as shown in Figure 5.3c. There are a profound number of potential applications of a nanoscale negative inductor with comparable amplitude to large-area patterned inductor elements. For an example RF nanoelectronics application, a high density negatively inductive element can be placed in series with a parasitic impedance to effectively eliminate it from the circuit.

APPENDIX A

Calculations of Anisotropic Spin Hall Conductivity in (001)-oriented $PtMn_3$

Spin conductivity tensors for the XMn_3 materials (X = Pt, Rh, Ir) were calculated via density functional theory in a prior work [33]. In that work, the noncollinear Kagome phase was found to have a strong anisotropic spin conductivity primarily along the [111] direction (charge current along [111] creates transverse spin current in the orthogonal plane). For the epitaxially templated systems in this work, current is applied within the (001) plane, and the coordinate system and spin orientations must be mapped from the original basis. The original basis for the DFT calculations is $\hat{x}'$ = $[1\bar{1}0]$, $\hat{y}'$ = $[11\bar{2}]$, $\hat{z}'$ = [111] [33]. To calculate the generated spin currents in some Hall device with coordinates $\hat{x}, \hat{y}, \hat{z}$, as in Figure 1.3a, the applied electric field is projected into the original basis, then the resulting spin current direction and polarization is projected back into the Hall device basis. Specifically, for some applied field direction $\hat{\mathcal{E}} = \epsilon_1\hat{x} + \epsilon_2\hat{y} + \epsilon_3\hat{z}$, the resulting spin current in the direction $\hat{r} = r_1\hat{x} + r_2\hat{y} + r_3\hat{z}$ with polarization $\hat{i}, i \in (x, y, z)$ is:

$$J^i_{\hat{\mathcal{E}},\hat{r}} = \sum_{i'} \left(\hat{i} \cdot \hat{i}'\right) \left[\boldsymbol{R} \cdot \sigma^{i'} \cdot \boldsymbol{E}\right] \tag{A.0.1}$$

where $\boldsymbol{R} = \sum_{i'} \left(\hat{r} \cdot \hat{i}'\right) \hat{i}'$, $\boldsymbol{E} = \sum_{i'} \left(\hat{\mathcal{E}} \cdot \hat{i}'\right) \hat{i}'$ are the projections of the spin current direction and applied electric field into the original basis, respectively, and $\sigma^{i'}$ is the spin Hall conductivity tensor for polarization along $\hat{i}'$ in the original basis. There is a difference in spin projection between the two bases that is accounted for in the $\left(\hat{i} \cdot \hat{i}'\right)$ term in Equation A.0.1. Finally, because the electric field and spin current directions are already normalized in this formulation, $\sigma^i_{xz} = J^i_{\hat{x},\hat{z}}$ directly.

As the magnetic heterostructures in this work are out-of-plane, the relevant conductivity is σ^i_{xz} for each spin polarization, where the final $\hat{x} \cdot [100] = \cos\phi_{100}$ is the lengthwise orientation of the Hall channel (and the direction of supplied current), and $\hat{z}$ = [001] always. For a patterned device with multiple AFM domains, the resulting spin conductivity is calculated by using the

appropriate device coordinates and averaging by the number of domain types. For example, if there are twin domains with (111) and $(11\bar{1})$ Kagome planes, the device bases are $\hat{x}_{111}$ = [100], $\hat{y}_{111}$ = [010], $\hat{z}_{111}$ = [010], and $\hat{x}_{11\bar{1}}$ = [001], $\hat{y}_{11\bar{1}}$ = [100], $\hat{z}_{11\bar{1}}$ = $[00\bar{1}]$. The computed transverse (σ^i_{xz}) and longitudinal (σ^i_{xx}) spin conductivities for assorted domain degeneracies are shown in Figure A.1. The resulting transverse spin current texture for devices along various orientations is shown in Figure A.2, and compared to a typical heavy metal spin Hall effect system. The python code used to calculate the spin Hall conductivity tensor components for Figure 1.3, Figure 4.3b, and Figure A.1 is shown in Source Code A.1. The python code used to generate the transverse spin textures in Figure A.1 is shown in Source Code A.2.

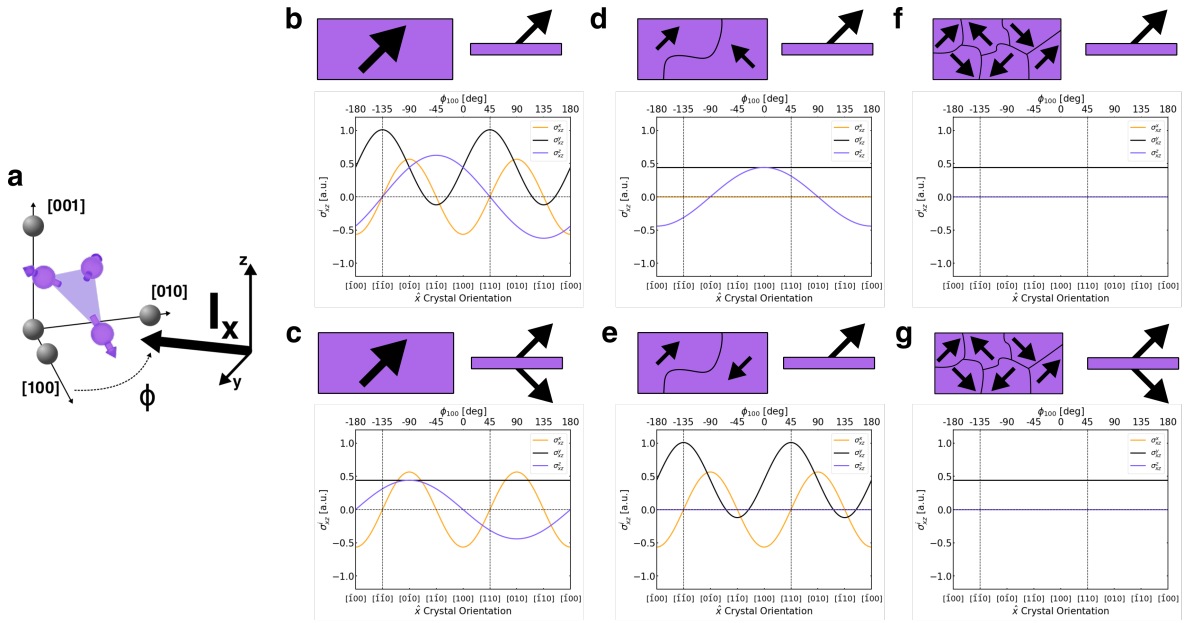

Figure A.1: **Orientation-dependent spin Hall conductivity in multi-domain noncollinear $PtMn_3$.** **a**, Schematic of noncollinear phase of $L1_2$ ordered $PtMn_3$ showing coordinate system for conductivity tensor calculations. **b**, σ^i_{xz} tensor elements for $i = x, y, z$ in the [100], [010], [001] basis for a single AFM domain with Kagome planes with [111] surface normal (black arrow, in-plane projection), along a direction $\hat{x} = [100] + (\cos\phi_{[100]}, \sin\phi_{[100]}, 0)$ based on prior DFT results [33], and rotated into the proper basis. The same for **c** [111],$[11\bar{1}]$, **d** [111],$[\bar{1}11]$, **e** [111],$[\bar{1}\bar{1}1]$, **f** [111],$[\bar{1}11]$,$[1\bar{1}1]$,$[\bar{1}\bar{1}1]$, and **g** all 8 [111]-equivalent domains in equal proportion. In any patterned device, the composition of out-of-plane spin conductivity is highly dependent on both crystal orientation and antiferromagnetic domaining. In general, the higher the global symmetry, the more tensor elements are reduced or eliminated altogether.

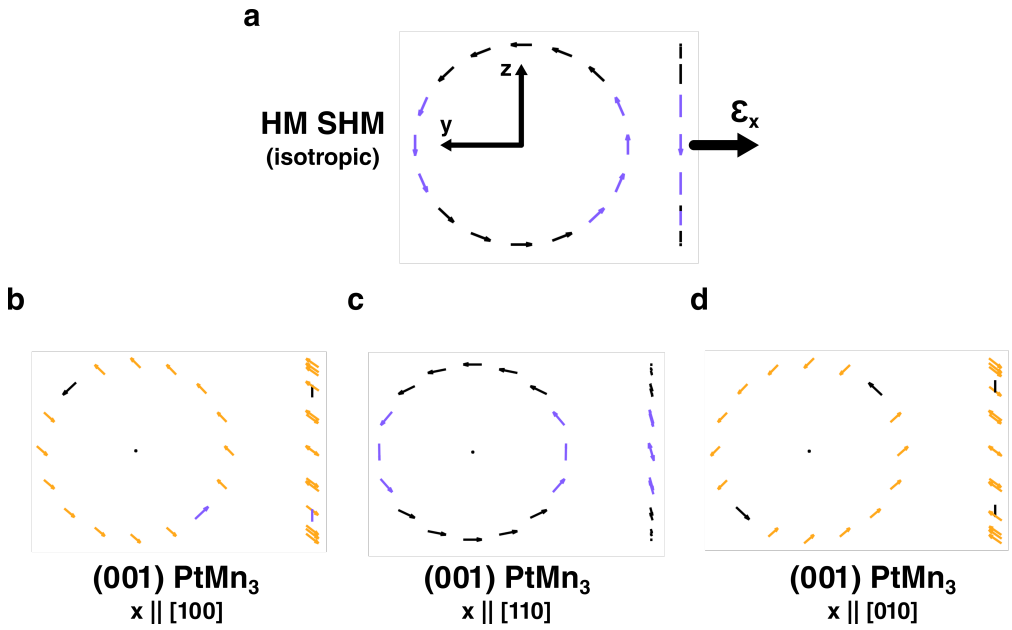

Figure A.2: **Orientation-dependent transverse spin current textures in single-domain non-collinear PtMn$_3$.** Transverse spin current polarization for all directions orthogonal to the applied current direction $\hat{x}$ for **a**, a typical heavy metal spin Hall effect system (HM SHM) such as Pt, W. The profile in **a** is the typical left handed circular polarization and is isotropic for all orientations of $\hat{x}$ in the crystal. For PtMn$_3$ with a single AFM domain oriented along [111] the texture is anisotropic with orientation and has varying $\hat{p} = \hat{x}, \hat{y}, \hat{z}$ components, as shown for **b**, $\hat{x} \parallel [100]$, **c**, $\hat{x} \parallel [110]$, and **d** $\hat{x} \parallel [010]$.

Source Code A.1: Calculation of orientation-depdendent longitudinal σ^i_{xx}, and transverse σ^i_{xz} spin Hall conductivity tensor components of the non-collinear antiferromagnetic ground state of $L1_2$ $PtMn_3$ with respect to an applied external current along $\hat{x}$. The anisotropy and amplitude of each element varies greatly with antiferromagnetic domain composition, as shown in Figure A.1.

```
# pm3_shc.py
# Steve Novakov 2021-07-29
# Desc: spin Hall conductivity tensor calculations for patterned in-plane
#       Hall devices of (001)-oriented PtMn3

import numpy as np
import numpy.linalg as la

b111 = [[1,0,0], [0,1,0], [0,0,1]]
b1n1 = [[0,1,0], [-1,0,0], [0,0,1]]
bn11 = [[0,-1,0], [1,0,0], [0,0,1]]
bnn1 = [[-1,0,0], [0,-1,0], [0,0,1]]
b11n = [[0,1,0], [1,0,0], [0,0,-1]]
b1nn = [[1,0,0], [0,-1,0], [0,0,-1]]
bn1n = [[-1,0,0], [0,1,0], [0,0,-1]]
bnnn = [[0,-1,0], [-1,0,0], [0,0,-1]]

# USER INPUT

# bases = [b111, b1n1, bn11, bnn1, b11n, b1nn, bn1n, bnnn]
# bbs = "all"

bases = [b111]
bbs = "111"

def Projector(x, y, z, jr):

    x0 = np.array([1, -1, 0])
    x0 = x0 / la.norm(x0)
    y0 = np.array([1, 1, -2])
    y0 = y0 / la.norm(y0)
    z0 = np.array([1, 1, 1])
    z0 = z0 / la.norm(z0)

    shcx = np.array([[-66, 0,0], [0, 66, 108], [0, 7, 0]])
    shcy = np.array([[0, 66, -108], [66, 0,0], [-7, 0,0]])
```

```
    shcz = np.array([[0, 32, 0], [-32, 0,0], [0,0,0]])

    xproj = np.array([x0.dot(x), y0.dot(x), z0.dot(x)])
    yproj = np.array([x0.dot(y), y0.dot(y), z0.dot(y)])
    zproj = np.array([x0.dot(z), y0.dot(z), z0.dot(z)])
    rproj = np.array([x0.dot(jr), y0.dot(jr), z0.dot(jr)])

    jrx0 = rproj.dot(shcx.dot(xproj))
    jry0 = rproj.dot(shcy.dot(xproj))
    jrz0 = rproj.dot(shcz.dot(xproj))

    jj = np.array([jrx0, jry0, jrz0])

    jrx = jj.dot(xproj)
    jry = jj.dot(yproj)
    jrz = jj.dot(zproj)

    return [jrx, jry, jrz]

def Rz(alpha):

    mat = [[np.cos(alpha), -1*np.sin(alpha), 0],\
           [np.sin(alpha), np.cos(alpha), 0],
           [0,0,1]]

    return np.array(mat)

# Rotate X,Y,Z from Zhang, Y., et al. (2017) into new x,y,z
# new x,y,z is std. caretsian coordinates rotated around z by phi

phis = np.linspace(-1*np.pi, np.pi, 360)
norm = 100.0

s_xz_x = []
s_xz_y = []
s_xz_z = []
s_xx_x = []
s_xx_y = []
s_xx_z = []

nb = len(bases)

for p in phis:
```

```
80
81      xzx = 0
82      xzy = 0
83      xzz = 0
84      xxx = 0
85      xxy = 0
86      xxz = 0
87
88      for b in bases:
89
90          bb = np.array(b)
91          x = bb[0]
92          y = bb[1]
93          z = bb[2]
94
95          rm = Rz(p)
96
97          x = rm.dot(x)
98          y = rm.dot(y)
99          z = rm.dot(z)
100
101         sx, sy, sz = Projector(x,y,z,z)
102
103         xzx += sx/nb
104         xzy += sy/nb
105         xzz += sz/nb
106
107         sx, sy, sz = Projector(x,y,z,x)
108
109         xxx += sx/nb
110         xxy += sy/nb
111         xxz += sz/nb
112
113     s_xz_x.append(xzx)
114     s_xz_y.append(xzy)
115     s_xz_z.append(xzz)
116     s_xx_x.append(xxx)
117     s_xx_y.append(xxy)
118     s_xx_z.append(xxz)
119
120 s_xz_x = np.array(s_xz_x) / norm
121 s_xz_y = np.array(s_xz_y) / norm
122 s_xz_z = np.array(s_xz_z) / norm
```

```
s_xx_x = np.array(s_xx_x) / norm
s_xx_y = np.array(s_xx_y) / norm
s_xx_z = np.array(s_xx_z) / norm

# output to files

head = "s_xz^x,s_xz^y,s_xz^z,s_xx^x,s_xx^y,s_xx^z"

outarray = np.array([s_xz_x, s_xz_y, s_xz_z, s_xx_x, s_xx_y, s_xx_z])
outarray = outarray.T

np.savetxt("shc_components.csv", outarray, header=head)
\end{python}
```

Source Code A.2: Calculation of transverse spin current texture of the non-collinear antiferromagnetic ground state of $L1_2$ $PtMn_3$ and a traditional spin Hall metal (e.g. Pt), with respect to an applied external current along some arbitrary direction in the (001) plane.

```
# pm3_shc.py
# Steve Novakov 2021-08-20
# Desc: transverse spin current texture calculation and film creation of
 ↪  in-plane
#       Hall devices of (001)-oriented PtMn3, Pt

import numpy as np
import numpy.linalg as la
import matplotlib.pyplot as pt
from mpl_toolkits.mplot3d import Axes3D
import matplotlib.gridspec as gridspec
from celluloid import Camera
from IPython.display import HTML

def Projector(x, y, z, jr):

    x0 = np.array([1, -1, 0])
    x0 = x0 / la.norm(x0)
    y0 = np.array([1, 1, -2])
    y0 = y0 / la.norm(y0)
    z0 = np.array([1, 1, 1])
    z0 = z0 / la.norm(z0)

    shcx = np.array([[-66, 0,0], [0, 66, 108], [0, 7, 0]])
```

```
24      shcy = np.array([[0, 66, -108], [66, 0,0], [-7, 0,0]])
25      shcz = np.array([[0, 32, 0], [-32, 0,0], [0,0,0]])
26
27      xproj = np.array([x0.dot(x), y0.dot(x), z0.dot(x)])
28      yproj = np.array([x0.dot(y), y0.dot(y), z0.dot(y)])
29      zproj = np.array([x0.dot(z), y0.dot(z), z0.dot(z)])
30      rproj = np.array([x0.dot(jr), y0.dot(jr), z0.dot(jr)])
31
32      jrx0 = rproj.dot(shcx.dot(xproj))
33      jry0 = rproj.dot(shcy.dot(xproj))
34      jrz0 = rproj.dot(shcz.dot(xproj))
35
36      jj = np.array([jrx0, jry0, jrz0])
37
38      jrx = jj.dot(xproj)
39      jry = jj.dot(yproj)
40      jrz = jj.dot(zproj)
41
42      return [jrx, jry, jrz]
43
44  def ProjectorPt(x, y, z, jr):
45
46      x0 = np.array([1, 0, 0])
47      y0 = np.array([0, 1, 0])
48      z0 = np.array([0, 0, 1])
49
50      shcx = np.array([[0,0,0], [0, 0, 1], [0, -1, 0]])
51      shcy = np.array([[0, 0, -1], [0,0,0], [1,0,0]])
52      shcz = np.array([[0, 1, 0], [-1, 0,0], [0,0,0]])
53
54      xproj = np.array([x0.dot(x), y0.dot(x), z0.dot(x)])
55      yproj = np.array([x0.dot(y), y0.dot(y), z0.dot(y)])
56      zproj = np.array([x0.dot(z), y0.dot(z), z0.dot(z)])
57      rproj = np.array([x0.dot(jr), y0.dot(jr), z0.dot(jr)])
58
59      jrx0 = rproj.dot(shcx.dot(xproj))
60      jry0 = rproj.dot(shcy.dot(xproj))
61      jrz0 = rproj.dot(shcz.dot(xproj))
62
63      jj = np.array([jrx0, jry0, jrz0])
64
65      jrx = jj.dot(xproj)
66      jry = jj.dot(yproj)
```

```
67      jrz = jj.dot(zproj)
68
69      return [jrx, jry, jrz]
70
71  def Rz(alpha):
72
73      mat = [[np.cos(alpha), -1*np.sin(alpha), 0],\
74             [np.sin(alpha), np.cos(alpha), 0],
75             [0,0,1]]
76
77      return np.array(mat)
78
79  def ProjectionColor(spin):
80
81      aspin = np.abs(spin)
82      px, py, pz = aspin
83
84      if np.amax(aspin) == px:
85          return "#ffa81a"
86      elif np.amax(aspin) == py:
87          return "black"
88      elif np.amax(aspin) == pz:
89          return "#825cff"
90
91  b111 = [[1,0,0], [0,1,0], [0,0,1]]
92
93  theta = np.linspace(0, 2*np.pi, num=16, endpoint=False)
94  ry = np.cos(theta)
95  rz = np.sin(theta)
96
97  n = theta.shape[0]
98
99  fig = pt.figure(figsize=(30,15))
100 ax = fig.add_subplot(121, projection='3d', azim=-180, elev=0)
101 ax2 = fig.add_subplot(122, projection='3d', azim=-90, elev=0)
102
103 camera = Camera(fig)
104
105 degs = np.linspace(0,360,int(360/1.) + 1)
106
107 for deg in degs:
108
109     #print(deg)
```

```
110
111     for i in range(0, n):
112
113         rr = np.array([0, ry[i], rz[i]])
114
115         bb = np.array(b111)
116         x = bb[0]
117         y = bb[1]
118         z = bb[2]
119
120         rm = Rz(np.radians(deg))
121
122         x = rm.dot(x)
123         y = rm.dot(y)
124         z = rm.dot(z)
125
126         rrr = rm.dot(rr)
127
128         sx, sy, sz = Projector(x,y,z,rrr)
129         #sx, sy, sz = ProjectorPt(x,y,z,rrr)
130
131         ss = np.array([sx, sy, sz])
132         ss /= np.linalg.norm(ss) * 5.0
133
134         pcolor = ProjectionColor(ss)
135
136         ax.quiver(*rr, *ss, color=pcolor, pivot="middle", linewidth=6)
137         ax2.quiver(*rr, *ss, color=pcolor, pivot="middle", linewidth=6)
138
139         for a in ax, ax2:
140             a.scatter(*rr, color=pcolor, s=300)
141
142     for a in ax, ax2:
143         a.set_xticks([])
144         a.set_yticks([])
145         a.set_zticks([])
146
147         a.set_xlim([-1,1])
148         a.set_ylim([-1,1])
149         a.set_zlim([-0.8,0.8])
150
151         a._axis3don = False
152
```

```
153     ax.scatter(0,0,0, color='black', s=300)
154
155     ax.quiver(0, 0, 0, 0, 0.5, 0, color='black', linewidth=10)
156     ax.quiver(0, 0, 0, 0, -0.0005, 0.5, color='black', linewidth=10)
157
158     ax.text(0,0.5,-0.25, r"$\hat{y}$", size=60, zorder=1, color='black')
159     ax.text(0,-0.1,0.45, r"$\hat{z}$", size=60, zorder=1, color='black')
160
161     ax2.text(-1.3,0,0, r"$\phi$ = " + str(int(deg)).zfill(3) +
        ↪  r"$^\circ$", size=60, zorder=1, color='black')
162     ax2.text(0.7,0,0.2, r"$\hat{x}$", size=60, zorder=1, color='black')
163
164     ax2.quiver(0.2, 0, 0, 0.6, 0, 0, color='black', linewidth=10)
165
166     fig.tight_layout()
167
168     camera.snap()
169
170 animation = camera.animate(interval=50, repeat = True)
171 animation.save("pm3_proj_1.mp4")
172 #animation.save("pt_proj_1.mp4")
```

APPENDIX B

XRD, Structural, and Chemical Characterization of $PtMn_3$ Thin Films

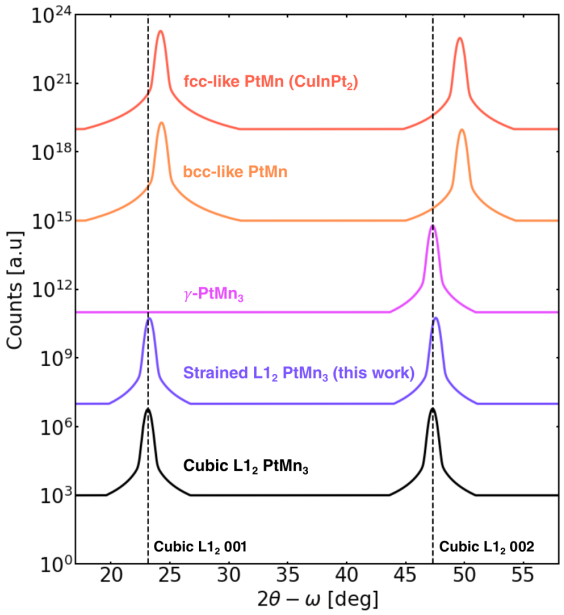

Figure B.1: **Simulated X-ray diffraction profiles of relevant (001)-oriented Pt-Mn intermetalltic thin films**. Theoretical out-of-plane X-ray diffraction profiles are shown for common Pt-Mn alloys and compared to the ideal cubic $L1_2$ $PtMn_3$ (001)-oriented thin film with a = c = 3.84 Å, and the tetragonally strained films on $SrTiO_3$ in this study. Depending on growth conditions, it is plausible to form any of the solid solution γ phase, or the bcc-like or $CuInPt_2$-like PtMn phase [49, 50]. Because of the qualitative similarity, confirmation of the cubic $L1_2$ phase requires additional evidence such as electron microscopy, chemical spectroscopy or neutron spectroscopy. XRD profiles were generated using structure factors and PseudoVoigt profiles for a planar Cu Kα X-ray beam with 0.5 degree divergence in CrystalDiffract (v6.9.2): a powder diffraction program for Mac and Windows. CrystalMaker Software Ltd, Oxford, England (www.crystalmaker.com).

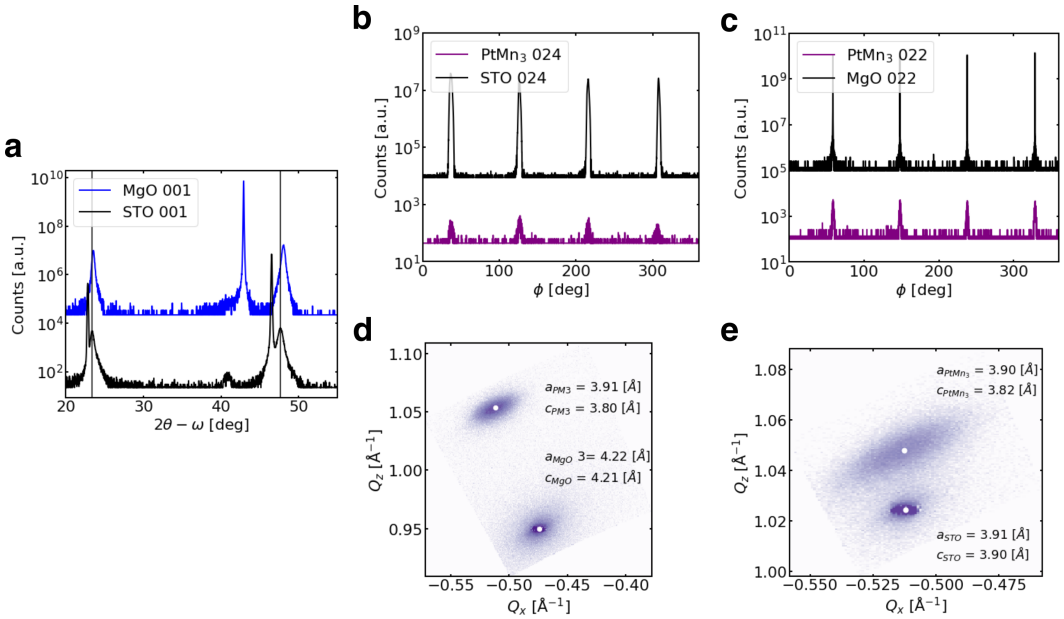

Figure B.2: **XRD of $PtMn_3$ Thin Films on $SrTiO_3$ and MgO**. **a**, out of plane XRD for $PtMn_3$ films of similar thicknesses grown on MgO (blue) and $SrTiO_3$ (black). Black vertical lines are placed at the $PtMn_3$ peaks for the $SrTiO_3$ (STO) sample, and show the increased tetragonality of the MgO samples. φ scans for both **b**, MgO and **c**, $SrTiO_3$ growths show epitaxial single-phase films with alignment to the substrate lattice. Reciprocal space map (RSM) of 024 film and substrate peaks for **d**, MgO and **e**, $SrTiO_3$ samples. All $PtMn_3$ films are templated to the substrate and exhibit large epitaxial strains, but the $SrTiO_3$ growths result in lower tetragonality due to the better lattice match. RSM data in **d**, **e** was obtained in collaboration with P.B. Meisenheimer [55].

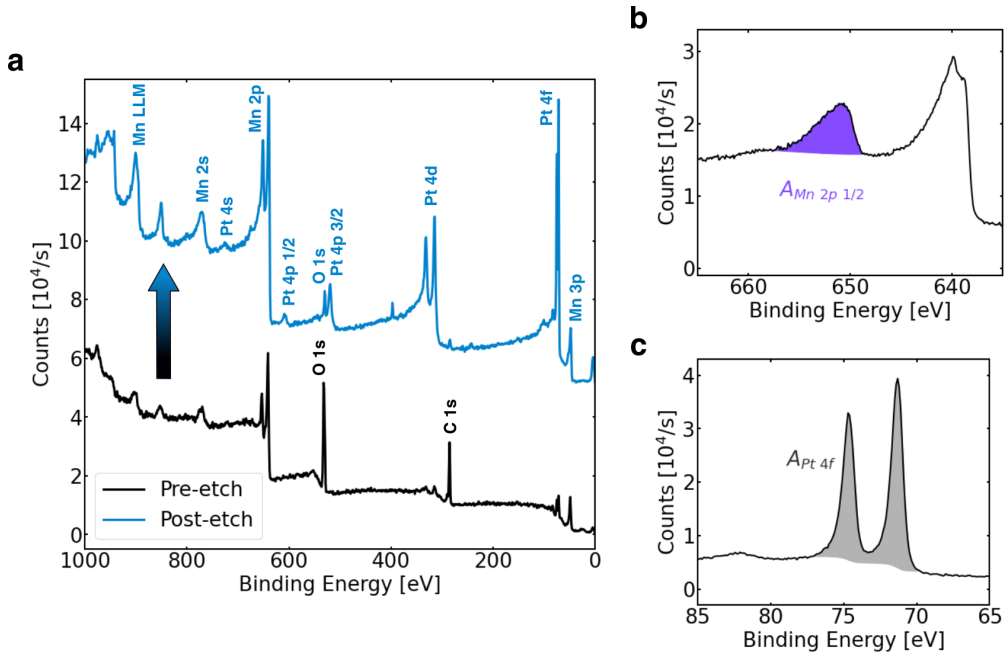

Figure B.3: **X-ray Photoelectron Spectroscopy of Reference $PtMn_6$ Target**. **a**, Broad survey XPS spectra of the polished backside of a reference $PtMn_6$ target pre (black) and post (blue) 600s ion beam etch to remove surface contaminants. The post etch **b**, Mn 2p complex and quantification region (Mn 2p 1/2 peak, shaded purple), and **c**, the Pt 4f complex and quantification region (shaded gray). For thin film quantification, the integrated peak intensity ratios are compared to these from the reference target to establish stoichiometry.

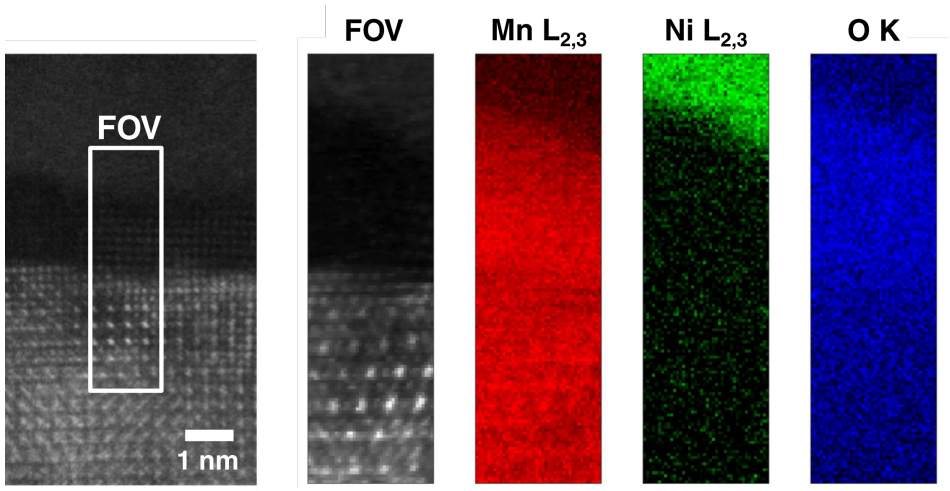

Figure B.4: **EELS map of MnO pocket on top $PtMn_3$ interface**. **a**, EELS map of ∼1.5 nm x 6 nm FOV near top interface across MnO cluster from an $SrTiO_3$/$PtMn_3$(66 nm)/Py(15 nm) sample showing Mn, Ni and O content. Mn diffusion to the surface is lowered by reducing high temperature exposure and not annealing post-growth. Mn interfacial regions seem to be fully MnO. To avoid MnO antiferromagnetism ($T_N \sim 115$ K), we perform all harmonic Hall effect measurements at T $\geq$ 120 K. This data was obtained in collaboration with G.A. Pan [55].

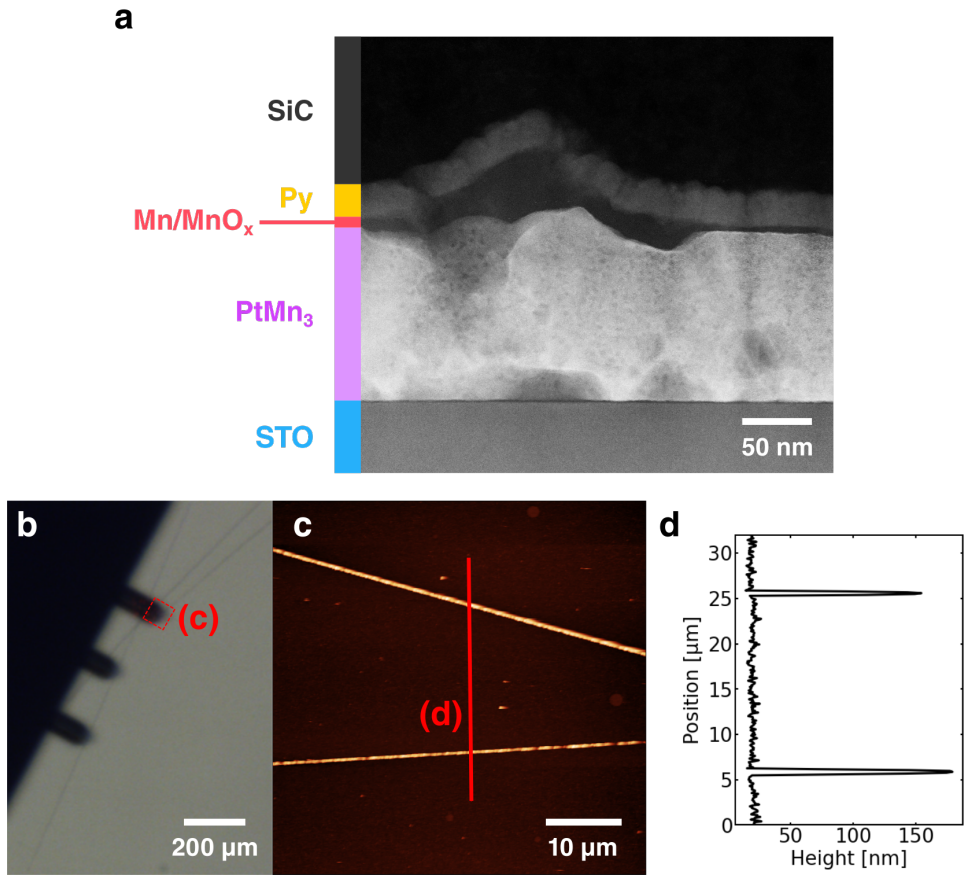

Figure B.5: **Surface manganese diffusion from high temperature annealing of $PtMn_3$ thin films**. **a**, Large field-of-view HAADF-STEM image of $SrTiO_3$/$PtMn_3$(120 nm)/Py(25 nm)/SiC sample grown for neutron diffraction measurements which underwent a 1 hour anneal at 700 °C in 50 mTorr Ar after deposition of the $PtMn_3$ layer. Post-growth annealing at these temperatures results in diffusion of Mn from the bulk of the $PtMn_3$ film to the surface, and formation of sparse macroscopic ridges of Mn that **b**, can be seen with an optical microscope. **c**, Topographic atomic force microscopy (AFM) of a small field of view containing these ridges and **d**, a height profile across them showing a consistent 1-2 μm width and up to 150 nm height (a likely overestimate due to scanning dynamics of the contact AFM tip). $PtMn_3$ films used for transport measurements in this work did not undergo any post-growth annealing and do not have visible ridges as in **b**, or significant Mn surface layers (though some diffusion does occur, and results in disconnected Mn pockets of 1-2 nm thickness as per Figure 2.3).

APPENDIX C

Magnetic Characterization of $PtMn_3$, $PtMn_3$/Py Thin Films

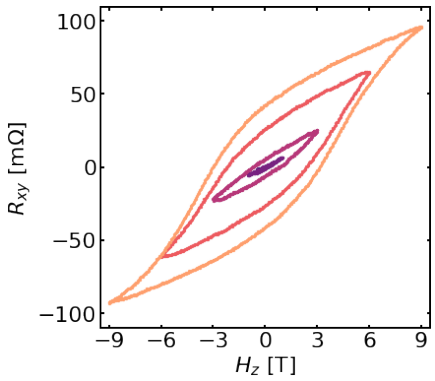

Figure C.1: **Anomalous Hall resistance in $PtMn_3$ on $SrTiO_3$ at 300 K]**. Anomalous Hall resistance of patterned $SrTiO_3$/$PtMn_3$(95 nm)/SiC vs. out-of-plane field H_z at 300 K under increasingly higher maximum field. The remnant magnetization does not saturate up to maximum fields of 9 T, a response typical of collinear antiferromagnets in the direction perpendicular to the main anisotropy axis.

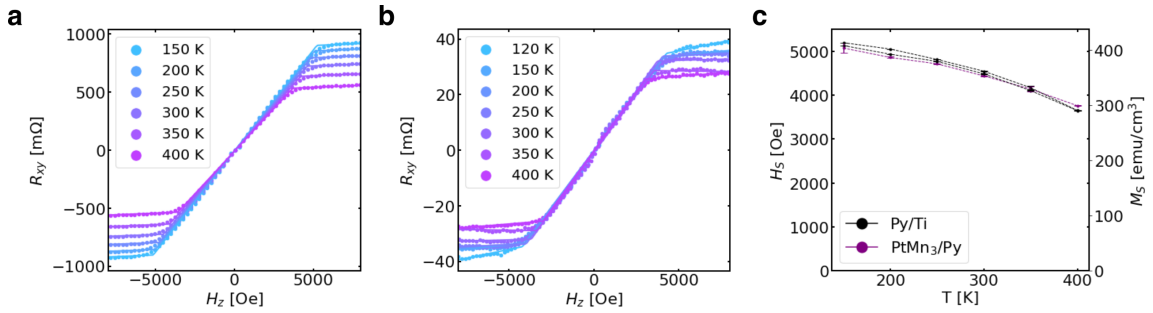

Figure C.2: **Out-of-plane anomalous Hall effect scans of Py and PtMn$_3$/Py**. Out-of-plane field scans of total device R_{xy} for patterned **a**, Al_2O_3/Py(15.0 nm)/TiO_2 and **b**, $SrTiO_3$/$PtMn_3$(46.6 nm)/Py(6.8 nm)/SiC Hall devices from 120 K - 400 K, showing the expected out-of-plane behavior of a uniaxial in-plane ferromagnet. **b**, saturation field H_S, saturation magnetization $M_S = H_S/4\pi$. The near identical H_S, M_S indicate a similar quality of Py film across samples.

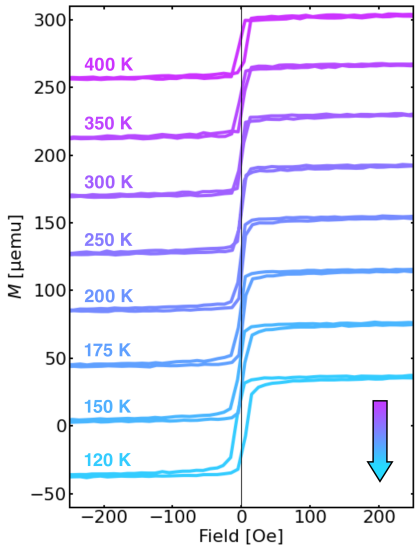

Figure C.3: **In-plane vibrating sample magnetometry of PtMn$_3$/Py**. In-plane vibrating sample magnetometry (VSM) of a 5 mm x 3 mm piece of the same $SrTiO_3$/$PtMn_3$(46.6 nm)/Py(6.8 nm)/SiC sample used for Hall devices from 120 K - 400 K and up to $\pm$250 Oe under an applied 50 Oe training field during temperature sweeps. VSM was performed in a Quantum Design Dynacool PPMS with the VSM option, and the sample was thermalized at each temperature step for 1 hour. There is no significant exchange bias and the Py is well saturated in-plane at 250 Oe, the minimum used for second harmonic Hall effect measurements.

APPENDIX D

Electronic Measurements of $PtMn_3$, $PtMn_3$/Py Thin Films

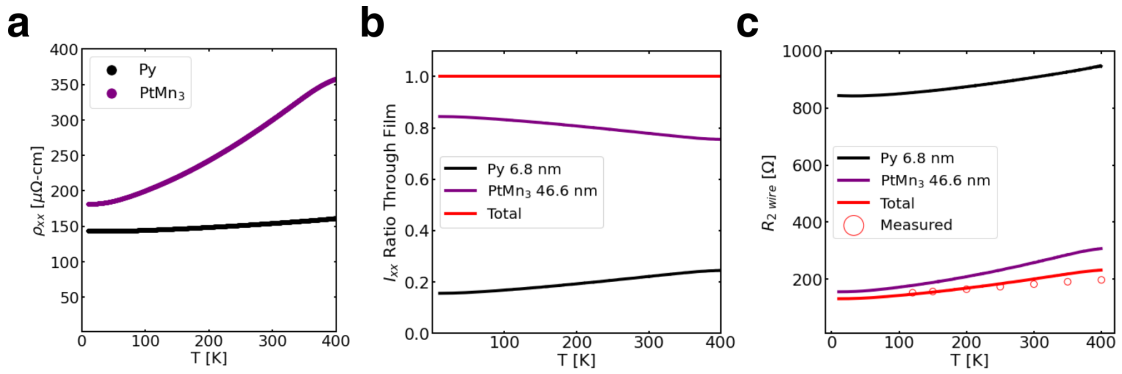

Figure D.1: **Device resistivity and current splitting in $PtMn_3$/Py Hall devices**. **a**, Resistivities of standalone $SrTiO_3$/$PtMn_3$(95 nm) and Al_2O_3/Py(15 nm) films, calculated via longitudinal 4-wire measurements of patterned Hall bar devices. **b**, The resulting current ratio in each film from 10 K - 400 K, assuming a parallel resistor model. **c**, Resistances of each film layer and total Hall channel resistance from 10 K - 400 K in the $SrTiO_3$/$PtMn_3$(46.6 nm)/Py(6.8 nm)/SiC devices used for harmonic Hall effect measurements, calculated from resistivity measurements of individual films. The calculated total channel resistance from the 4-wire resistivity scans closely matches the measured 2-wire device resistance (red circles).

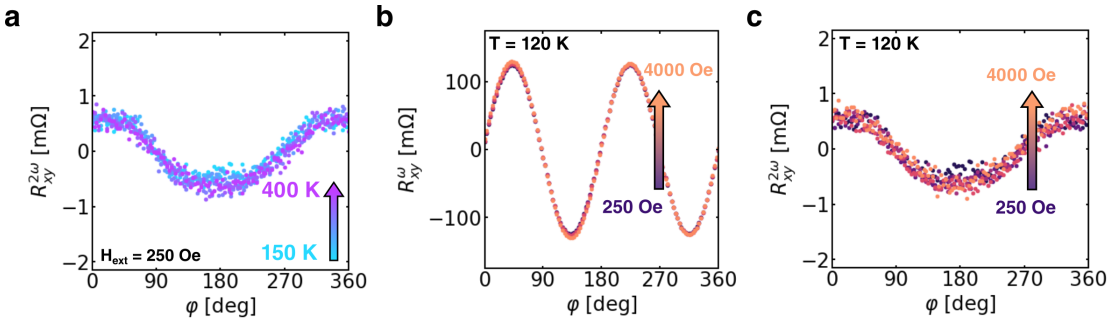

Figure D.2: **Harmonic Hall effect Py control measurement**. **a**, In-plane second harmonic Hall resistance $R_{xy}^{2\omega}$ from 150-400 K for a patterned Al_2O_3/Py(15 nm)/TiO_2 control sample with H_{ext} = 250 Oe. In-plane **b**, first and **c**, second harmonic Hall resistance for the same sample at 150 K vs. H_{ext} from 250-4000 Oe. For all temperature and H_{ext}, the control sample is well saturated, and the thermoelectric component of $R_{xy}^{2\omega}$ dominates ($\sim \cos\varphi$, no H_{ext} dependence). There is often a small detectable field-like torque from $\hat{p} = \hat{y}$ spin current attributed to the Rashba effect from the interface symmetry breaking with the Py and Al_2O_3 substrate, but it is consistently < 1 Oe per 10^7 A cm^{-2}.

APPENDIX E

Fitting Temperature Dependent Harmonic Hall Effect Data with BUMPS/DREAM

Fitting code and parameter error plots are provided for the free parameter fitting to a single $V_{xy}^{2\omega}$ frame as in Figure 4.4a-h. All such parameter fits in this work were done with the Bumps python package (v0.8.0) and the built in DREAM implementation. The script provided in Source Code E.1 handles the data and assigns it to a fitter. The free parameter fitter initializes the parameters according to the range of values in the data and then assigns them to individual $V_{xy}^{2\omega}(H_{ext}, \varphi)$ curves and executes the DREAM algorithm. The source code for the free parameter fitter is provided in Source Code E.2. The final output contains the parameter paths for each iteration of DREAM, and a distribution of final values, shown in Figure E.1. The fit is considered good if the values have a distribution that is unconstrained by the bounds and a small relative error.

For the fixed scaling parameter model used to extract the data in Figure 4.5, the spin torque effective field parameters are forced to follow strict $1/H_{ext}$, $1/(H_{ext} + H_S)$ scaling in a full dataset of $V_{xy}^{2\omega}(H_{ext}, \varphi)$ curves at a particular temperature. The vertical offset parameter is relaxed due to the anomalous scaling discussed in chapter 4. The script provided in Source Code E.3 handles the data and assigns it to a fitter. The strict scaling fitter initializes the parameters according to the range of values in the data and then assigns them to individual $V_{xy}^{2\omega}(H_{ext}, \varphi)$ curves and executes the DREAM algorithm. The source code for the scrict fitter is provided in Source Code E.4. The fitted curves and raw data for a $V_{xy}^{2\omega}(H_{ext}, \varphi)$ frame at 300 K is shown in Figure E.2a. The corresponding parameter distributions are shown in Figure E.2b.

Source Code E.1: Execution script for the free-parameter fit to the second harmonic Hall effect model.

```
# bumps_run_strict.py
# Steve Novakov 2021-07-29
# Desc: script to run differential evolution and DREAM fitting for second
# harmonic Hall effect data through the python BUMPS CLI. The fitter here
# has free parameter scaling for a each (p, H) curve at temperature tt

import subprocess as sp
import os
import sys
import time
import winsound
import json
import interpolants

de_steps = 2000
dream_steps = 3000

target_dir = "data_directory"
targets = ["DEVICE_ID_1", "DEVICE_ID_1", "DEVICE_ID_1"]

FITTER = "v2w_xyz_free"

DREAMS = False
#DREAMS = True

# DE ~ 191 secs per
# DREAMS ~ 600 secs per

start_time = time.time()

for target in targets:

  dirs = os.listdir(target_dir + "/" + target)

  for dir in dirs:

    if "DREAMS_2w" not in dir:
      continue

    stuff = dir.split("_")
```

```
41
42      tt = stuff[-1]
43
44      rootpath = target_dir + "/" + target
45      parampath = rootpath + "/DREAMS_2w_" + tt + "/" + \
46        FITTER + "-err.json"
47
48      wpath = target_dir + "/" + target + "/DE_2wPar_" + tt
49
50      command = ["python"]
51      command.append("-m")
52      command.append("bumps.cli")
53      command.append("./" + FITTER + "_params" + ".py")
54      command.append(rootpath)
55      command.append(parampath)
56      command.append(str(tt))
57      command.append("--overwrite")
58
59      if DREAMS:
60
61        dreampath = target_dir + "/" + target + "/DREAMS_2wPar_" + tt
62        parpath = wpath + "/" + FITTER + "_params" + ".par"
63
64        command.append("--fit=dream")
65        command.append("--burn=1500")
66        command.append("--steps={:}".format(int(de_steps)))
67        command.append("--init=lhs")
68        command.append("--trim=true")
69        command.append("--pars=" + parpath)
70        command.append("--store=" + dreampath)
71
72      else:
73
74        command.append("--fit=de")
75        command.append("--steps={:}".format(int(dream_steps)))
76        command.append("--store=" + wpath)
77
78      command.append("--batch")
79      sp.call(command, shell=True)
80
81      print("--- %s seconds ---" % (time.time() - start_time))
82
83  # play a sound when finished
```

```
84  winsound.Beep(100,500); winsound.Beep(400,500); winsound.Beep(200,500);
```

Source Code E.2: Fitting model for differential evolution/DREAM for the free-parameter fit to the second harmonic Hall effect model.

```
1   # v2w_xyz_free.py
2   # Steve Novakov 2021-07-29
3   # Desc: Actual fit model used for differential evolution and DREAM
    ↪  fitting
4   # to second harmonic Hall effect data through the python BUMPS CLI. The
    ↪  fitter
5   # here has free parameter scaling for a each (p, H) curve at temperature
    ↪  tt
6
7   import numpy as np
8   from bumps.names import Parameter, FitProblem, Curve
9   from bumps.parameter import Constant
10  import json
11  import sys
12
13  def V2WFit(phis, a, a_cp, a_c2pcp, a_c2p, a_sp, a_c2psp):
14
15    s = a_cp *  np.cos(phis)
16    s += a_c2pcp * np.cos(2*phis) * np.cos(phis)
17    s += a_c2p * np.cos(2*phis)
18    s += a_sp * np.sin(phis)
19    s += a_c2psp * np.cos(2*phis) * np.sin(phis)
20    s += a
21
22    return s
23
24  curves = []
25
26  args = sys.argv
27
28  opath = args[1]
29  tt = args[2]
30  hs = Constant(float(args[3]))
31
32  data = json.load(open(opath, "r"))
33
34  fields = sorted(list(data[tt].keys()), reverse=True, key=lambda x:
    ↪  float(x))
```

```
35
36  hmin  = np.amin(np.array(fields).astype(np.float))
37
38  for ii in range(0, len(fields)):
39
40    hh = fields[ii]
41
42    field = float(hh)
43    hext = Constant(field)
44
45    phis = np.radians(np.array(data[tt][hh]["phi"]))
46    v2wy = np.array(data[tt][hh]["v2wy"])
47
48    span = np.amax(v2wy) - np.amin(v2wy)
49    mid = (np.amax(v2wy) + np.amin(v2wy))/2.
50
51    dv2wy = 2e-7 * np.ones(v2wy.shape) * (field / hmin)**0.5
52    # increased error on lower amplitude points
53
54    a = Parameter(name="a_"+str(hh), value=mid).range(mid - span/2., mid +
      ↪  span/2.)
55    a_cp = Parameter(name="a_cp_"+str(hh), value=span/3.).range(-3*span,
      ↪  3*span)
56    a_c2pcp = Parameter(name="a_c2pcp_"+str(hh),
      ↪  value=span/3.).range(-3*span, 3*span)
57    a_c2p = Parameter(name="a_c2p_"+str(hh), value=span/3.).range(-3*span,
      ↪  3*span)
58    a_sp = Parameter(name="a_sp_"+str(hh), value=span/3.).range(-3*span,
      ↪  3*span)
59    a_c2psp = Parameter(name="a_c2psp_"+str(hh),
      ↪  value=span/3.).range(-3*span, 3*span)
60
61    if float(tt) > 390:
62
63        a = Parameter(name="a_"+str(hh), value=mid).range(-1*span/4,
          ↪  span/4.)
64        a_cp = Parameter(name="a_cp_"+str(hh),
          ↪  value=span/3.).range(-1*span, span)
65        a_c2pcp = Parameter(name="a_c2pcp_"+str(hh),
          ↪  value=span/3.).range(-1*span, span)
66        a_c2p = Parameter(name="a_c2p_"+str(hh),
          ↪  value=span/3.).range(-1*span, span)
```

```
        a_sp = Parameter(name="a_sp_"+str(hh),
        ↪  value=span/3.).range(-1*span, span)
        a_c2psp = Parameter(name="a_c2psp_"+str(hh),
        ↪  value=span/3.).range(-1*span, span)

    designator = "T{:d}_H{:d}".format(int(tt), int(hh))

    curves.append(Curve(V2WFit, phis, v2wy, dy=dv2wy, name=designator,\
      a=a, a_cp=a_cp, a_c2pcp=a_c2pcp, a_c2p=a_c2p, a_sp=a_sp,
      ↪  a_c2psp=a_c2psp))

problem = FitProblem(curves)
```

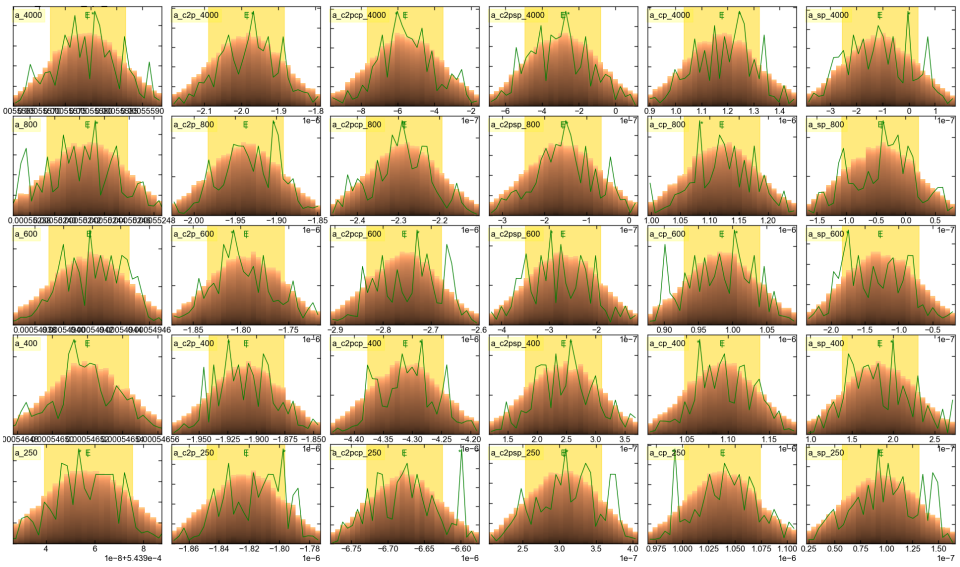

Figure E.1: **Parameter distributions from DREAM for free parameter fit to in-plane second harmonic Hall effect data**. Final distribution of fitted parameters from the DREAM algorithm for the device shown in Figure 4.4 in the free parameter scheme. Here, each amplitude for a particular component (e.g. $\cos\varphi$, $\sin\varphi$, etc) is unconstrained, and is found for each H_{ext}, φ profile for H_{ext} = (250, 400, 600, 800, 4000) Oe. The parameters and their errors are used to determine the scaling with respect to $1/H_{ext}$, $1/(H_{ext} + H_S)$.

Source Code E.3: Execution script for the strict parameter fit to the second harmonic Hall effect model with enforced $1/H_{ext}$, $1/(H_{ext} + H_S)$ field scaling.

```
# bumps_run_strict.py
# Steve Novakov 2021-07-29
# Desc: script to run differential evolution and DREAM fitting for second
```

```
4  # harmonic Hall effect data through the python BUMPS CLI. The fitter here
5  # has fixed parameter scaling for a single (p, H) frame at temperature tt
6
7  import subprocess as sp
8  import os
9  import sys
10 import time
11 import winsound
12 import json
13
14 de_steps = 2000
15 dream_steps = 3000
16
17 target_dir = "data_directory"
18 targets = ["DEVICE_ID_1", "DEVICE_ID_1", "DEVICE_ID_1"]
19
20 FITTER = "v2w_xyz_strict"
21
22 DREAMS = False
23 #DREAMS = True
24
25 # DE ~ 400 secs per
26 # DREAMS ~ 1900 secs per
27
28 start_time = time.time()
29
30 for target in targets:
31
32   raw_data_path = target_dir + "/" + target + "/CORRECTED_DATA.json"
33   root_path = target_dir + "/" + target
34
35   tar_data =  json.load(open(raw_data_path, "r"))
36   temps = sorted(list(tar_data.keys()), key=lambda x: int(x))
37
38   for tt in temps:
39
40     wpath = root_path + "/DE_2w_" + tt
41
42     command = ["python"]
43     command.append("-m")
44     command.append("bumps.cli")
45     command.append("./" + FITTER + ".py")
46     command.append(raw_data_path)
```

```
    command.append(root_path)
    command.append(str(tt))
    command.append("--overwrite")

    if DREAMS:

      dreampath = root_path + "/DREAMS_2w_" + tt
      parpath = wpath + "/" + FITTER + ".par"

      command.append("--fit=dream")
      command.append("--burn=1500")
      command.append("--init=lhs")
      command.append("--steps={:}".format(int(dream_steps)))
      command.append("--pars=" + parpath)
      command.append("--store=" + dreampath)

    else:

      command.append("--fit=de")
      command.append("--steps={:}".format(int(de_steps)))
      command.append("--store=" + wpath)

    command.append("--batch")

    sp.call(command, shell=True)

    print("--- %s seconds ---" % (time.time() - start_time))

# play a sound when finished
winsound.Beep(100,500); winsound.Beep(400,500); winsound.Beep(200,500);
```

Source Code E.4: Fitting model for differential evolution/DREAM for the strict parameter fit to the second harmonic Hall effect model with enforced $1/H_{ext}$, $1/(H_{ext} + H_S)$ field scaling.

```
# v2w_xyz_strict.py
# Steve Novakov 2021-07-29
# Desc: Actual fit model used for differential evolution and DREAM
 ↪  fitting
# to second harmonic Hall effect data through the python BUMPS CLI.
# The fitter here has fixed parameter scaling for a single (p, H) frame
# at temperature tt with a relaxed offset due to anomalous behavior of
 ↪  z-pol
```

```
7  # field like component.
8
9  import numpy as np
10 from bumps.names import Parameter, FitProblem, Curve
11 from bumps.parameter import Constant
12 import json
13 import sys
14 import interpolants
15
16 def V2WFit(phis, delta, h_off, hext, hs, vt, v_ra, v_rp, hoe,\
17     hy_fl, ry_dl, rx_fl, rx_dl, rz_dl):
18
19   a_ra = v_ra /(h_off + hext + hs)
20   a_rp = v_rp / (h_off + hext)
21
22   s = (vt - a_ra * ry_dl * hy_fl) *  np.cos(phis)
23   s += -1 * a_rp * (hy_fl - hoe) * np.cos(2*phis) * np.cos(phis)
24   s += a_rp * rz_dl * hy_fl * np.cos(2*phis)
25   s += a_rp * rx_fl * hy_fl * np.cos(2*phis) * np.sin(phis)
26   s += a_ra * rx_dl * hy_fl * np.sin(phis)
27   s += delta
28
29   return s
30
31 curves = []
32
33 # open data
34
35 args = sys.argv
36
37 raw_data_path = args[1]
38 root_path = args[2]
39 tt = args[3]
40
41 data = json.load(open(raw_data_path, "r"))
42
43 fields = sorted(list(data[tt].keys()), reverse=True, key=lambda x:
   ↪  float(x))
44
45 mean_hoe = 29.3 # Oe per 1e7 A/cm2
46 hoe = Constant(mean_hoe)
47
48 # fit parameters and limits
```

```
49
50  yfl0 = 10.0 # Oe Per 1e7 A/cm2
51  yrange = 1e3 # Oe Per 1e7 A/cm2
52
53  xrange = 2.0 # relative to hfl_y
54  zrange = 2.0 # relative to hfl_y
55
56  hy_fl = Parameter(name="hy_fl", value=yfl0).range(-1*yrange, yrange)
57  ry_dl = Parameter(name="ry_dl", value=1e-1).range(0.0, 2.0)
58
59  # e.g. hx_fl = rx_fl * hy_fl in units of Oe Per 1e7 A/cm2
60  rx_fl = Parameter(name="rx_fl", value=-1e-1).range(-1*xrange, xrange)
61  rx_dl = Parameter(name="rx_dl", value=1e-1).range(-1*xrange, xrange)
62  rz_dl = Parameter(name="rz_dl", value=1e-1).range(-1*zrange, zrange)
63
64  # compensate for small remnant magnetization in the bore
65  h_off = Parameter(name="h_off", value=10.0).range(-50.0, 50.0)
66
67  # set vt range
68
69  hmax = fields[0]
70  v2wy_max = np.array(data[tt][hmax]["v2wy"])
71  amp_max = (np.amax(v2wy_max) - np.amin(v2wy_max))/2.
72  mid_max = (np.amax(v2wy_max) + np.amin(v2wy_max))/2.
73
74  vt = Parameter(name="vt", value=amp_max/4.).range(amp_max*0.02, amp_max)
75
76  path1w = root_path + "/DREAMS_1w_" + str(tt) + "/first_harmonic-err.json"
77  rpdata = json.load(open(path1w, "r"))
78
79  # calculate constant factors
80
81  vps = []
82
83  for key in rpdata.keys():
84
85    if "vp" in key:
86      if "4000" not in key:
87        vps.append(rpdata[key]['mean'])
88
89  vps = np.array(vps)
90
91  hs, dhs = interpolants.GetHs([float(tt)])
```

```
92  hs = hs[0]
93
94  ra, dra = interpolants.GetRa([float(tt)])
95  ra = ra[0]
96
97  rl, drl = interpolants.GetRL([float(tt)])
98  rl = rl[0]
99
100 rfm, rnm = interpolants.GetCurrentRatios([float(tt)])
101 rfm = rfm[0]
102 rnm = rnm[0]
103
104 t_fm = 6.8e-7 # in cm
105 t_nm = 46.6e-7 # in cm
106 width = 10e-4 # in cm
107
108 i_total = 3.5 / rl # in Amps rms
109 i_fm = i_total * rfm # in Amps rms
110 i_nm = i_total * rnm # in Amps rms
111
112 a_shm = t_nm * width
113
114 rp = np.mean(vps) / i_fm
115
116 j_shm = 1e-7 * i_nm / a_shm # in units of 1e7 A/cm2
117
118 # set up fitting curves
119
120 for ii in range(0, len(fields)):
121   hh = fields[ii]
122   hext = float(hh)
123
124   v_ra = Constant(0.5 * ra * i_fm * j_shm)
125   v_rp = Constant(rp * i_fm * j_shm)
126
127   phis = np.radians(np.array(data[tt][hh]["phi"]))
128   v2wy = np.array(data[tt][hh]["v2wy"])
129
130   span = np.amax(v2wy) - np.amin(v2wy)
131   mid = (np.amax(v2wy) + np.amin(v2wy))/2.
132
133   dv2wy = 2e-7 * np.ones(v2wy.shape) * (hext / float(hmax))**0.5
134   # increased error on lower amplitude points
```

```
135
136     delta = Parameter(name="delta_" + str(int(hh)),
        ↪  value=mid).range(mid-span, mid+span)
137
138     h_ext = Constant(hext)
139
140     designator = "T{:d}_H{:d}".format(int(tt), int(hh))
141
142     curves.append(Curve(V2WFit, phis, v2wy, dy=dv2wy, name=designator,\
143       delta=delta, h_off=h_off, hext=h_ext, hs=hs, vt=vt, v_ra=v_ra,
          ↪  v_rp=v_rp, hoe=hoe,\
144         hy_fl=hy_fl, ry_dl=ry_dl, rx_fl=rx_fl, rx_dl=rx_dl, rz_dl=rz_dl,
            ↪  s2t=s2t))
145
146 problem = FitProblem(curves)
```

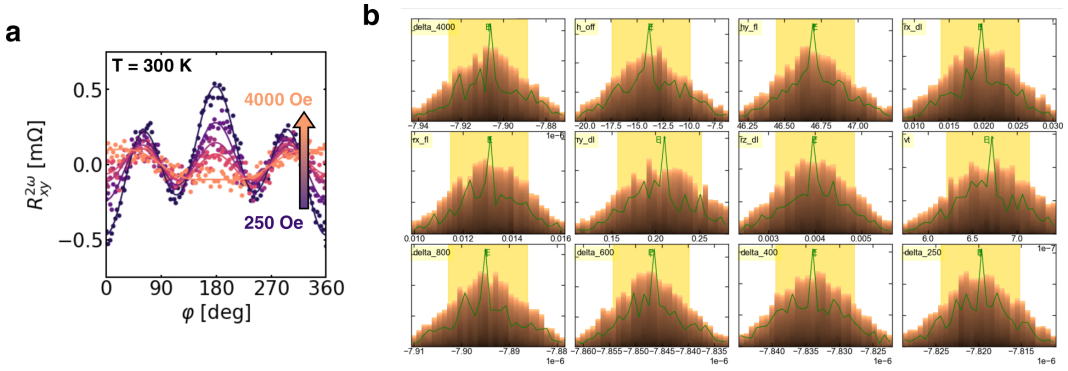

Figure E.2: **Parameter distributions from DREAM for strict parameter fit to in-plane second harmonic Hall effect data**. **a** The result of a stricter fitting method which takes the parameter field scaling confirmed by the free fitting method, and enforces the $1/H_{ext}$, $1/(H_{ext} + H_S)$ scaling for all parameters except for the offset, shown for a device at T = 300 K with mostly σ_{xz}^{y}. **b**, the corresponding parameter distribution for the fitted curves in **a**. This is a more efficient fitting routine that can be consistently applied to all devices at all temperature setpoints, including devices with anomalous offset scaling as in Figure 4.4, with the caveat that information is lost about any h_{FL}^{z} spin torque effective fields.

BIBLIOGRAPHY

[1] Železný, J., Wadley, P., Olejnik, K., Hoffmann, A. & Ohno, H. Spin transport and spin torque in antiferromagnetic devices. *Nat. Phys.* **14**, 220–228 (2018).

[2] Šmejkal, L., Mokrousov, Y., Yan, B. & MacDonald, A. H. Topological antiferromagnetic spintronics. *Nat. Phys.* **14**, 242–251 (2018).

[3] Dieny, B. *et al.* Opportunities and challenges for spintronics in the microelectronics industry. *Nat. Electron.* **3**, 446–459 (2020).

[4] Noel, P. *et al.* Non-volatile electric control of spin-charge conversion in a $SrTiO_3$ rashba system. *Nature* **580**, 483–486 (2020).

[5] Miron, I. M. *et al.* Current-driven spin torque induced by the Rashba effect in a ferromagnetic metal layer. *Nat. Mater.* **9**, 230–4 (2010).

[6] Khang, N. H. D., Ueda, Y. & Hai, P. N. A conductive topological insulator with large spin Hall effect for ultralow power spin-orbit torque switching. *Nat. Mater.* **17**, 808–813 (2018).

[7] Han, J. *et al.* Room-temperature spin-orbit torque switching induced by a topological insulator. *Phys. Rev. Lett.* **119**, 077702 (2017).

[8] Mellnik, A. R. *et al.* Spin-transfer torque generated by a topological insulator. *Nature* **511**, 449–51 (2014).

[9] Reynolds, N. *et al.* Spin Hall torques generated by rare-earth thin films. *Phys. Rev. B* **95** (2017).

[10] Liu, L. *et al.* Spin-torque switching with the giant spin hall effect of tantalum. *Science* **336**, 555–8 (2012).

[11] Liu, L., Moriyama, T., Ralph, D. C. & Buhrman, R. A. Spin-torque ferromagnetic resonance induced by the spin Hall effect. *Phys. Rev. Lett.* **106**, 036601 (2011).

[12] Sinova, J., Valenzuela, S. O., Wunderlich, J., Back, C. H. & Jungwirth, T. Spin Hall effects. *Rev. Mod. Phys.* **87**, 1213–1260 (2015).

[13] Seemann, M., Ködderitzsch, D., Wimmer, S. & Ebert, H. Symmetry-imposed shape of linear response tensors. *Phys. Rev. B* **92** (2015).

[14] Gurung, G., Shao, D.-F. & Tsymbal, E. Y. Spin-torque switching of noncollinear antiferromagnetic antiperovskites. *Phys. Rev. B* **101** (2020).

[15] Nan, T. *et al.* Controlling spin current polarization through non-collinear antiferromagnetism. *Nat. Comm.* **11**, 4671 (2020).

[16] Tetlow, H. & Gradhand, M. Semiconductor spintronics: Tuning the spin Hall effect in Si. *Phys. Rev. B* **87** (2013).

[17] Dyakonov, M. & Perel, V. I. Possibility of orienting electron spins with current. *JETP Lett.* (1971).

[18] Dyakonov, M. & Perel, V. I. Current-induced spin orientation of electrons in semiconductors. *Phys. Let. A* **35** (1971).

[19] Engel, H. A., Halperin, B. I. & Rashba, E. I. Theory of spin Hall conductivity in n-doped GaAs. *Phys. Rev. Lett.* **95**, 166605 (2005).

[20] Edelstein, V. M. Spin polarization of conduction electrons induced by electric current in two-dimensional asymmetric electron systems. *Sol. Stat. Comm.* **73**, 233–235 (1990).

[21] Miron, I. M. *et al.* Current-driven spin torque induced by the rashba effect in a ferromagnetic metal layer. *Nat. Mater.* **9**, 230–4 (2010).

[22] Noel, P. *et al.* Non-volatile electric control of spin-charge conversion in a $SrTiO_3$ Rashba system. *Nature* **580**, 483–486 (2020).

[23] Murakami, S., Nagaosa, N. & Zhang, S. C. Dissipationless quantum spin current at room temperature. *Science* **301**, 1348–51 (2003).

[24] Guo, G. Y., Murakami, S., Chen, T. W. & Nagaosa, N. Intrinsic spin hall effect in platinum: first-principles calculations. *Phys. Rev. Lett.* **100**, 096401 (2008).

[25] Meisenheimer, P. B., Novakov, S., Vu, N. M. & Heron, J. T. Perspective: Magnetoelectric switching in thin film multiferroic heterostructures. *Jour. of Appl. Phys.* **123**, 240901 (2018).

[26] Berry, M. Quantal phase factors accompanying adiabatic changes. *Proc. of the Royal Soc. of Lond. A.* **392**, 45–57 (1997).

[27] Xiao, D., Chang, M.-C. & Niu, Q. Berry phase effects on electronic properties. *Rev. Mod. Phys.* **82**, 1959–2007 (2010).

[28] Hall, E. H. XXXVIII. On the new action of magnetism on a permanent electric current. *The Lond. Edin. and Dubl. Phil. Mag. and Jour. of Sci.* **10**, 301–328 (1880).

[29] Hall, E. H. XVIII. On the "Rotational Coefficient" in nickel and cobalt. *The Lond. Edin. and Dubl. Phil. Mag. and Jour. of Sci.* **12**, 157–172 (1881).

[30] Pugh, E. M. & Rostoker, N. Hall effect in ferromagnetic materials. *Reviews of Modern Physics* **25**, 151–157 (1953).

[31] Tanaka, T. *et al.* Intrinsic spin Hall effect and orbital Hall effect in 4d and 5d transition metals. *Phys. Rev. B* **77** (2008).

[32] Chang, M.-C. & Niu, Q. Berry curvature, orbital moment, and effective quantum theory of electrons in electromagnetic fields. *Jour. of Phys. Cond. Matt.* **20**, 193202 (2008).

[33] Zhang, Y. *et al.* Strong anisotropic anomalous hall effect and spin hall effect in the chiral antiferromagnetic compounds Mn_3X (X=Ge, Sn, Ga, Ir, Rh, and Pt). *Phys. Rev. B* **95** (2017).

[34] Sakurai, J. & Napolitano, J. *Modern Quantum Mechanics, Second Edition* (Addison-Wesley, 2011).

[35] Ashcroft, N. W. & Mermin, N. D. *Solid State Physics* (Harcourt, Inc., 1976).

[36] Noky, J. & Sun, Y. Linear response in topological materials. *Appl. Sci.* **9**, 4832 (2019).

[37] Yao, Y. *et al.* First principles calculation of anomalous hall conductivity in ferromagnetic bcc Fe. *Phys. Rev. Lett.* **92**, 037204 (2004).

[38] Zhang, Y., Železný, J., Sun, Y., van den Brink, J. & Yan, B. Spin Hall effect emerging from a noncollinear magnetic lattice without spin–orbit coupling. *New Jour. of Phys.* **20**, 073028 (2018).

[39] Krén, E. *et al.* Magnetic structures and exchange interactions in the Mn-Pt system. *Phys. Rev.* **171**, 574–585 (1968).

[40] Nakatsuji, S., Kiyohara, N. & Higo, T. Large anomalous hall effect in a non-collinear antiferromagnet at room temperature. *Nature* **527**, 212–5 (2015).

[41] Kimata, M. *et al.* Magnetic and magnetic inverse spin hall effects in a non-collinear antiferromagnet. *Nature* **565**, 627–630 (2019).

[42] Takeuchi, Y. *et al.* Chiral-spin rotation of non-collinear antiferromagnet by spin-orbit torque. *Nat. Mater.* (2021).

[43] Zhang, W. *et al.* Giant facet-dependent spin-orbit torque and spin hall conductivity in the triangular antiferromagnet $IrMn_3$. *Sci. Adv.* **2**, e1600759 (2016).

[44] Kohn, A. *et al.* The antiferromagnetic structures of $IrMn_3$ and their influence on exchange-bias. *Sci. Rep.* **3**, 2412 (2013).

[45] Krén, E., Kádár, G., Pál, L., Sólyom, J. & Szabó, P. Magnetic structures and magnetic transformations in ordered Mn_3(Rh, Pt) alloys. *Phys. Lett.* **20**, 331–332 (1966).

[46] Liu, Z. Q. *et al.* Electrical switching of the topological anomalous hall effect in a non-collinear antiferromagnet above room temperature. *Nat. Electron.* **1**, 172–177 (2018).

[47] Chen, X. *et al.* Observation of the antiferromagnetic spin Hall effect. *Nat. Mater.* **20**, 800–804 (2021).

[48] Chiang, C. C., Huang, S. Y., Qu, D., Wu, P. H. & Chien, C. L. Absence of evidence of electrical switching of the antiferromagnetic Néel vector. *Phys. Rev. Lett.* **123**, 227203 (2019).

[49] Brun, K., Kjekshus, A. & Pearson, W. B. Equiatomic transition metal alloys of manganese. I. tetragonal PtMn phase. *Phil. Mag.* **10**, 291–& (1964).

[50] Menshikov, A. Z., Antropov, V. P., Gasnikova, G. P., Dorofeyev, Y. A. & Kazantsev, V. A. Magnetic phase diagram of ordered $(Fe_{1-x}Mn_x)$Pt alloys. *Jour. of Mag. and Mag. Mat.* **65**, 159–166 (1987).

[51] Villars, P. & Okamoto, H. Mn-Pt binary phase diagram 0-100 at.% Pt. URL https://materials.springer.com/isp/phase-diagram/docs/c_0902284. Copyright 2016 Springer-Verlag Berlin Heidelberg & Material Phases Data System (MPDS), Switzerland & National Institute for Materials Science (NIMS), Japan. Accessed 2021-07-31.

[52] Crc handbook of chemistry and physics, 84th edition. *Jour. of the Amer. Chem. Soc.* **126**, 1586–1586 (2004).

[53] Trassin, M. *et al.* Ultraflat monocrystalline Pt (111) electrodes. *Jour. of Appl. Phys.* **105**, 106101 (2009).

[54] Adachi, H., Hata, T., Tomoaki, M., Tomoyoshi, M. & Kikuo, T. *Handbook of Sputter Deposition Technology Second Edition* (William Andrew, 2012).

[55] Novakov, S. *et al.* Composite spin Hall conductivity from non-collinear antiferromagnetic order. *Submitted. In review.* (2021).

[56] Feng, J. *et al.* Effects of oxidation of top and bottom interfaces on the electric, magnetic, and spin-orbit torque properties of Pt/Co/AlO_x trilayers. *Phys. Rev. Appl.* **13** (2020).

[57] Avci, C. O., Beach, G. S. D. & Gambardella, P. Effects of transition metal spacers on spin-orbit torques, spin Hall magnetoresistance, and magnetic anisotropy of Pt/Co bilayers. *Phys. Rev. B* **100** (2019).

[58] Moulder, J. F., Stickle, W. F., Sobol, P. E. & Domben, K. D. *Handbook of X-ray Photoelectron Spectroscopy* (Perkin-Elmer Corporation, 1992).

[59] Vrugt, J. *et al.* Accelerating Markov chain monte carlo simulation by differential evolution with self-adaptive randomized subspace sampling. *Int. Journ. of Nonl. Sci. & Num. Sim.* **10**, 273–290 (2009).

[60] Kienzle, P., Krycka, J., Patel, N. & Sahin, I. Bumps (version 0.8.0) [Computer Software]. College Park, MD: University of Maryland. Retrieved aug 03, 2021. (2011).

[61] Krén, E., Kádár, G., Pál, L. & Szabó, P. Investigation of the first-order magnetic transformation in Mn_3Pt. *Jour. of Appl. Phys.* **38**, 1265–1266 (1967).

[62] Hayashi, M., Kim, J., Yamanouchi, M. & Ohno, H. Quantitative characterization of the spin-orbit torque using harmonic Hall voltage measurements. *Phys. Rev. B* **89** (2014).

[63] Avci, C. O. *et al.* Interplay of spin-orbit torque and thermoelectric effects in ferromagnet/normal-metal bilayers. *Phys. Rev. B* **90** (2014).

[64] Garello, K. *et al.* Symmetry and magnitude of spin-orbit torques in ferromagnetic heterostructures. *Nat. Nanotechnol.* **8**, 587–93 (2013).

[65] Landau, L. & Lifshitz, E. On the theory of the dispersion of magnetic permeability in ferromagnetic bodies. *Phys. Zeit. der Sowj.* **8**, 135 (1935).

[66] Brown, W. F. Thermal fluctuations of a single-domain particle. *Phys. Rev.* **130**, 1677–1686 (1963).

[67] Slonczewski, J. C. Current-driven excitation of magnetic multilayers. *Jour. of Mag. and Mag. Mat.* **159**, L1–L7 (1996).

[68] Ralph, D. C. & Stiles, M. D. Spin transfer torques. *Jour. of Mag. and Mag. Mat.* **320**, 1190–1216 (2008).

[69] Baumgartner, M. *et al.* Spatially and time-resolved magnetization dynamics driven by spin-orbit torques. *Nat. Nanotechnol.* (2017).

[70] Stamm, C. *et al.* Magneto-optical detection of the spin Hall effect in Pt and W thin films. *Phys. Rev. Lett.* **119** (2017).

[71] Soldatov, I. V. & Schäfer, R. Advances in quantitative kerr microscopy. *Physical Review B* **95** (2017).

[72] (John Wiley & Sons, Ltd, 2008).

[73] Fan, Y. *et al.* Magnetization switching through giant spin-orbit torque in a magnetically doped topological insulator heterostructure. *Nat. Mater.* **13**, 699–704 (2014).

[74] Xiao, D., Yao, Y., Fang, Z. & Niu, Q. Berry-phase effect in anomalous thermoelectric transport. *Phys. Rev. Lett.* **97**, 026603 (2006).

[75] Lee, W. L., Watauchi, S., Miller, V. L., Cava, R. J. & Ong, N. P. Anomalous hall heat current and nernst effect in the $CuCr_2Se_{4-x}Br_x$ ferromagnet. *Phys. Rev. Lett.* **93**, 226601 (2004).

[76] Nguyen, M. H., Ralph, D. C. & Buhrman, R. A. Spin torque study of the spin Hall conductivity and spin diffusion length in platinum thin films with varying resistivity. *Phys. Rev. Lett.* **116**, 126601 (2016).

[77] Wang, W. *et al.* Anomalous spin-orbit torques in magnetic single-layer films. *Nat. Nanotechnol.* **14**, 819–824 (2019).

[78] Nahrwold, G. *et al.* Structural, magnetic, and transport properties of Permalloy for spintronic experiments. *Jour. of Appl. Phys.* **108**, 013907 (2010).

[79] Zhang, W., Han, W., Jiang, X., Yang, S.-H. & S. P. Parkin, S. Role of transparency of platinum–ferromagnet interfaces in determining the intrinsic magnitude of the spin hall effect. *Nat. Phys.* **11**, 496–502 (2015).

[80] Fitzsimmons, M. R. *et al.* Antiferromagnetic domain size and exchange bias. *Phys. Rev. B* **77** (2008).

[81] Kim, M. G. *et al.* Imaging antiferromagnetic antiphase domain boundaries using magnetic Bragg diffraction phase contrast. *Nat. Comm.* **9**, 5013 (2018).

[82] Sapozhnik, A. A. *et al.* Direct imaging of antiferromagnetic domains in Mn_2Au manipulated by high magnetic fields. *Phys. Rev. B* **97** (2018).

[83] Hoffmann, A. Spin hall effects in metals. *IEEE Trans. on Magn.* **49**, 5172–5193 (2013).

[84] Zhu, L., Ralph, D. C. & Buhrman, R. A. Highly efficient spin-current generation by the spin Hall effect in $Au_{1-x}Pt_x$. *Phys. Rev. Appl.* **10** (2018).

[85] Ou, Y., Shi, S., Ralph, D. C. & Buhrman, R. A. Strong spin Hall effect in the antiferromagnet PtMn. *Phys. Rev. B* **93** (2016).

[86] Heron, J. T., Schlom, D. G. & Ramesh, R. Electric field control of magnetism using $BiFeO_3$-based heterostructures. *Appl. Phys. Rev.* **1**, 021303 (2014).

[87] Ederer, C. & Spaldin, N. A. Weak ferromagnetism and magnetoelectric coupling in bismuth ferrite. *Phys. Rev. B* **71** (2005).

[88] Wang, J. *et al.* Epitaxial $BiFeO_3$ multiferroic thin film heterostructures. *Science* **299**, 1719–22 (2003).

[89] Trassin, M. *et al.* Interfacial coupling in multiferroic/ferromagnet heterostructures. *Phys. Rev. B* **87** (2013).

[90] Drera, G. *et al.* Grain size and stoichiometry control over RF-sputtered multiferroic $BiFeO_3$ thin films on silicon substrates. *Thin Sol. Film.* **589**, 551–555 (2015).

[91] Meisenheimer, P. B. *et al.* Engineering new limits to magnetostriction through metastability in iron-gallium alloys. *Nat. Comm.* **12**, 2757 (2021).

[92] Borrego, J. M., Blazquez, J. S., Conde, C. F., Conde, A. & Roth, S. Structural ordering and magnetic properties of arc-melted FeGa alloys. *Intermetallics* **15**, 193–200 (2007).

[93] Avci, C. O. *et al.* Current-induced switching in a magnetic insulator. *Nat. Mater.* (2016).

[94] Vlietstra, N. *et al.* Simultaneous detection of the spin-hall magnetoresistance and the spin-Seebeck effect in platinum and tantalum on yttrium iron garnet. *Phys. Rev. B* **90** (2014).

[95] Liu, L. *et al.* Symmetry-dependent field-free switching of perpendicular magnetization. *Nat. Nanotechnol.* (2021).

[96] Liu, L., Lee, O. J., Gudmundsen, T. J., Ralph, D. C. & Buhrman, R. A. Current-induced switching of perpendicularly magnetized magnetic layers using spin torque from the spin Hall effect. *Phys. Rev. Lett* **109**, 096602 (2012).

[97] Yun, S. J., Lee, K. J. & Lim, S. H. Critical switching current density induced by spin Hall effect in magnetic structures with first and second-order perpendicular magnetic anisotropy. *Sci. Rep.* **7**, 15314 (2017).

[98] Peng, S., Zhang, Y., Wang, M., Zhang, Y. & Zhao, W. *Magnetic Tunnel Junctions for Spintronics: Principles and Applications*, 1–16 (Amer. Canc. Soc., 2014).

[99] Nagaosa, N. & Tokura, Y. Topological properties and dynamics of magnetic skyrmions. *Nat. Nanotechnol.* **8**, 899–911 (2013).

[100] Nagaosa, N. Emergent inductor by spiral magnets. *Jap. Jour. of Appl. Phys.* **58**, 120909 (2019).

[101] Yokouchi, T. *et al.* Emergent electromagnetic induction in a helical-spin magnet. *Nature* **586**, 232–236 (2020).